Transactions in Theoretical and Mathematical Physics

Publisher: Qom University of Technology

ISSN: 3041-8984

Volume**:** 3, Issue 4, 2026

Available online: https://ttmp.qut.ac.ir

Table of Contents

Conformal invariance of symplectic packing numbers and relationship with symplectic capacities
Un-Gyong Jong, Kwang-Hyon Jong, Song-Il Kang
Pages 156-160

Bound State of an Electron on a ^{4}He Superfluid Droplet as a Test for Quantum Gravity
Mansour Haghighat, Farhang Loran
Pages 161-163

Tunable Casimir Torque in a Heterogeneous Rotational Microsystem Using Phase-Change Materials
Zahra Rabiee, Fatemeh Tajik
Pages 164-171

Some properties of coherent states with singular complex matrix argument
Dusan POPOV
Pages 172-190

Symmetry Reductions of Boundary Layer Equations of Second Grade Fluids
Mehmet Pakdemirli
Pages 191-201

Analytical, Numerical, and PINN Analysis of the ABC Fractional GK Equation: A Compatibility-Aware Benchmark Study
Md. Akher Chowdhury, Md. Masudar Rahman, Md. Zahangir Alam, Md. Ashik Iqbal
Pages 202-218

TTMP vol 3 (4), 2026
doi: 10.30511/TTMP.2026.2094308.1083

Transactions in Theoretical and Mathematical Physics

Conformal Invariance of Symplectic Packing Numbers and Relationship with Symplectic Capacities

Un-Gyong Jong[a1], **Kwang-Hyon Jong**[1], **Song-Il Kang**[1]

[1]Faculty of Mathematics, Kim Hyong Jik University of Education, Pyongyang, Democratic People's Republic of Korea

Received: 13 July 2026 / Accepted: 14 October 2026 / Published: 24 October 2026

Abstract

In this paper, we proved the conformal invariance of symplectic packing numbers and its consequences. We also found the relationship with symplectic capacities and studied the existence of a symplectic embedding from a symplectic ellipsoid into a polydisc.

Keywords: Symplectic packing number; Symplectic capacity; Symplectic ellipsoid; Symplectic embedding

1 Introduction

Symplectic geometry has its own characteristics because of its symplectic structure, a nondegenerate closed 2-form, and is an important rule among geometries such as algebraic and complex geometry, etc., as well as nonlinear functional analysis and dynamics [1, 2].

Symplectic embedding, a map between symplectic manifolds which preserves symplectic structure, satisfies the most fundamental nonsqueezing theorem first established by Gromov (1985).

This theorem shows that $B^{2n}(a)$ embeds symplectically into $Z^{2n}(b)$ only if $a \leq b$ where $B^{2n}(a)$ and $Z^{2n}(b)$ are respectively the symplectic ball and the symplectic cylinder defined as follows:

$$B^{2n}(a) = \Big\{x = (x^1, \cdots, x^n, y^1, \cdots, y^n) \in \mathbb{R}^{2n} \Big| \sum_{i=1}^{n} \left[(x^i)^2 + (y^i)^2\right] < \frac{a}{\pi}\Big\}, \tag{1}$$

$$Z^{2n}(b) = \Big\{x = (x^1, \cdots, x^n, y^1, \cdots, y^n) \in \mathbb{R}^{2n} \Big| (x^1)^2 + (y^1)^2 < \frac{b}{\pi}\Big\}. \tag{2}$$

[a]Corresponding author: sb.myong@star-co.net.kp

Since a and b are the areas of the cross-section by the symplectic plane span$\{e_1, f_1\}$, where $\{e_1, \ldots, e_n, f_1, \ldots, f_n\}$ is the symplectic basis of $(\mathbb{R}^{2n}, \omega_0)$, this theorem reminds us that 2-dimensional measurement of a symplectic manifold contains information for preserving the symplectic structure. Therefore, the concept of symplectic capacity emerged.

Let γ be a family of all $2n$-dimensional symplectic manifolds (M, ω). An symplectic capacity is a map $c : \gamma \to [0, +\infty)$ associating with each manifold a number in such a way that the following axioms are satisfied [2].

(1) **Monotonicity:** $c(M, \omega) \leq c(N, \tau)$, if (M, ω) symplectically embeds into (N, τ).

(2) **Conformality:** $c(M, \alpha\omega) = |\alpha| c(M, \omega)$ for all $\alpha \in \mathbb{R} \setminus \{0\}$.

(3) **Nontriviality:** $c(B^{2n}(1)) = c(Z^{2n}(1)) = 1$.

More generally, nontriviality is replaced by

(3)' **Generalized nontriviality:** For $B^{2n}(1) := B, Z^{2n}(1) := Z, 0 < c(B), c(Z) < \infty$.

In particular, a map that satisfies the first two axioms, monotonicity and conformality, is called a generalised symplectic capacity. Symplectic ellipsoid $E(r_1, \cdots, r_n)$ and polydisc $C^{2n}(a)$ mentioned mainly in this paper is as follows:

$$E(r_1, \cdots, r_n) := \Big\{(x'_1, \cdots, x'_n, y'_1, \cdots, y'_n) \in \mathbb{R}^{2n} \Big| \sum_{i=1}^{n} \frac{\pi(x_i'^2 + y_i'^2)}{r_i} < 1\Big\}, \tag{3}$$

$$C^{2n}(a) := B^2(a) \times \cdots \times B^2(a). \tag{4}$$

Radii $r_i, i = \overline{1,n}$ of ellipsoid are nonzero real numbers such that $r_1 \leq r_2 \leq \cdots \leq r_n$. By definition, $E(a, \cdots, a) = B^{2n}(a)$.

For 4-dimensional symplectic ellipsoid $E(r_1, r_2)$ the Ekeland-Hofer capacities forms a nondecreasing sequence of $kr_1, k \geq 1$ and $lr_2, l \geq 1$ with repetition [3]. Similarly, but

not the same, ECH capacities of symplectic ellipsoids are a nondecreasing sequence of $ma+nb, m,n \geq 0$.

Surprisingly, in [4] they found the necessary and sufficient condition for the existence of a symplectic embedding between symplectic ellipsoids by using ECH capacities. Detailed material comes from [5, 6]. In [7–9], they studied the existence of symplectic embeddings between specific manifolds, and this problem remains as important as ever.

Definition 1 [10] Assume that (M,ω) is connected $2n$-dimensional symplectic manifold of finite volume $Vol(M,\omega)$
$= \frac{1}{n!}\int_M \omega^n$. For each $k \in \mathbb{N}$, the k-th symplectic packing number p_k is defined as follows:

$$p_k(M,\omega) = \sup_a \frac{kVol(B^{2n}(a),\omega_0)}{Vol(M,\omega)}, \tag{5}$$

where the supremum is taken over all those a for which the disjoint union $\bigsqcup_{i=1}^{k} B^{2n}(a)$ of k equal balls symplectically embeds into (M,ω).

This packing number is a symplectic invariant, and it has been studied [11] in 4 dimensions. In [12, 13], they considered the stability of the symplectic packing number.

2 Conformal invariance of symplectic packing numbers

Both the symplectic packing number and symplectic capacities are symplectic invariants, but they are distinct. Therefore, it is natural to view the symplectic packing number in the light of monotonicity and conformality of symplectic capacity.

If you have the definitions of both the symplectic packing number and the symplectic capacity, it seems that comparing them is pointless. Still, in this paper, we ask how different they are to understand the properties of the symplectic packing number.

First, consider the packing number for a symplectic ellipsoid.

Example 1: In $(\mathbb{R}^{2n},\omega_0)$, where $\omega_0 = \sum_{i=1}^{n} dx_i \wedge dy_i$, the first symplectic packing number for $E(a_1,\cdots,a_n)$ is $\frac{a_1^{n-1}}{a_2\cdots a_n}$.

Indeed, from the definition of the symplectic ellipsoid

$$B^{2n}(a_1) \subset E(a_1,\cdots,a_n) \subset Z^{2n}(a_1), \tag{6}$$

and the biggest symplectic ball embedded into the symplectic ellipsoid $E(a_1,\cdots,a_n)$ is $B^{2n}(a_1)$. So,

$$\begin{aligned} p_1\big(E(a_1,\ldots,a_n)\big) &= \frac{\mathrm{Vol}\left(B^{2n}(a_1),\omega_0\right)}{\mathrm{Vol}\left(E(a_1,\ldots,a_n)\right)} \\ &= \frac{a_1^{n-1}}{a_2a_3\cdots a_n}. \end{aligned} \tag{7}$$

From this example, we have got something more about the symplectic packing number: Firstly, $p_1(B^{2n}(a)) = 1$ for each real number a.

Second, the symplectic packing number is not monotonic. Indeed, it is obvious that $B^{2n}(a_1)$ embeds symplectically into $E(a_1,\cdots,a_n)$. But, $p_1\big(E(a_1,\cdots,a_n)\big)$ is less than one except the special $a_1 = a_2 = \cdots = a_n$, that is,

$$p_1\big(B^{2n}(a_1)\big) \geq p_1\big(E(a_1,\cdots,a_n)\big),$$

as desired. And then, how about conformality?

Theorem 1 *For each nonzero real number α and natural number k,*

$$p_k(M,\alpha\omega) = p_k(M,\omega). \tag{8}$$

Proof Suppose that $\bigsqcup_{i=1}^{k}\big(B^{2n}(a),\omega_0\big)$ embeds symplectically into $(M,\alpha\omega)$, this means that there exist symplectic embeddings $\phi_i, i = \overline{1,n}$ such that

$$\phi_i\big(B^{2n}(a)\big) \subset (M,\alpha\omega), \tag{9}$$

and

$$\phi_i\big(B^{2n}(a)\big) \cap \phi_j\big(B^{2n}(a)\big) = \varnothing, \tag{10}$$

for all $i \neq j$. First, we check that $\big(B^{2n}(a),\omega_0\big) \xrightarrow{s} (M,\alpha\omega) \Longleftrightarrow \big(B^{2n}(\frac{a}{|\alpha|}),\omega_0\big) \xrightarrow{s} (M,\omega)$.

Let $\phi : \big(B^{2n}(a),\omega_0\big) \longrightarrow (M,\alpha\omega)$ be symplectic embedding. Then, $\phi^*(\alpha\omega) = \omega_0$ so that $\phi^*(\omega) = \frac{1}{\alpha}\omega_0$. Simplifying $a' = \frac{a}{|\alpha|}$, consider $\psi : B^{2n}(a') \to B^{2n}(a)$ defined by $\psi(x) = \sqrt{|\alpha|}x$. Then, we can see

$$\psi^*(\frac{1}{\alpha}\omega_0) = \frac{|\alpha|}{\alpha}\omega_0. \tag{11}$$

Thus, if $\alpha > 0$, we denote $\hat{\phi}$ as $\hat{\phi} = \phi\circ\psi : \big(B^{2n}(a'),\omega_0\big) \longrightarrow (M,\omega)$, if not, as $\hat{\phi} = \phi\circ\psi\circ\psi_0 : \big(B^{2n}(a'),\omega_0\big) \longrightarrow (M,\omega)$, where ψ_0 is defined as

$$\psi_0 : \big(B^{2n}(a'),\omega_0\big) \longrightarrow \big(B^{2n}(a'),-\omega_0\big), \tag{12}$$

so that $\psi_0(u,v) = (-u,v)$, for all $(u,v) \in \mathbb{R}^{2n}$.

Then, $\hat{\phi}$ is symplectic embedding which maps $\big(B^{2n}(\frac{a}{|\alpha|}),\omega_0\big)$ into (M,ω) for each real number α and we conclude

$$\begin{aligned} p_k(M,\alpha\omega) &= \sup_a\left\{\frac{k\,\mathrm{Vol}\left(B^{2n}(a),\omega_0\right)}{\mathrm{Vol}(M,\alpha\omega)}\right\} \\ &= \sup_a\left\{\frac{k\frac{1}{n!}\int_{B^{2n}(a)}\omega_0^n}{\frac{1}{n!}\int_M(\alpha\omega)^n}\right\} \\ &= \sup_a\left\{\frac{ka^n}{|\alpha|^n\mathrm{Vol}(M,\omega)}\right\} \\ &= \sup_{a'}\left\{\frac{k|\alpha|^n(a')^n}{|\alpha|^n\mathrm{Vol}(M,\omega)}\right\} = p_k(M,\omega). \end{aligned} \tag{13}$$

for all natural number k as claimed.

This theorem shows that the symplectic packing number of a symplectic manifold (M,ω) remains unchanged even though a scalar multiple dilates the symplectic structure. This differs from the conformality of symplectic capacity, which says the symplectic capacity of $(M,\alpha\omega)$ is $|\alpha|$-multiple of the capacity of (M,ω), and that's why we call this property conformal invariance of the symplectic packing number.

Finally, nontriviality is meaningful only for the symplectic ball and meaningless for the symplectic cylinder, since the symplectic packing number is defined for symplectic manifolds of finite volume. Symplectic packing number for symplectic ball is studied in [3, 14].

3 Relationship between symplectic packing numbers and symplectic capacities

Consider maps defined as

$$c_k(M,\omega) := \sup\left\{a\Big|\bigsqcup_{i=1}^{k} B^{2n}(a) \xrightarrow{s} (M,\omega)\right\}, \tag{14}$$

$$c^c(M,\omega) := \inf\left\{a\Big|(M,\omega) \xrightarrow{s} C^{2n}(a)\right\}, \tag{15}$$

for each $2n$-dimensional symplectic manifold (M,ω). Obviously, if $k=1$, c_k is Gromov width and

$$p_k(M,\omega)Vol(M,\omega) = \frac{k}{n!}\big(c_k(M,\omega)\big)^n. \tag{16}$$

The maps c_k and c^c satisfy monotonicity and conformality, so they are generalised symplectic capacities. For 4-dimensional symplectic ellipsoid $E(1,a)$, these have the following properties.

Theorem 2 *For all natural number k and $C := C^4(1)$,*

$$\Big[c^c(E(1,k))\Big]^{-1} = c_k(C), \tag{17}$$

$$\Big[c^c(E(1,k))\Big]^{2} = \frac{k}{2p_k(C)}, \tag{18}$$

Proof The first statement follows from:

By the results

$$\bigsqcup_{i=1}^{k} B^4(1) \to C^4(A) \Leftrightarrow E(1,k) \to C^4(A), \tag{19}$$

of [4, 7], we know

$$\begin{aligned} c^c(E(1,k)) &= \inf\left\{A\Big|E(1,k) \xrightarrow{s} C^{2n}(A)\right\} \\ &= \inf\left\{A\Big|\bigsqcup_{i=1}^{k} B^4(1) \to C^4(A)\right\}, \end{aligned} \tag{20}$$

and remembering $c_U(V) = \big(c^V(U)\big)^{-1}$ for

$$c_U(V) = \sup_{\lambda}\left\{\lambda\,\middle|\,\lambda U \xrightarrow{s} V\right\}, \tag{21}$$

$$c^V(U) = \inf_{\lambda}\left\{\lambda\,\middle|\,U \xrightarrow{s} \lambda V\right\}, \quad U,V \in \mathbb{R}^{2n}, \tag{22}$$

we conclude that

$$\begin{aligned} \Big[c^c(E(1,k))\Big]^{-1} &= c_{E(1,k)}(C^4(1)) \\ &= \sup\left\{a\Big|\sqrt{a}E(1,k) \to C^4(1)\right\} \\ &= \sup\left\{a\Big|E(a,ka) \to C^4(1)\right\} \\ &= \sup\left\{a\Big|\bigsqcup_{i=1}^{k} B^{2n}(a) \to C^4(1)\right\} \\ &= c_k\big(C^4(1)\big). \end{aligned} \tag{23}$$

Let's move on to the second statement of Theorem 2. By using (16) and $Vol\big(C^4(1)\big) = 1$, we get

$$\Big[c^c(E(1,k))\Big]^{2} = \frac{k}{2p_k(C)}, \tag{24}$$

from the first.

Remark 1 The map c_k in Theorem 2 is different from c_k in [15] (page 145). This theorem relates the k-th symplectic packing number p_k to the generalised symplectic capacities c_k and c^c.

Corollary 1 *The value of $c^c(E(1,k))$ is given by Table 1.*

Proof In [15], the k-th symplectic packing numbers p_k for the 4-dimensional box $(0,1)^4$ are given. Since $C^4(1)$ is equivalent symplectically to $(0,1)^4$, we get $p_k\big(C^4(1)\big)$ (Table 2).

Now, by Theorem 2, this corollary is proved.

If the second radius of the symplectic ellipsoid $E(1,a)$ is given in general, that is, $a \geq 1$ is real number, abbreviating $c^c\big(E(1,a)\big)$ by $c^c(a)$, we know

$$c^c(k) \leq c^c(a) \leq c^c(k+1), \tag{25}$$

where k is the greatest integer less than or equal to a. Indeed, it is easy from the relation

$$E(1,k) \subset E(1,a) \subset E(1,k+1), \tag{26}$$

and monotonicity of c^c. Besides, there are many generalized symplectic capacities such as ECH capacities. We suggest that readers review the relationship between the packing number and ECH capacities in detail [15].

Table 1 The values of $c^c(E(1,k))$

k	1	2	3	4	5	6	7	more that 8
c^c	1	1	$\frac{3}{2}$	$\frac{3}{2}$	$\frac{5}{3}$	$\frac{7}{4}$	$\frac{15}{8}$	$\sqrt{\frac{k}{2}}$

Table 2 The values of $p_k\big(C^4(1)\big)$

k	1	2	3	4	5	6	7	more that 8
p_k	$\frac{1}{2}$	1	$\frac{2}{3}$	$\frac{8}{9}$	$\frac{9}{10}$	$\frac{48}{49}$	$\frac{224}{225}$	1

Corollary 2 *Generalized symplectic capacity c^c for $E(1,a)$ is given in some subintervals as follows:*

$$c^c(a) = 1 \quad if \quad a \in [1,2], \tag{27}$$

$$c^c(a) = \frac{a}{2} \quad if \quad a \in [2,3], \tag{28}$$

$$c^c(a) = \frac{3}{2} \quad if \quad a \in [3,4]. \tag{29}$$

Proof The first and third cases follow from Corollary 1 and equation (25). The second case implies that the two ratios of the first and the second radius for both $E(1,a)$ and $E(A,2A)$, respectively, are always in $[2,3)$. That is, $E(1,a)$ and $E(A,2A)$ have the same shape type [16]. Therefore,

$$E(a) \xrightarrow{s} E(a') \Leftrightarrow a_i \leq a'_i, \tag{30}$$

for each i (see, Theorem 3, page 266 of [16]). We can get

$$E(1,a) \xrightarrow{s} E(A,2A) \Leftrightarrow \begin{cases} 1 \leq A \\ a \leq 2A \end{cases} \tag{31}$$

and from this,

$$\frac{a}{2} \leq A \leq 1. \tag{32}$$

Therefore $c^c(a) = \frac{a}{2}$ as desired.

The generalised symplectic capacity c^c in this paper provides an upper bound on symplectic capacities and can be used to estimate the existence of symplectic embeddings. Since symplectic ellipsoid $E(1,a)$ embeds into $C^4(b)$ if and only if $c^c(a) < b$, it is impossible to estimate the existence of symplectic embeddings using symplectic invariants other than c^c.

Example 2. Let's estimate whether $E(1,4)$ embeds into $C^4(\frac{10}{7})$ or not. First of all, the volume constraint holds:

$$\begin{aligned} \text{Vol}\big(E(1,4)\big) &= \frac{1\cdot 4}{2!} = 2, \\ \text{Vol}\big(C^4(\tfrac{10}{7})\big) &= \left(\frac{10}{7}\right)^2 = \frac{100}{49}. \end{aligned} \tag{33}$$

and the Gromov width is preserved

$$\omega_G\big(E(1,4)\big) = 1, \qquad \omega_G\big(C^4(\frac{10}{7})\big) = \frac{10}{7}. \tag{34}$$

Next, the first three terms of the Ekeland-Hofer capacity are also satisfied. Indeed, the first three terms of the Ekeland-Hofer capacity of $E(1,4)$ are $1,2,3$, respectively. But corresponding of $C^4(1)$ are given as follows [17]

$$\begin{aligned} Vol\big(E(1,4)\big) &= \frac{1\cdot 4}{2!} = 2, \\ Vol\big(C^4(\frac{10}{7})\big) &= \left(\frac{10}{7}\right)^2 = \frac{100}{49}. \end{aligned} \tag{35}$$

So, the first three terms of Ekeland-Hofer capacity of $C^4(\frac{10}{7})$ are

$$\begin{aligned} c_1\big(C^4(\tfrac{10}{7})\big) &= \frac{40}{7}, \\ c_2\big(C^4(\tfrac{10}{7})\big) &= \frac{30\sqrt{3}}{7}, \\ c_3\big(C^4(\tfrac{10}{7})\big) &= \frac{80}{7}. \end{aligned} \tag{36}$$

So, the Ekeland-Hofer capacity does not distinguish whether $E(1,4)$ embeds symplectically into $C^4(\frac{10}{7})$. But, $E(1,4)$ could not embed symplectically into $C^4(\frac{10}{7})$. From Corollary 2, we know that

$$c^c\big(E(1,4)\big) = \frac{3}{2} \geq c^c\big(C^4(\frac{10}{7})\big) = \frac{10}{7}, \tag{37}$$

this implies that $E(1,4)$ could not embed symplectically into $C^4(\frac{10}{7})$.

4 Conclusions

In this paper, we studied the conformal invariance of the symplectic packing number and its relationship to symplectic capacities, and we found a counterexample to symplectic embedding from a symplectic ellipsoid into a polydisc.

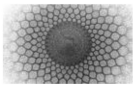
Acknowledgements Thank you to the publishing house that helped publish this manuscript.

References

1. M. Gosson *et al.*, Symplectic capacities and the geometry of uncertainty: The irruption of symplectic topology in classical and quantum, *Phys. Rep.* **484**, 131 (2009), doi: 10.1016/j.physrep.2009.08.001.
2. D. McDuff, *Introduction to symplectic topology*, (Oxford University Press, 1998).
3. D. McDuff, Hofer conjecture on embedding symplectic ellipsoids, *J. Diff. Geom.* **88**, 519 (2011), doi: 10.4310/jdg/1321366358.
4. D. McDuff *et al.*, The embedding capacity of 4-dimensional symplectic ellipsoids, *Ann. Math.* **175**, 1191 (2012), doi: 10.4007/annals.2012.175.3.5.
5. M. Hutchings, An elementary alternative to ECH capacities, *PNAS* **119**(35), e2203090119 (2022), doi: 10.1073/pnas.2203090119.
6. B. Wormleighton, ECH capacities, EHRHART theory, and toric varieties, *J. Symplectic Geom.* **19**, 475 (2021), doi: 10.4310/JSG.2021.v19.n2.a5.
7. D. Frenkel *et al.*, Symplectic embeddings of 4-dimensional ellipsoids into cubes, *J. Symplectic Geom.* **13**, 765 (2015), doi: 10.4310/JSG.2015.v13.n4.a2.
8. L. Guth, Symplectic embeddings of polydisks, *Invent. Math.* **172**, 477 (2008), doi: 10.1007/s00222-007-0103-9.
9. D. Cristofaro-Gardiner, Symplectic embeddings from concave toric domains into convex ones, *J. Diff. Geom.* **112**, 199 (2019), arXiv:1409.4378 [math.SG], doi: 10.4310/jdg/1559786421.
10. F. Schlenk, *Embedding problems in symplectic geometry*, (Walter de Gruyter, Berlin, New York, 2005), doi: 10.1515/9783110199697.
11. P. Biran, Symplectic packing in dimension 4, *Geom. Funct. Anal.* **7**, 420 (1997), doi: 10.1007/s000390050014.
12. D. Cristofaro-Gardiner, R. Hind, Boundaries of open symplectic manifolds and the failure of packing stability, arXiv:2307.01140 [math. SG], doi: 10.4171/JEMS/1707.
13. O. Buse *et al.*, Packing stability for symplectic 4-manifolds, *Trans. Amer. Math. Soc.* **368**, 8209 (2016), doi: 10.1090/tran/6802.
14. L. Traynor, Symplectic packing constructions, *J. Diff. Geom.* **41**, 735 (1995).
15. F. Schlenk, Symplectic Embedding Problems, Old and New, *Bull. Amer. Math. Soc. (N.S.)* **55**, 139 (2018), doi: 10.1090/bull/1587.
16. J. Basto Gonçalves, Symplectic rigidity and flexibility of ellipsoids, *Indag. Math.* **24**, 264 (2013), doi: 10.1016/j.indag.2012.09.011.
17. L. Baracco *et al.*, On the Ekeland-Hofer symplectic capacities of the real bidisc, *Pacific J. Math.* **305**, 423 (2020), doi: 10.2140/pjm.2020.305.423.

TTMP vol 3 (4), 2026
doi: 10.30511/TTMP.2026.2096069.1088

Transactions in Theoretical and Mathematical Physics



Bound State of an Electron on a ^{4}He Superfluid Droplet as a Test for Quantum Gravity

Mansour Haghighat[1,2], **Farhang Loran**[3,a]

[1]Physics Department, College of Sciences, Shiraz University, Shiraz 71454, Iran
[2]Islamic World Science and Technology Monitoring and Citation Institute (ISC), Shiraz, Iran
[3]Department of Physics, Isfahan University of Technology, Isfahan 84156-83111, Iran

Received: 29 July 2026 / Accepted: 26 October 2026 / Published: 28 October 2026

Abstract We address the problem of finding a system in which there would be measurable quantum gravitational effects. Following standard quantum-field methods, we have calculated the first-order radiative correction of graviton exchange on the binding energy of an electron with an ultra cold superfluid droplet of ^{4}He with mass about the Planck mass. For two ^{4}He droplets with a mass difference of about one microgram, we show that the relative difference in the binding energies is about one percent.

Keywords: Bound State; ^{4}He Superfluid Droplet; Test for Quantum Gravity

1 Introduction

The most important obstacle in the search for quantum gravity (QG) is the absence of the experimental input that is needed to test the theory. There are papers on the phenomenology of quantum gravity [1] but the magnitude of the proposed QG effects are expected to be negligible in standard. circumstances because the Planck scale suppresses them. However, small effects can become observable in special contexts. and one can always search for an experimental setup such that a very large number of the very small quantum-gravity contributions are effectively summed together. For instance, the ratio of the forces of gravity and electricity between two particles with mass m and charge e is

$$\frac{F_g}{F_e} = \frac{Gm^2}{e^2} = \frac{hc}{2\pi e^2}\left(\frac{m}{M_{\text{Planck}}}\right)^2, \tag{1}$$

that is too small for the fundamental particles with the ordinary masses. It is well known that electrons can be bound in surface states. outside certain bulk dielectrics such as ^{4}He [2]. Experimentally, the binding energy of the electron to the surface of liquid helium has been measured using millimeter-wave spectroscopy to be 8 Kelvin [3]. R. Y. Chiao by replacing the oil of the classic "Millikan oil drops" with superfluid helium (^{4}He) with a gravitational mass of around the Planck-mass scale ($M_{\text{Plank}} \approx 22$ micrograms), proposed an experimental setup for a gravity-wave antenna [4]. In this Letter we propose another experiment to detect the interplay between gravity and QED by exploring the bound state of an electron to an ultra cold superfluid drop of ^{4}He (e-^{4}He bound state).

2 Gravitational Quantum Corrections to the Binding Energy

The e-^{4}He bound state is due to formation of an image charge inside the dielectric sphere of the drop. The image potential is of the form [5]

$$V = -Ze^2/r, \tag{2}$$

[a]Corresponding author: loran@iut.ac.ir

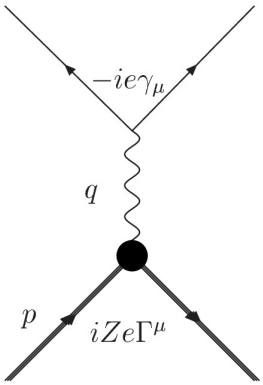


Fig. 1 One photon exchange diagram for e-^{4}He bound state. The upper legs show the electronic current, while the lower legs stand for the ^{4}He drop current.

where r is the radial distance of the electron from the droplet surface and

$$Z = \frac{(k-1)}{(k+1)}, \tag{3}$$

in which $k \approx 1.057$ is the relative permittivity of Helium. Because there is a barrier of 1 eV, the penetration of the electron with binding energy of a few Kelvin, into the Helium drop is negligible. Thus, one can assume the e-^{4}He bound state as an ideal Hydrogen-like system. Using Eq.(3), one can see that the binding energy is about 8 Kelvin ($\approx 10^{-3}$ eV) and the effective Bohr radius $r_{\rm B} = 76$ [6]. This justifies the tick-film approximation we have considered to obtain Eq.(3) as far as the radius of the Helium drop is about one millimeter.

In QED, the tree-level diagram corresponding to the hydrogen-like bound state is give by Fig.(1).

In this letter, we would like to explore the QG effects in the e-^{4}He bound state. As is seen from Eq.(1), classically, only for particles with mass comparable to the Planck mass the gravitational force is comparable with the electrical force. Therefore, at tree level, the one graviton exchange diagram between the electron and ^{4}He is negligible in comparison with the corresponding one-photon exchange diagram. In contrast, one anticipates that for the one loop corrections, the QG-correction for the photon-^{4}He vertex to be the only significant term in comparison with the other one loops coming from both QED and QG, see Fig.(2). Thus,

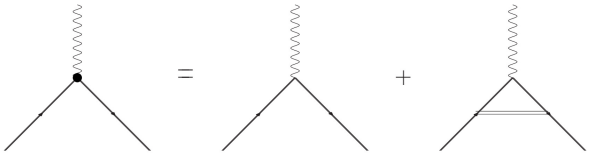


Fig. 2 The most significant gravitational one-loop correction for the ^{4}He-photon vertex. The double line represents the graviton.

gravitational quantum corrections can have a valuable contribution to the binding energy of e-^{4}He bound state. Consequently, this mesoscopic system seems to be a good lab for probing the nature of the interplay between gravitation and quantum mechanics.

The straightforward framework for general relativity quantized for small fluctuations is a nonrenormalizable quantum field theory. In fact, it is shown that the one-loop divergences in the theory of scalar field coupled to quantum general relativity, can only be cancelled by counterterms that do not appear in the original action [7]. Nevertheless, this framework is appropriate for describing interactions at energies and momenta below the Planck scale $M_{\rm Planck}$ when treated as an effective low-energy theory [8, 9].

To calculate the one-loop diagram in Fig.(2) we consider the action for transverse-traceless small fluctuation modes $h_{\mu\nu}$, given by the following Lagrangian,

$$\begin{aligned}\mathscr{L} = &\frac{M^2_{\rm Planck}}{128\pi}\eta^{\alpha\beta}\partial_\alpha h^{\mu\nu}\partial_\beta h_{\mu\nu} \\ &+(\eta^{\mu\nu}+h^{\mu\nu})\,\partial_\mu\phi^*\partial_\nu\phi+\cdots,\end{aligned} \tag{4}$$

in which $\eta_{\alpha\beta}$ is the Minkowski metric. In this way, for the low momentum transfer, one can show that

$$\begin{aligned}\Gamma^\mu = p^\mu + \frac{1}{\pi}\frac{m^2_{^4\rm He}}{M^2_{\rm Planck}}\Bigg\{&-\frac{11}{6}+\frac{1}{2}\ln\left(\frac{\Lambda}{m_{^4\rm He}}\right) \\ &-\ln\left(\frac{\lambda}{2m_{^4\rm He}}\right)+\mathscr{O}\left(\frac{q^2}{m^2_{^4\rm He}}\right)\Bigg\}p^\mu,\end{aligned} \tag{5}$$

Where $\Lambda \sim M_{\rm Planck}$ is the ultraviolet cutoff and λ is an infrared cutoff. It should be noted that the mass of the helium droplet is not a fundamental parameter of the quantum gravity and therefore the first three terms due to the one loop correction in Eq.(5) can not be absorbed into any properly

renormalized vertex function. In fact, the QG-structural effects can be described by a form factor which, in principle, can be measured in the e-^{4}He scattering processes for different ^{4}He droplets. The form factor at vanishing four momentum transfer for an appropriate *reference mass* m_r can be set to unity. Therefore the vertex function can be written as follows.

$$\Gamma^\mu = p^\mu + \frac{1}{\pi}\frac{m^2_{^4\mathrm{He}}}{M^2_{\mathrm{Planck}}}\left\{\ln\left(\frac{m_{^4\mathrm{He}}}{m_r}\right) + \mathscr{O}\left(\frac{q^2}{m^2_{^4\mathrm{He}}}\right)\right\} p^\mu, \quad (6)$$

3 Conclusion

From Eq.(6) one verifies that the binding energy depends on the mass of ^{4}He droplet. Therefore, the physical observable can be the difference in the binding energies of different *e*-^{4}He droplets with different masses,

$$\frac{\Delta E}{E} \simeq \frac{1}{\pi M^2_{\mathrm{Planck}}}\Delta\left(m^2_{^4\mathrm{He}}\ln\frac{m_{^4\mathrm{He}}}{m_r}\right). \quad (7)$$

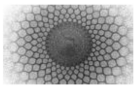
where E is the binding energy of *e*-^{4}He system at the tree level and ΔE is the energy difference due to the one loop QG-correction for two ^{4}He droplets with different masses. For instance, for two ^{4}He droplets with mass difference of about one microgram, and $m_r \simeq M_{\mathrm{Planck}}$ the relative difference in the binding energies will be about two percent.

References

1. J. Ellis, J. Lopez, N. Mavromatos, D. Nanopoulos and CPLEAR Collaboration, Phys. Lett. B 364 (1995) 239. https://doi.org/10.1016/0370-2693(95)01416-0;
   R. Brustein, M. Gasperini, M. Giovannini and G. Veneziano, Phys. Lett. B 361 (1995) 45. https://doi.org/10.1016/0370-2693(95)01128-D;
   I. C. Percival and W. T. Strunz, Proc. R. Soc. A 453 (1997) 431, arXiv:quant-ph/9607011. https://doi.org/10.1098/rspa.1997.0025;
   G. Amelino-Camelia, J. Ellis, N. E. Mavromatos, D. V. Nanopoulos and S. Sarkar, Nature 393 (1998) 763. https://doi.org/10.1038/31647;
   D. V. Ahluwalia, Mod. Phys. Lett. A 13 (1998) 1393. https://doi.org/10.1142/S0217732398001455;
   G. Amelino-Camelia, Nature 398 (1999) 216, arXiv:gr-qc/9808029. https://doi.org/10.1038/18377;
   G. F. Giudice, R. Rattazzi and J. D. Wells, Nucl. Phys. B 544 (1999) 3. https://doi.org/10.1016/S0550-3213(99)00044-9;
   E. A. Mirabelli, M. Perelstein and M. E. Peskin, Phys. Rev. Lett. 82 (1999) 2236. https://doi.org/10.1103/PhysRevLett.82.2236.
2. M. W. Cole and M. H. Cohen, Phys. Rev. Lett. 23 (1969) 1238. https://doi.org/10.1103/PhysRevLett.23.1238;
   M. W. Cole, Phys. Rev. B 2 (1970) 4239. https://doi.org/10.1103/PhysRevB.2.4239;
   V. B. Shikin, Zh. Eksp. Teor. Fiz. 58 (1970) 1748 [Sov. Phys. JETP 31 (1970) 936];
   V. B. Shikin and Yu. P. Monarkha, J. Low Temp. Phys. 16 (1974) 193. https://doi.org/10.1007/BF00655867.
3. C. C. Grimes and G. Adams, Phys. Rev. Lett. 36 (1976) 145. https://doi.org/10.1103/PhysRevLett.36.145.
4. R. Y. Chiao, Int. J. Mod. Phys. D 16 (2007) 2309, arXiv:gr-qc/0606118. https://doi.org/10.1142/S0218271807011279.
5. E. Y. Andrei (ed.), *Two-Dimensional Electron Systems: on Helium and other Cryogenic Substrates*, Kluwer Academic Publishers, Dordrecht, 1997. https://doi.org/10.1007/978-94-015-1286-2;
   P. M. Platzman and M. I. Dykman, Science 284 (1999) 1967. https://doi.org/10.1126/science.284.5422.1967.
6. C. C. Grimes *et al.*, Phys. Rev. B 13 (1976) 140. https://doi.org/10.1103/PhysRevB.13.140.
7. G. 't Hooft and M. Veltman, Ann. Inst. H. Poincaré Phys. Théor. A 20 (1974) 69. https://www.numdam.org/item/AIHPA_1974__20_1_69_0/.
8. J. F. Donoghue, Phys. Rev. D 50 (1994) 3874, arXiv:gr-qc/9405057. https://doi.org/10.1103/PhysRevD.50.3874.
9. S. P. Robinson and F. Wilczek, Phys. Rev. Lett. 96 (2006) 231601. https://doi.org/10.1103/PhysRevLett.96.231601.

TTMP vol 3 (4), 2026
doi: 10.30511/TTMP.2026.2107007.1098

Transactions in Theoretical and Mathematical Physics



Tunable Casimir Torque in a Heterogeneous Rotational Microsystem Using Phase-Change Materials

Zahra Rabiee[1,a], **Fatemeh Tajik**[1]

[1]Department of Condensed Matter Physics, Faculty of Physics, Alzahra University, Tehran, Iran

Received: 25 September 2026 / Accepted: 28 October 2026 / Published: 05 November 2026

Abstract This study investigates the Casimir torque in a rotational microelectromechanical system (MEMS) with heterogeneous surface coatings using Lifshitz theory in conjunction with the proximity force approximation (PFA). The system consists of two parallel plates: a stationary, highly electrically conductive gold plate and a movable plate that rotates about its central axis. The movable plate is divided into two regions with different surface coatings: the left half in the schematic is coated with silicon carbide (SiC), whereas the right half is coated with a phase-change material (PCM), considered in both its crystalline and amorphous phases. We assume an equilibrium separation of 300 nm between the plates in the parallel configuration and consider small rotational angles. The results show that switching the PCM coating from the amorphous to the crystalline phase increases the net Casimir torque by approximately a factor of 12 at a normalized rotation angle of $\phi = 0.9$. Thermal fluctuations at 450 K further enhance the torque; however, in the crystalline phase, the temperature dependence becomes less pronounced because quantum fluctuations dominate. The equivalent Casimir voltage required to counteract the Casimir torque with an electrostatic torque in the realistic material configuration is substantially lower than that for an ideal, perfectly conducting system. These results demonstrate that the proposed heterogeneous rotational system may provide a viable platform for active optomechanical switching and tunable thermal sensing in NEMS applications.

Keywords: Optical properties; Silicon carbide; Casimir torque; Phase change material; Micro electromechanical system; Lifshitz theory; Casimir force.

1 Introduction

The Casimir force, predicted by Hendrik Casimir in 1948, originates from quantum fluctuations of the electromagnetic field in vacuum [1]. At submicron separations, this interaction increases rapidly and can induce irreversible stiction between components, thereby compromising the functionality and reliability of micro- and nanoelectromechanical systems (MEMS/NEMS) [2, 7]. Consequently, developing effective strategies to control and tune Casimir interactions is of considerable practical importance.

One promising approach uses phase-change materials (PCMs), which can reversibly switch between ordered crystalline and disordered amorphous phases in response to thermal or electrical stimuli. Depending on the material, this phase transition can substantially change the optical response, particularly the frequency-dependent dielectric function [3, 4]. Previous studies have demonstrated that these changes can modulate the Casimir force and affect the actuation dynamics of microsystems [3, 4]. More broadly, recent reviews discuss the influence of material optical re-

[a]Corresponding author: rabiee2213@gmail.com

sponse, geometry, temperature, conductivity, and surface morphology on Casimir interactions and their applications in MEMS [8, 9].

In this work, we investigate a two-segment rotational microsystem in which the movable plate comprises two regions coated with different materials: silicon carbide (SiC) and a phase-change material (PCM). The primary objective is to calculate the net Casimir torque arising from the system's optical heterogeneity and to investigate how phase transitions and finite temperature affect the torque magnitude and the corresponding electrostatic-equivalent voltage. Our approach combines mechanical rotation, material heterogeneity, phase switching, and thermal effects within the framework of Lifshitz theory and the proximity force approximation (PFA). Recent theoretical work has also highlighted the relevance of thermal effects to Casimir torque between birefringent plates [11]. Here, we examine thermal effects in a heterogeneous rotational geometry, with particular emphasis on the influence of the PCM phase on the net torque and its temperature dependence. A closely related study investigated phase transitions and thermal fluctuations in nonhomogeneous torsional Casimir MEMS containing SiC and a PCM [12]. The present treatment focuses on the equilibrium torque and electrostatic-equivalent voltage.

2 System Geometry and Calculation Method

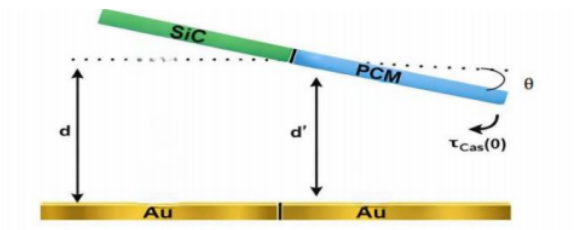


Fig. 1 Schematic of the rotational system consisting of a stationary gold plate and a movable plate with SiC coating on the left half and PCM coating on the right half. Positive rotation lowers the PCM side toward the stationary plate.

The system consists of a stationary bottom plate made of gold (Au) and a movable top plate with a total length $L_x = 2\times10^{-5}\,\mathrm{m}$ and a width $L_y = 10^{-5}\,\mathrm{m}$. As shown in Fig. 1, the left half of the movable plate is coated with silicon carbide (SiC), whereas the right half is coated with a phase-change material (PCM), considered in both its crystalline and amorphous phases. The PCM investigated here is silver–indium–antimony–telluride (Ag–In–Sb–Te, AIST).

The initial separation between the two plates in the parallel configuration is $d = 300\,\mathrm{nm}$. The movable plate can rotate through a small angle θ about its central axis. For a positive rotation that brings the PCM-coated side closer to the gold plate, the local separations at a distance r from the rotation axis are

$$d'_L = d + r\sin\theta, \qquad d'_R = d - r\sin\theta. \tag{1}$$

Both the material heterogeneity and the rotational displacement can contribute to a net Casimir torque about the rotation axis.

According to Lifshitz theory, the magnitude of the attractive Casimir pressure between two parallel, nonmagnetic plates separated by a vacuum gap h at temperature T is [5]

$$p(h,T) = \frac{k_\mathrm{B}T}{\pi}{\sum_{n=0}^{\infty}}' \int_0^\infty k_\parallel \,\mathrm{d}k_\parallel\, q_n \times \sum_{\nu=\mathrm{TE,TM}} \frac{r_{1\nu}r_{2\nu}e^{-2q_nh}}{1-r_{1\nu}r_{2\nu}e^{-2q_nh}}. \tag{2}$$

Here, the prime indicates that the $n=0$ term has half weight. The Matsubara frequencies and perpendicular wave-vector components are defined by

$$\xi_n = \frac{2\pi k_\mathrm{B}T}{\hbar}n, \tag{3}$$

$$q_n = \sqrt{k_\parallel^2 + \frac{\xi_n^2}{c^2}}, \tag{4}$$

$$\kappa_{i,n} = \sqrt{k_\parallel^2 + \varepsilon_i(i\xi_n)\frac{\xi_n^2}{c^2}}. \tag{5}$$

The vacuum relative permittivity is unity. The Fresnel reflection coefficients at the vacuum–material interfaces are

$$r_{i,\mathrm{TE}} = \frac{q_n - \kappa_{i,n}}{q_n + \kappa_{i,n}}, \tag{6}$$

$$r_{i,\mathrm{TM}} = \frac{\varepsilon_i(i\xi_n)q_n - \kappa_{i,n}}{\varepsilon_i(i\xi_n)q_n + \kappa_{i,n}}. \tag{7}$$

All reflection coefficients in Eq. (2) are evaluated at $i\xi_n$ and $k_\parallel$.

The dielectric functions at imaginary frequencies are obtained from the measured optical response through

$$\varepsilon_j(i\xi) = 1 + \frac{2}{\pi}\int_0^\infty \frac{\omega\,\mathrm{Im}\,\varepsilon_j(\omega)}{\omega^2+\xi^2}\,\mathrm{d}\omega. \tag{8}$$

Experimental optical data are supplemented, where appropriate, by a Drude extrapolation at low frequencies [4, 7]. The Drude dielectric function on the imaginary frequency axis is

$$\varepsilon_{\mathrm{D}}(i\xi) = 1 + \frac{\omega_{\mathrm{p}}^2}{\xi(\xi+\gamma)}, \tag{9}$$

where ω_{p} is the plasma frequency and γ is the relaxation rate. At zero temperature, the Matsubara sum is replaced by a continuous frequency integral:

$$k_{\mathrm{B}}T\sum_{n=0}^{\infty}{}' \longrightarrow \frac{\hbar}{2\pi}\int_0^\infty \mathrm{d}\xi. \tag{10}$$

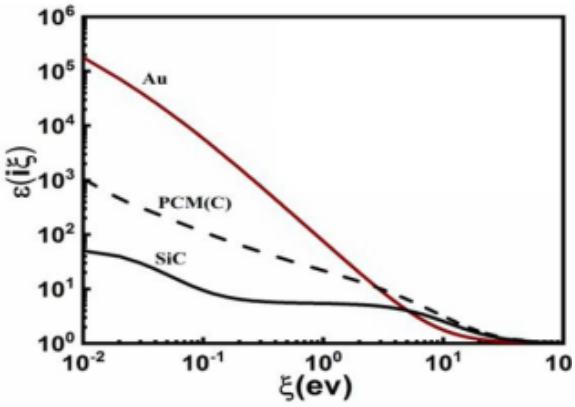


Fig. 2 Dielectric functions $\varepsilon(i\xi)$ as a function of imaginary frequency for Au, SiC, and crystalline PCM, denoted by PCM(C), used in the rotational MEMS.

For small rotational angles and gaps much smaller than the lateral plate dimensions, we employ the proximity force approximation (PFA) [6]. Let $a = L_x/2$, and choose a signed coordinate x along the movable plate such that the PCM occupies $0 < x < a$ and SiC occupies $-a < x < 0$. Positive rotation reduces the gap on the PCM side. Within the linearized small-angle geometry, the local separation is

$$h(x,\theta) = d - x\theta. \tag{11}$$

We denote by $p_j(h,T) > 0$ the magnitude of the attractive Lifshitz pressure between gold and material j at separation h and temperature T. Taking positive torque to increase θ, the local proximity approximation gives

$$\tau_{\mathrm{Cas}}(\theta,T) = L_y\int_0^a x\Big[p_{\mathrm{PCM}}(d-x\theta,T) - p_{\mathrm{SiC}}(d+x\theta,T)\Big]\,\mathrm{d}x. \tag{12}$$

This expression follows by integrating the local attractive force with its signed moment arm about the central axis.

Equivalently, let $\mathscr{F}_j(h,T)$ denote the interaction free energy per unit area, normalized to vanish at infinite separation. With the positive attractive-pressure convention,

$$p_j(h,T) = \frac{\partial\mathscr{F}_j(h,T)}{\partial h}. \tag{13}$$

The interaction free energy in the same approximation is

$$U_{\mathrm{Cas}}(\theta,T) = L_y\int_0^a\Big[\mathscr{F}_{\mathrm{PCM}}(d-x\theta,T) + \mathscr{F}_{\mathrm{SiC}}(d+x\theta,T)\Big]\,\mathrm{d}x. \tag{14}$$

The relation

$$\tau_{\mathrm{Cas}} = -\frac{\partial U_{\mathrm{Cas}}}{\partial\theta} \tag{15}$$

then reproduces Eq. (12).

For smooth pressure functions and $a|\theta|/d \ll 1$, Taylor expansion yields

$$\tau_{\mathrm{Cas}}(\theta,T) = \tau_0(T) + K_{\mathrm{Cas}}(T)\theta + \mathscr{O}(\theta^2), \tag{16}$$

where

$$\tau_0(T) = \frac{L_y a^2}{2}\left[p_{\mathrm{PCM}}(d,T) - p_{\mathrm{SiC}}(d,T)\right], \tag{17}$$

and

$$K_{\mathrm{Cas}}(T) = -\frac{L_y a^3}{3}\left[\frac{\partial p_{\mathrm{PCM}}(d,T)}{\partial d} + \frac{\partial p_{\mathrm{SiC}}(d,T)}{\partial d}\right]. \tag{18}$$

The constant term measures the torque caused by material heterogeneity in the parallel configuration, whereas the linear coefficient measures the angular response. For identical coatings, $\tau_0 = 0$, and the torque is an odd function of θ. For heterogeneous coatings, a nonzero torque may already be present at $\theta = 0$.

Within the linearized geometry, we define

$$\theta_0 = \frac{d}{a}, \qquad \phi = \frac{\theta}{\theta_0}. \tag{19}$$

For $|\phi| < 1$, the smallest and largest local gaps are

$$h_{\min} = d(1 - |\phi|), \tag{20}$$

$$h_{\max} = d(1 + |\phi|). \tag{21}$$

Using $d = 300\,\text{nm}$ and $a = 10\,\mu\text{m}$, we obtain $\theta_0 = 0.03\,\text{rad}$. Thus, $\phi = 0.9$ corresponds to $\theta = 0.027\,\text{rad}$ and a minimum gap of 30 nm. A normalized angle close to unity therefore represents proximity to contact, even though the physical angle remains small.

The Taylor expansion in Eq. (16) requires $|\phi| \ll 1$ and should not be extrapolated to the near-contact regime. The validity of the local proximity approximation is a separate issue involving the gap, slope, finite plate dimensions, and coating boundary. Near contact, the results can also become more sensitive to surface roughness and the material description at small separations.

3 Results

3.1 Casimir Torque at Zero Temperature

Table 1 Casimir torque at zero temperature, expressed in units of $10^{-15}\,\text{N m}$.

Normalized angle ϕ	Ideal	Crystalline	Amorphous
0.01	0.87	0.81	0.53
0.30	1.14	0.98	0.61
0.50	2.74	1.95	0.84
0.80	16.9	7.2	1.3
0.90	135.5	34.8	2.9

Table 1 presents the Casimir torque for the ideal perfectly conducting case and the realistic material configuration as a function of the normalized rotation angle,

$$\phi = \frac{\theta}{\theta_0} = \frac{a\theta}{d}, \qquad a = \frac{L_x}{2}. \tag{22}$$

In the crystalline phase, the torque is closer to the ideal perfectly conducting value than in the amorphous phase, particularly at small normalized angles. The amorphous phase produces a substantially smaller torque. At $\phi = 0.9$, the crystalline-phase torque exceeds the amorphous-phase torque by a factor of approximately 12.

3.2 Effect of Temperature

Figures 3 and 4 show the torque reduction factor,

$$\eta(\phi, T) = \frac{\tau_{\text{Cas}}(\phi, T)}{\tau_{\text{Cas}}^{\text{ID}}(\phi, T)}, \tag{23}$$

where $\tau_{\text{Cas}}^{\text{ID}}$ denotes the torque for the ideal perfectly conducting reference system at the same angle and temperature. The reduction factor increases at 450 K compared with its zero-temperature value, particularly in the amorphous phase.

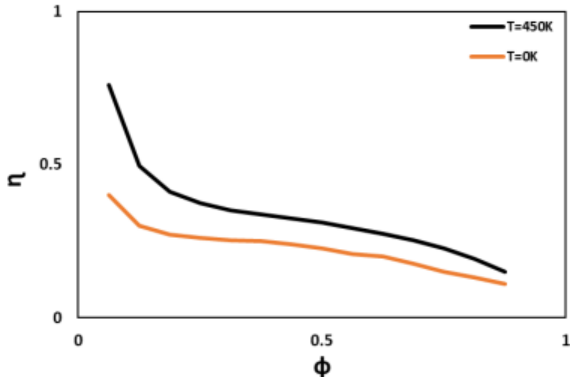


Fig. 3 Torque reduction factor $\eta = \tau_{\text{Cas}}/\tau_{\text{Cas}}^{\text{ID}}$ versus normalized angle ϕ for the microsystem containing amorphous PCM at $T = 0\,\text{K}$ and $T = 450\,\text{K}$.

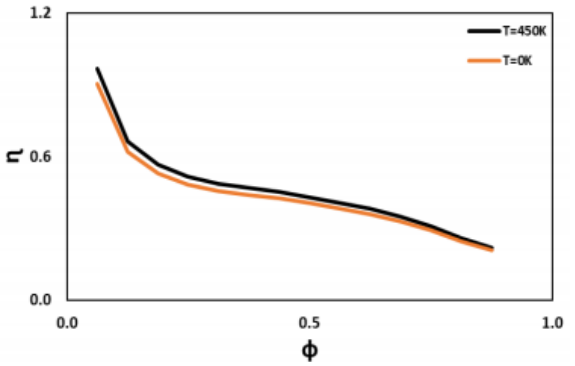


Fig. 4 Torque reduction factor $\eta = \tau_{\text{Cas}}/\tau_{\text{Cas}}^{\text{ID}}$ versus normalized angle ϕ for the microsystem containing crystalline PCM at $T = 0\,\text{K}$ and $T = 450\,\text{K}$.

The finite-temperature calculations at $T = 450\,\text{K}$ show that thermal fluctuations enhance the total Casimir torque. However, the magnitude of this enhancement strongly depends on the PCM phase. In the crystalline phase, where the

quantum contribution remains dominant, increasing the temperature produces only a modest change in the torque, with an enhancement of less than 20%. By contrast, in the amorphous phase, where the zero-temperature Casimir torque is comparatively weak, the thermal contribution can account for up to approximately 50% of the total torque.

This pronounced phase-dependent thermal response suggests two distinct operating regimes: a thermally responsive regime in the amorphous phase, potentially suitable for temperature sensing, and a comparatively thermally stable regime in the crystalline phase. Such phase-dependent tunability could benefit the development of adaptive NEMS devices intended to operate in environments with substantial temperature variations.

These observations are consistent with the broader literature showing that thermal corrections to Casimir interactions depend on geometry, separation, and material optical response [9, 10]. Recent theoretical work has also demonstrated substantial thermal effects on Casimir torque between birefringent plates [11]. A study of nonhomogeneous torsional PCM MEMS also reported reduced sensitivity of actuation to thermal fluctuations in the crystalline phase [12].

3.3 Equivalent Casimir Voltage

The compensating electrodes must produce a torque opposite to the Casimir torque. Their placement and electrical connection determine both the sign and magnitude of the electrostatic torque; coating heterogeneity alone does not specify this electrode configuration. For a specified electrode configuration, let $C(\theta)$ denote the capacitance. At a fixed applied voltage V, the electrostatic torque is

$$\tau_{\mathrm{el}}(\theta,V)=\frac{V^2}{2}\frac{\mathrm{d}C}{\mathrm{d}\theta}=G(\theta)V^2, \tag{24}$$

where

$$G(\theta)=\frac{1}{2}\frac{\mathrm{d}C}{\mathrm{d}\theta}. \tag{25}$$

The voltage producing an electrostatic torque equal in magnitude to the Casimir torque is

$$V_{\mathrm{eq}}(\theta,T)=\sqrt{\frac{|\tau_{\mathrm{Cas}}(\theta,T)|}{|G(\theta)|}}, \qquad G(\theta)\neq 0. \tag{26}$$

This magnitude comparison corresponds to actual torque compensation only when the two torques have opposite signs. In that case, the signed balance condition is

$$\tau_{\mathrm{Cas}}(\theta,T)+G(\theta)V^2=0, \tag{27}$$

which yields

$$V^2=-\frac{\tau_{\mathrm{Cas}}(\theta,T)}{G(\theta)}\geq 0. \tag{28}$$

At a fixed angle and for the same electrostatic geometry, the material and ideal-conductor calculations must therefore satisfy

$$\frac{V_{\mathrm{eq}}^{\mathrm{mat}}}{V_{\mathrm{eq}}^{\mathrm{ID}}}=\sqrt{\frac{|\tau_{\mathrm{Cas}}^{\mathrm{mat}}|}{|\tau_{\mathrm{Cas}}^{\mathrm{ID}}|}}. \tag{29}$$

This identity provides a direct consistency check between the torque and equivalent-voltage results. Torque balance alone does not establish stability. Stability additionally requires a negative derivative of the total torque with respect to angle at equilibrium, including any mechanical restoring torque:

$$\left.\frac{\partial\tau_{\mathrm{tot}}}{\partial\theta}\right|_{\theta=\theta_{\mathrm{eq}}}<0, \tag{30}$$

where the derivative is evaluated at fixed applied voltage and temperature, and

$$\tau_{\mathrm{tot}}=\tau_{\mathrm{Cas}}+\tau_{\mathrm{el}}+\tau_{\mathrm{mech}}. \tag{31}$$

For comparison, the closed-form ideal-conductor reference expression used in the original formulation is

$$V_{\mathrm{eq}}^{\mathrm{ID}}(\phi)=\left[\frac{\pi^2\hbar c}{90\varepsilon_0 d^2}\times\frac{\phi^3(3+\phi^2)}{(1-\phi^2)^3\left[\ln(1-\phi)+\frac{\phi}{1-\phi}\right]}\right]^{1/2}, \qquad 0<\phi<1. \tag{32}$$

Here, ε_0 denotes the vacuum permittivity in SI units, not the vacuum relative permittivity, which is unity. This expression is a zero-temperature ideal-conductor magnitude benchmark. Its electrostatic geometry factor is that of a single half-plate parallel-gap electrode with capacitance

$$C_{\mathrm{ref}}(\theta)=\frac{\varepsilon_0 L_y}{\theta}\ln\left(\frac{d}{d-a\theta}\right). \tag{33}$$

For positive θ, this electrode attracts the approaching half and gives a positive torque. It therefore does not, by itself, compensate a positive Casimir torque. Actual compensation requires an electrode arrangement with the opposite torque sign, using its own $G(\theta)$ in Eq. (26). The closed-form benchmark must not be applied to the realistic heterogeneous system without the appropriate material torque and electrode geometry.

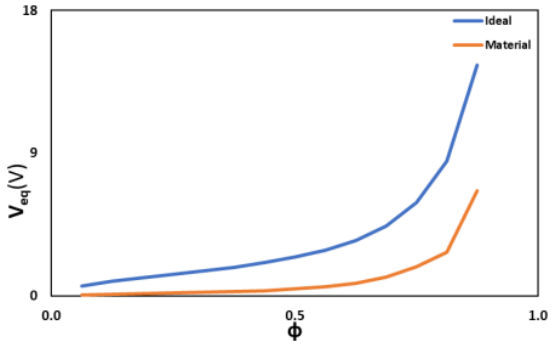


Fig. 5 Equivalent Casimir voltage V_{eq} versus normalized angle $\phi = \theta/\theta_0$ for the ideal perfectly conducting configuration and the realistic microsystem composed of crystalline PCM, SiC, and Au at $T = 0\,\mathrm{K}$.

The calculation of the equivalent Casimir voltage shows that the voltage required to counterbalance the Casimir torque through an electrostatic torque in the realistic material configuration is substantially lower than that required in the ideal perfectly conducting case. For example, for the same assumed electrostatic geometry at $\phi = 0.8$, the equivalent voltage is approximately $V_{\mathrm{eq}} = 2.74\,\mathrm{V}$ in the crystalline phase and $V_{\mathrm{eq}} = 1.16\,\mathrm{V}$ in the amorphous phase. The corresponding value for the ideal perfectly conducting configuration is $V_{\mathrm{eq}}^{\mathrm{ID}} = 4.2\,\mathrm{V}$.

The substantially reduced compensation voltage indicates that the Casimir-induced rotational behavior can be controlled using relatively low electrostatic bias voltages, potentially reducing the electrical energy required for actuation and control. In the amorphous phase, where the intrinsic Casimir torque is comparatively weak, only a small electrostatic bias is required to compensate for the interaction. Provided that the stability condition is also satisfied, this may allow operation near a zero-total-torque equilibrium. This characteristic may be advantageous for low-power memory and switching concepts in which minimal actuation energy and stable near-zero-torque states are desirable.

4 Conclusion

In this study, we investigated the net Casimir torque in a rotational microsystem with heterogeneous surface coatings of SiC and a phase-change material (PCM), using Lifshitz theory in conjunction with the proximity force approximation (PFA). The results show that switching the PCM from the amorphous to the crystalline phase substantially enhances the Casimir torque. At a normalized rotation angle of $\phi = 0.9$, the torque in the crystalline phase is approximately 12 times greater than that in the amorphous phase.

This pronounced difference primarily reflects the substantial change in the PCM's frequency-dependent dielectric response across the phase transition. In particular, the crystalline phase exhibits a stronger absorptive response, characterized by an enhanced imaginary part of the dielectric function over relevant frequency ranges, and consequently displays more metal-like optical behavior than the amorphous phase. This modification of the electromagnetic reflection properties alters the fluctuation-induced interaction within the gap, leading to a stronger Casimir interaction and, consequently, a larger torque.

This phase-dependent behavior provides a route toward an active optomechanical switch operating between low- and high-torque states. Switching may be induced by thermal or electrical stimulation of the PCM, without requiring a continuous external voltage bias to maintain its material phase.

From a fundamental physics perspective, this study shows that optical heterogeneity, combined with an asymmetric rotational geometry, can generate a substantial net Casimir torque without intrinsic material anisotropy. This provides a useful physical concept for designing tunable micro- and nanoelectromechanical devices. These results build on previous studies of Casimir-force modulation using phase-change materials [3, 4], while extending the concept to torque generation in a heterogeneous rotational system.

Related torsional PCM-MEMS work also addresses phase-dependent thermal effects [12].

A normalized angle close to unity represents proximity to contact, even though the physical angle remains small. The Taylor expansion of the torque requires $|\phi| \ll 1$ and should not be extrapolated to this regime. The validity of the local proximity approximation is a separate issue involving the gap, slope, finite plate dimensions, and coating boundary. Near contact, the results can also become more sensitive to surface roughness and the material description at small separations.

Another potentially important extension would be to incorporate surface roughness into the theoretical model. At very small separations, local variations in the gap can significantly modify the electromagnetic interaction. Including experimentally realistic roughness profiles would therefore provide a more comprehensive assessment of the robustness of the predicted Casimir torque. Finite-size and edge effects also warrant further investigation.

Combining phase-change materials, heterogeneous surface coatings, and rotational geometry provides a means to actively tune the Casimir torque. The proposed configuration allows adjustment of both the torque amplitude, through switching between weak- and strong-torque regimes, and the thermal response, through switching between relatively temperature-insensitive and temperature-responsive regimes. These characteristics highlight the potential of phase-change-enabled Casimir systems for tunable optomechanical switching, thermal sensing, and low-power NEMS applications.

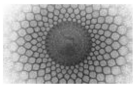
References

1. H. B. G. Casimir, "On the attraction between two perfectly conducting plates," Proceedings of the Koninklijke Nederlandse Akademie van Wetenschappen **51**, 793–795 (1948).
2. F. M. Serry, D. Walliser, and G. J. Maclay, "The role of the Casimir effect in the static deflection and stiction of membrane strips in microelectromechanical systems (MEMS)," Journal of Applied Physics **84**, 2501–2506 (1998). doi:10.1063/1.368410.
3. G. Torricelli, P. J. van Zwol, O. Shpak, C. Binns, G. Palasantzas, B. J. Kooi, V. B. Svetovoy, and M. Wuttig, "Switching Casimir forces with phase-change materials," Physical Review A **82**, 010101(R) (2010). doi:10.1103/PhysRevA.82.010101.
4. M. Sedighi, W. H. Broer, S. Van der Veeke, V. B. Svetovoy, and G. Palasantzas, "Influence of materials' optical response on actuation dynamics by Casimir forces," Journal of Physics: Condensed Matter **27**, 214014 (2015). doi:10.1088/0953-8984/27/21/214014.
5. E. M. Lifshitz, "The theory of molecular attractive forces between solids," Soviet Physics JETP **2**, 73–83 (1956).
6. B. E. Sernelius, "Different Approaches," in *Fundamentals of van der Waals and Casimir Interactions*, Springer Series on Atomic, Optical, and Plasma Physics, Vol. 102 (Springer, Cham, 2018), pp. 109–123. doi:10.1007/978-3-319-99831-2_6.
7. F. Tajik, *Casimir Torques and Lateral Forces: Influence of Optical Properties and Surface Morphology*, Ph.D. thesis, University of Groningen (2018). University repository.
8. B. Spreng, T. Gong, and J. N. Munday, "Recent developments on the Casimir torque," International Journal of Modern Physics A **37**, 2241011 (2022). doi:10.1142/S0217751X22410111.
9. B. Elsaka, X. Yang, P. Kästner, K. Dingel, B. Sick, P. Lehmann, S. Y. Buhmann, and H. Hillmer, "Casimir Effect in MEMS: Materials, Geometries, and Metrologies—A Review," Materials **17**, 3393 (2024). doi:10.3390/ma17143393.
10. M. Dhital and U. Mohideen, "A Brief Review of Some Recent Precision Casimir Force Measurements," Physics **6**, 891–904 (2024). doi:10.3390/physics6020055.
11. B. Spreng and J. N. Munday, "Thermal Effects in the Casimir Torque between Birefringent Plates," Physical Review Letters **135**, 013602 (2025). doi:10.1103/32gq-dbms.

12. F. Tajik and Z. Dadigiv, “Chaotic motion due to amorphous to crystalline phase transition in torsional Casimir MEMS under the influence of thermal fluctuations,” Physica B: Condensed Matter **718**, 417881 (2025). doi:10.1016/j.physb.2025.417881.

TTMP vol 3 (4), 2026
doi: 10.30511/TTMP.2026.2095052.1082

Transactions in Theoretical and Mathematical Physics



Some properties of coherent states with singular complex matrix argument

Dušan Popov[1,2,a]

[1] University Politehnica Timişoara, Department of Physical Foundations of Engineering, Bd. V. Pârvan No. 2, 300223 Timişoara, Romania
[2] Serbian Academy of Nonlinear Sciences (SANS), Kneza Mihaila 36, Beograd-Stari Grad, Belgrade, Serbia

Received: 19 July 2026 / Accepted: 30 October 2026 / Published: 06 Nomember 2026

Abstract In this paper, we studied the properties of a new version of coherent states whose argument is a linear combination of two special singular 2×2 matrices, each with a single nonzero element equal to 1, and two complex labelling variables as expansion coefficients. We show that this new version of coherent states satisfies all conditions imposed on coherent states, for both pure and mixed (thermal) states characterised by the density operator. As applications, we examined the connection between these coherent states and qubits and von Neumann entropy.

keywords: coherent states, singular matrix, Hamel basis, density operator, entropy.

1 Introduction

Coherent states were discovered a century ago by Schrödinger in 1926, although he did not use this name [1]. They have proven useful in various branches of theoretical physics, especially quantum optics and quantum information. Starting with the linear quantum harmonic oscillator, coherent states were later formulated for more complex quantum systems, including nonlinear oscillators. Methods for describing the properties of these states have been diverse, including phase-space considerations, operator algebra, semiclassical approximations, geometric quantisation, and more [2–6], and the references therein. Among the newest methods, one can consider bicomplex algebra, which highlights the properties of bicomplex numbers. In particular, a new generation of coherent states has been constructed using generalized hypergeometric functions with bicomplex arguments [7, 8].

[a]e-mail: dusan_popov@yahoo.co.uk

Another relatively new direction in examining the properties of coherent states involves states with matrix-valued arguments. In this approach, the parameter labelling the coherent states is replaced by a matrix-valued function [9, 10].

Coherent states with a shifted argument, as well as displaced number states, have also begun to attract attention [11–13].

On the other hand, consider the vector space of square diagonal matrices. A basis for this space can be described as a Hamel basis [14]. Every matrix in this space can be uniquely written as a finite linear combination of the standard diagonal basis matrices. These are singular elementary matrices with one diagonal element equal to 1 and all remaining elements equal to zero:

$$\begin{pmatrix} a & b \\ c & d \end{pmatrix} = a \begin{pmatrix} 1 & 0 \\ 0 & 0 \end{pmatrix} + b \begin{pmatrix} 0 & 1 \\ 0 & 0 \end{pmatrix} + c \begin{pmatrix} 0 & 0 \\ 1 & 0 \end{pmatrix} + d \begin{pmatrix} 0 & 0 \\ 0 & 1 \end{pmatrix}. \quad (1)$$

The matrix elements are real or complex numbers.

By definition, a matrix is singular if its determinant is zero. Consequently, such a matrix is non-invertible. For diagonal square matrices, a matrix is singular if at least one diagonal element is zero.

In this paper, we examine a particular case of a singular diagonal matrix: one with a single nonzero element on the main diagonal, equal to 1, and zeros elsewhere.

We examine coherent states labelled by a linear combination of two singular diagonal 2×2 matrices, with two complex variables as expansion coefficients.

We therefore consider the following two basic singular matrices:

$$u_0 \equiv \begin{pmatrix} 1 & 0 \\ 0 & 0 \end{pmatrix}, \qquad u_1 \equiv \begin{pmatrix} 0 & 0 \\ 0 & 1 \end{pmatrix}. \quad (2)$$

A diagonal square matrix, viewed as an element of this vector space, can be written as a linear combination of these basis matrices with complex coefficients:

$$Z \equiv \begin{pmatrix} z & 0 \\ 0 & \sigma \end{pmatrix} = zu_0 + \sigma u_1 = z \begin{pmatrix} 1 & 0 \\ 0 & 0 \end{pmatrix} + \sigma \begin{pmatrix} 0 & 0 \\ 0 & 1 \end{pmatrix}. \tag{3}$$

For the two-dimensional case examined here, we use the argument specified in Eq. (3). This leads to functions satisfying Cauchy's functional equation [15], but involving complex variables:

$$\begin{aligned} \mathcal{F}(zu_0 + \sigma u_1) &= \mathcal{F}(zu_0) + \mathcal{F}(\sigma u_1) \\ &= \mathcal{F}(z)u_0 + \mathcal{F}(\sigma)u_1. \end{aligned} \tag{4}$$

In this paper, we study the properties of coherent states from two perspectives: as coherent states with a shifted complex argument, and as coherent states whose argument is a linear combination of special singular 2×2 matrices forming a Hamel basis. This is the main purpose of the present paper. Owing to the properties of these matrices, functions labelled by two complex variables decompose into two functions, each depending on only one variable. Our 2×2 matrices are somewhat similar to a matrix representation of quaternions, which extend complex numbers through one real component and three imaginary components. However, the matrices used here have specific properties.

Complex representations of quaternions have also been used to construct vector coherent states [9–11, 16, 17].

2 Some properties of special square orthogonal matrices

As is known, any quantum state of a system is represented by a linear combination of state vectors, the set of these vectors forming an orthonormal basis in Hilbert space (the vectors being mutually perpendicular and of norm equal to one). One of the most useful bases is the Fock vector basis, which uses occupation-number states. Each individual state is a single-particle state, an eigenstate of the particle number operator, orthogonal, and part of a complete set for representing any arbitrary quantum state in Fock space. In matrix form, each Fock vector is represented as a column vector with all terms zero except one, which is 1 and represents the state containing a single particle.

Thus, the column vector $|n\rangle$, of dimensions $n_{\max}\times1$, and its transpose (row vector) $\langle n| = |n\rangle^T$, with dimensions $1 \times n_{\max}$, have all elements equal to zero, except for the element in position $n+1$, which is equal to 1:

$$\begin{aligned} &\mathcal{M}(|n\rangle)_{n_{\max}\times1} \equiv (\delta_{in})_{n_{\max}\times1}, \quad \delta_{in} = \begin{cases} 0, & i \neq n, \\ 1, & i = n, \end{cases} \\ &\mathcal{M}(\langle n|)_{1\times n_{\max}} \equiv (\delta_{jn})_{1\times n_{\max}}, \quad \delta_{jn} = \begin{cases} 0, & j \neq n, \\ 1, & j = n. \end{cases} \end{aligned} \tag{5}$$

Their product satisfies

$$\mathcal{M}(\langle n|)_{1\times n_{\max}} \mathcal{M}(|n\rangle)_{n_{\max}\times1} = 1. \tag{6}$$

In expanded form, the Fock vectors are expressed as follows:

$$|0\rangle \equiv \begin{pmatrix} 1 \\ 0 \\ \vdots \\ 0 \end{pmatrix}, \quad |1\rangle \equiv \begin{pmatrix} 0 \\ 1 \\ \vdots \\ 0 \end{pmatrix}, \quad \ldots, \quad |n_{\max}\rangle \equiv \begin{pmatrix} 0 \\ 0 \\ \vdots \\ 1 \end{pmatrix}. \tag{7}$$

Consequently, the Fock-vector projector $|n\rangle\langle n|$ is a square singular diagonal matrix of dimensions $n_{\max} \times n_{\max}$, which has only one element equal to 1 on the main diagonal, the remaining off-diagonal elements being equal to zero. We denote this projector by u_n:

$$\begin{aligned} u_n \equiv |n\rangle\langle n| &= \mathcal{M}(|n\rangle)_{n_{\max}\times1} \mathcal{M}(\langle n|)_{1\times n_{\max}} \\ &\equiv (\delta^n_{ij})_{n_{\max}\times n_{\max}}, \quad \delta^n_{ij} = \begin{cases} 0, & i \neq n \text{ or } j \neq n, \\ 1, & i = j = n. \end{cases} \end{aligned} \tag{8}$$

It is observed that the matrices u_j, $j = 0, 1, \ldots, n_{\max}$, have a special structure: they have a single element on the main diagonal equal to 1, with all other elements equal to zero. These matrices are positive semidefinite, idempotent, and mutually orthogonal. Their determinant is zero; therefore, they are singular and noninvertible. Because they are diagonal, they are symmetric. The product of any two different matrices is the zero matrix. Their trace is equal to 1.

$$\begin{aligned} u_i(u_j)^m = (u_i)^m u_j = \begin{cases} u_j, & i = j, \\ 0, & i \neq j, \end{cases} \\ i, j = 0, 1, \ldots, n_{\max}, \qquad m = 1, 2, \ldots \end{aligned} \tag{9}$$

$$\sum_{n=0}^{n_{\max}-1} u_n = \sum_{n=0}^{n_{\max}-1} |n\rangle\langle n| = I_{n_{\max}}. \tag{10}$$

The 2×2 matrices of the form shown above are 2×2 projectors u_i acting on a two-dimensional Hilbert space $\mathcal{H}_2$. In most cases, this space corresponds to two-level energy systems or, in computational physics, qubits. On the other hand, the Fock vectors $|n\rangle$ belong to the infinite-dimensional Hilbert space known in quantum mechanics as Fock space $\mathcal{H}_F$. The total space is formed

by the elements obtained as the tensor product of the two spaces: $\mathcal{H}_{\text{total}} = \mathcal{H}_2 \otimes \mathcal{H}_F$. An example is $u_i \otimes |n\rangle$.

As an example often used in quantum mechanics, consider a system with $n_{\max}$ states. If the system is in thermodynamic equilibrium with the environment at temperature $T = 1/(\beta k_{\text{B}})$, its states are mixed and described by the normalised canonical density operator. This operator can be represented as a linear combination of diagonal square matrices, each having only one nonzero element on the main diagonal, equal to 1:

$$\begin{aligned}\rho &= \frac{1}{Z(\beta)} \sum_{n=0}^{n_{\max}-1} e^{-\beta E_n} |n\rangle\langle n| \\ &= \frac{1}{Z(\beta)} \sum_{n=0}^{n_{\max}-1} e^{-\beta E_n} u_n, \\ Z(\beta) &= \sum_{n=0}^{n_{\max}-1} e^{-\beta E_n}.\end{aligned} \tag{11}$$

Hence the interest in this type of matrix and, at the same time, the motivation to examine their properties in connection with applications in quantum mechanics, especially in the coherent-state approach. We limit ourselves, for reasons of clarity and brevity, to 2×2 matrices, although the results can be generalised relatively easily to matrices of dimensions $n_{\max} \times n_{\max}$.

In particular, consider a two-level energy system, where E_0 is the energy eigenvalue in the ground state $n = 0$, and E_1 is the energy eigenvalue in the excited state $n = 1$. The corresponding density operator in $\mathcal{H}_2$ has the spectral decomposition

$$\begin{aligned}\rho &= \frac{1}{Z(\beta)} \sum_{n=0}^{1} e^{-\beta E_n} |n\rangle\langle n| \\ &= \frac{e^{-\beta E_0}}{Z(\beta)} |0\rangle\langle 0| + \frac{e^{-\beta E_1}}{Z(\beta)} |1\rangle\langle 1|.\end{aligned} \tag{12}$$

The partition function, given by the sum of the diagonal elements of $e^{-\beta H}$, is

$$Z(\beta) = \operatorname{Tr}\left(e^{-\beta H}\right) = e^{-\beta E_0} + e^{-\beta E_1}. \tag{13}$$

In matrix form, the two energy states are

$$\begin{aligned}|0\rangle &\equiv \begin{pmatrix}1\\0\end{pmatrix}, \qquad \langle 0| \equiv \begin{pmatrix}1 & 0\end{pmatrix}, \\ |0\rangle\langle 0| &= \begin{pmatrix}1\\0\end{pmatrix}\begin{pmatrix}1 & 0\end{pmatrix} = \begin{pmatrix}1 & 0\\0 & 0\end{pmatrix} \equiv u_0.\end{aligned} \tag{14}$$

$$\begin{aligned}|1\rangle &\equiv \begin{pmatrix}0\\1\end{pmatrix}, \qquad \langle 1| \equiv \begin{pmatrix}0 & 1\end{pmatrix}, \\ |1\rangle\langle 1| &= \begin{pmatrix}0\\1\end{pmatrix}\begin{pmatrix}0 & 1\end{pmatrix} = \begin{pmatrix}0 & 0\\0 & 1\end{pmatrix} \equiv u_1.\end{aligned} \tag{15}$$

In quantum mechanics, when an observable has a spectrum of discrete eigenvalues and the set $\{|n\rangle\}$ is complete, any ket $|\Psi\rangle$ can be uniquely expanded as a linear combination, with the sum extending over the entire range of values of n, namely $|\Psi\rangle = \sum_n c_n |n\rangle$. The same situation occurs for singular diagonal square matrices, which can be written as a linear combination of matrices with all elements zero except one:

$$\begin{aligned}\mathcal{M}(z_n)_{n_{\max}\times n_{\max}} &\equiv (z_n \delta_{ij})_{n_{\max}\times n_{\max}}, \\ \delta_{ij} &= \begin{cases}0, & i,j \neq n, \\ z_n, & i = j = n,\end{cases} \\ & \quad n = 0, 1, \ldots, n_{\max}.\end{aligned} \tag{16}$$

$$\mathcal{M}(z_n)_{n_{\max}\times n_{\max}} = \sum_{n=0}^{n_{\max}-1} z_n u_n. \tag{17}$$

This is the linear expansion in the Hamel basis [14], that is, a maximal linearly independent set spanning a vector space through finite combinations. Here, the basis consists of linearly independent diagonal square matrices spanning the entire space of matrices of this type. The expansion is unique, and the coefficients are complex numbers, namely the elements of the singular diagonal matrix.

Let us recall the properties of these matrices:

$$\begin{aligned}&(u_0)^2 = u_0, \qquad (u_1)^2 = u_1, \\ &u_i u_j = \begin{cases}1, & i = j, \\ 0, & i \neq j,\end{cases} \qquad i,j = 0,1, \\ &u_0 + u_1 = \begin{pmatrix}1 & 0\\0 & 1\end{pmatrix} \equiv I.\end{aligned} \tag{18}$$

As a geometrical interpretation, the matrices u_j are orthogonal projection matrices that project vectors onto the real coordinate axes, with $u_0 = P_x$ and $u_1 = P_y$:

$$P_x \begin{pmatrix}x\\y\end{pmatrix} = \begin{pmatrix}x\\0\end{pmatrix}, \qquad P_y \begin{pmatrix}x\\y\end{pmatrix} = \begin{pmatrix}0\\y\end{pmatrix}. \tag{19}$$

These projection matrices represent the probability density that a system with only two states, or two energy levels, will end up in one of these states.

Finally, any 2×2 diagonal matrix can be written as a linear combination of these two projection matrices:

$$\begin{aligned}\begin{pmatrix}z & 0\\0 & \sigma\end{pmatrix} &= z\begin{pmatrix}1 & 0\\0 & 0\end{pmatrix} + \sigma\begin{pmatrix}0 & 0\\0 & 1\end{pmatrix} \\ &= z u_0 + \sigma u_1.\end{aligned} \tag{20}$$

This can be related to Cauchy's functional equation:

$$\mathcal{F}(z u_0 + \sigma u_1) = \mathcal{F}(z u_0) + \mathcal{F}(\sigma u_1). \tag{21}$$

In particular, an important property of these 2×2 diagonal matrices can be formulated for the following two situations.

If $\mathcal{F}(0) = 0$, we have

$$\mathcal{F}(xu_j) = \mathcal{F}(x)u_j, \qquad j = 0, 1. \tag{22}$$

Alternatively, if $\mathcal{F}(0) \neq 0$, the power-series expansion of the function about $x = 0$ gives

$$\begin{aligned}\mathcal{F}(xu_j) &= \sum_{n=0}^{\infty} c_n (xu_j)^n \\ &= c_0 I + \sum_{n=1}^{\infty} c_n x^n u_j \\ &= \mathcal{F}(0)I + u_j \sum_{n=1}^{\infty} c_n x^n \\ &= \mathcal{F}(0)I + \big[\mathcal{F}(x) - \mathcal{F}(0)\big]u_j \\ &= \mathcal{F}(x)u_j + \mathcal{F}(0)(I - u_j).\end{aligned} \tag{23}$$

Since the projectors are complementary, $u_0 + u_1 = I$ and $u_0 u_1 = u_1 u_0 = 0$, we obtain, in particular, for $\mathcal{F}(0) \neq 0$,

$$\begin{aligned}\mathcal{F}(xu_0) &= \mathcal{F}(x)u_0 + \mathcal{F}(0)u_1 = \begin{pmatrix} \mathcal{F}(x) & 0 \\ 0 & \mathcal{F}(0) \end{pmatrix}, \\ \mathcal{F}(xu_1) &= \mathcal{F}(0)u_0 + \mathcal{F}(x)u_1 = \begin{pmatrix} \mathcal{F}(0) & 0 \\ 0 & \mathcal{F}(x) \end{pmatrix}.\end{aligned} \tag{24}$$

If the argument of an analytic function is a linear combination of two complementary projectors u_j, the projectors can be extracted from the function:

$$\mathcal{F}(xu_0 + yu_1) = \mathcal{F}(x)u_0 + \mathcal{F}(y)u_1. \tag{25}$$

Returning to the density operator of a two-level system, we can write, using the new notation,

$$\begin{aligned}\rho &= \frac{1}{Z(\beta)} \sum_{n=0}^{1} e^{-\beta E_n} |n\rangle\langle n| \\ &= \frac{1}{Z(\beta)} \left(e^{-\beta E_0} u_0 + e^{-\beta E_1} u_1\right) \\ &= \frac{1}{Z(\beta)} \begin{pmatrix} e^{-\beta E_0} & 0 \\ 0 & e^{-\beta E_1} \end{pmatrix}.\end{aligned} \tag{26}$$

The partition function $Z(\beta)$ is obtained from the normalization condition $\operatorname{Tr} \rho = 1$:

$$\begin{aligned}Z(\beta) &= \sum_{m=0}^{1} \langle m|e^{-\beta H}|m\rangle \\ &= \sum_{n=0}^{1} e^{-\beta E_n} = e^{-\beta E_0} + e^{-\beta E_1}.\end{aligned} \tag{27}$$

For this case, the density operator is a 2×2 diagonal matrix.

$$\begin{aligned}\rho &= \frac{1}{1 + e^{-\beta(E_1 - E_0)}} u_0 + \frac{1}{1 + e^{\beta(E_1 - E_0)}} u_1 \\ &= \begin{pmatrix} \dfrac{1}{1 + e^{-\beta(E_1 - E_0)}} & 0 \\ 0 & \dfrac{1}{1 + e^{\beta(E_1 - E_0)}} \end{pmatrix}.\end{aligned} \tag{28}$$

From this expression, the trace of the operator is seen to be equal to unity:

$$\operatorname{Tr} \rho = \frac{1}{1 + e^{-\beta(E_1 - E_0)}} + \frac{1}{1 + e^{\beta(E_1 - E_0)}} = 1. \tag{29}$$

3 Coherent states with shifted arguments

In a previous paper [13], we derived the expression for generalized coherent states with a displaced or shifted argument. This type of coherent state has as its argument a linear combination of two complex variables z and σ, with two real numbers ε and λ as coefficients. Below, we present the main results on coherent states with a shifted argument obtained in that paper. These results will help us examine the case considered here.

We use the following pair of nonlinear adjoint annihilation and creation operators:

$$\widehat{A} = \widehat{a}\, {}_p f_q(\widehat{N}), \qquad \widehat{A}^\dagger = {}_p f_q(\widehat{N})\, \widehat{a}^\dagger. \tag{30}$$

Here, ${}_p f_q(\widehat{N})$ is the deformation function depending on the number operator $\widehat{N} = \widehat{a}^\dagger \widehat{a}$, and p and q are positive integers. The deformation function changes the usual canonical commutation relation $[\widehat{a}, \widehat{a}^\dagger] = 1$ into a deformed Heisenberg algebra. It satisfies

$${}_p f_q(\widehat{N} + m)|n + s\rangle = {}_p f_q(n + s + m)|n + s\rangle. \tag{31}$$

$$\begin{aligned}{}_p f_q(\widehat{N}) &= \sqrt{\frac{\prod_{j=1}^{q} (b_j - 1 + \widehat{N})}{\prod_{i=1}^{p} (a_i - 1 + \widehat{N})}}, \\ {}_p f_q(\widehat{N})|n\rangle &= \sqrt{\frac{\prod_{j=1}^{q} (b_j - 1 + n)}{\prod_{i=1}^{p} (a_i - 1 + n)}}\, |n\rangle.\end{aligned} \tag{32}$$

The actions of these operators and their adjoints on the Fock vectors are

$$\begin{aligned}
&\widehat{A}|n\rangle = \sqrt{{}_pe_q(n)}\,|n-1\rangle,\\
&\langle n|\widehat{A}^\dagger = \sqrt{{}_pe_q(n)}\,\langle n-1|,\\
&\widehat{A}^\dagger|n\rangle = \sqrt{{}_pe_q(n+1)}\,|n+1\rangle,\\
&\langle n|\widehat{A} = \sqrt{{}_pe_q(n+1)}\,\langle n+1|,\\
&\langle n|\widehat{A}^\dagger\widehat{A}|n\rangle = {}_pe_q(n).
\end{aligned} \tag{33}$$

We use the notation

$${}_pe_q(n) \equiv n\big[{}_pf_q(n)\big]^2 = n\,\frac{\prod_{j=1}^{q}(b_j-1+n)}{\prod_{i=1}^{p}(a_i-1+n)}. \tag{34}$$

The repeated action of the creation operator on the vacuum state leads to

$$\begin{aligned}
(\widehat{A}^\dagger)^n|0\rangle &= \sqrt{\prod_{s=1}^{n}{}_pe_q(s)}\,|n\rangle = \sqrt{{}_p\rho_q(n)}\,|n\rangle,\\
\langle 0|(\widehat{A})^n &= \langle n|\sqrt{\prod_{s=1}^{n}{}_pe_q(s)} = \langle n|\sqrt{{}_p\rho_q(n)}.
\end{aligned} \tag{35}$$

The newly introduced quantity is called the structure function because it determines the internal structure of coherent states:

$$\begin{aligned}
{}_p\rho_q(n) &\equiv \prod_{s=1}^{n}{}_pe_q(s) = n!\,\frac{\prod_{j=1}^{q}(b_j)_n}{\prod_{i=1}^{p}(a_i)_n}\\
&= \Gamma(a/b)\,\Gamma(n+1)\,\frac{\prod_{j=1}^{q}\Gamma(b_j+n)}{\prod_{i=1}^{p}\Gamma(a_i+n)},
\end{aligned} \tag{36}$$

$$\Gamma(a/b) \equiv \frac{\prod_{i=1}^{p}\Gamma(a_i)}{\prod_{j=1}^{q}\Gamma(b_j)}.$$

Instead of the usual binomial coefficients, generalized binomial coefficients appear in the calculations. They are defined as follows:

$$\binom{{}_p\rho_q(l)}{{}_p\rho_q(n)} \equiv \frac{{}_p\rho_q(l)}{{}_p\rho_q(n)\,{}_p\rho_q(l-n)}. \tag{37}$$

Generalized binomial coefficients enter the calculation of coherent states with a shifted argument when a product of two shift operators, each depending on a single complex variable, is applied to the vacuum state [13]. A generalized Newton binomial expression is also used. This quantity is denoted by square brackets, $[x+y]^l$, and defined as

$$[x+y]^l \equiv \sum_{m=0}^{l}\binom{{}_p\rho_q(l)}{{}_p\rho_q(m)}x^{l-m}y^m. \tag{38}$$

The coherent states with a shifted argument are labelled by a complex number Z, which is a linear combination of two ordinary complex variables z and σ, with real coefficients ε and λ:

$$\begin{aligned}
Z &= \varepsilon z + \lambda\sigma\\
&= \operatorname{Re} Z + i\operatorname{Im} Z = |Z|\exp(i\varphi_Z).
\end{aligned} \tag{39}$$

In deriving the expression for generalized coherent states with shifted arguments [13], we used the generalized displacement operator

$$\widehat{\mathcal{D}}(z) \equiv \frac{{}_pF_q(z\widehat{A}^\dagger)}{\sqrt{{}_pF_q(|z|^2)}}, \tag{40}$$

which agrees with the construction discussed in Ref. [11].

To simplify the notation, whenever there is no risk of confusion, we omit the parameter sets $a = \{a_i\}_{i=1}^{p}$ and $b = \{b_j\}_{j=1}^{q}$ from the generalized hypergeometric functions. Thus, we write ${}_pF_q(x)$ instead of ${}_pF_q(a;b;x)$, where

$$\begin{aligned}
{}_pF_q(a;b;x) &\equiv {}_pF_q(x)\\
&= \sum_{n=0}^{\infty}\frac{\prod_{i=1}^{p}(a_i)_n}{\prod_{j=1}^{q}(b_j)_n}\frac{x^n}{n!} = \sum_{n=0}^{\infty}\frac{x^n}{{}_p\rho_q(n)}.
\end{aligned} \tag{41}$$

Consequently, coherent states whose argument is a linear combination of complex numbers are defined using the generalized displacement operator $\widehat{\mathcal{D}}(\varepsilon z+\lambda\sigma) = \widehat{\mathcal{D}}(\lambda\sigma)\widehat{\mathcal{D}}(\varepsilon z)$, which acts on the vacuum state:

$$|Z\rangle \equiv |\varepsilon z+\lambda\sigma\rangle \longrightarrow \widehat{\mathcal{D}}(\lambda\sigma)\widehat{\mathcal{D}}(\varepsilon z)|0\rangle. \tag{42}$$

After simple calculations, the final expression for the generalized displaced, or shifted, argument is obtained as

$$\begin{aligned}
|\varepsilon z+\lambda\sigma\rangle = &\sqrt{\frac{{}_pF_q(|\lambda\sigma|^2)\,{}_pF_q(|\varepsilon z|^2)}{{}_pF_q(|\varepsilon z+\lambda\sigma|^2)}}\\
&\times\widehat{\mathcal{D}}(\lambda\sigma)\widehat{\mathcal{D}}(\varepsilon z)|0\rangle.
\end{aligned} \tag{43}$$

Equivalently, its expansion with respect to the Fock vectors is

$$|\varepsilon z+\lambda\sigma\rangle = \frac{1}{\sqrt{{}_pF_q(|\varepsilon z+\lambda\sigma|^2)}} \times \sum_{n=0}^{\infty} \frac{[\varepsilon z+\lambda\sigma]^n}{\sqrt{{}_p\rho_q(n)}}\,|n\rangle. \tag{44}$$

This can also be written in the following form:

$$|\varepsilon z+\lambda\sigma\rangle = \frac{1}{\sqrt{{}_pF_q(|\varepsilon z+\lambda\sigma|^2)}} \times {}_pF_q\big([\varepsilon z+\lambda\sigma]\widehat{A}^\dagger\big)|0\rangle, \tag{45}$$

and similarly for its complex-conjugate counterpart.

Using the variable $Z=\varepsilon z+\lambda\sigma$, the coherent states can be written as

$$\begin{aligned}|Z\rangle &= \frac{1}{\sqrt{{}_pF_q(|Z|^2)}}\sum_{n=0}^{\infty}\frac{[Z]^n}{\sqrt{{}_p\rho_q(n)}}\,|n\rangle \\ &= \frac{1}{\sqrt{{}_pF_q(|Z|^2)}}{}_pF_q\big([Z]\widehat{A}^\dagger\big)|0\rangle,\end{aligned} \tag{46}$$

$$\begin{aligned}\langle Z| &= \frac{1}{\sqrt{{}_pF_q(|Z|^2)}}\sum_{n=0}^{\infty}\frac{[Z^*]^n}{\sqrt{{}_p\rho_q(n)}}\,\langle n| \\ &= \frac{1}{\sqrt{{}_pF_q(|Z|^2)}}\langle 0|\,{}_pF_q\big([Z^*]\widehat{A}\big).\end{aligned} \tag{47}$$

4 Coherent states with matrix arguments

Let us consider a complex variable Z with a diagonal matrix structure, that is, a sum of two complex numbers z and σ, each multiplied by a 2×2 matrix:

$$\begin{aligned}Z &= \begin{pmatrix} z & 0\\ 0 & \sigma\end{pmatrix} \\ &= z\begin{pmatrix}1&0\\0&0\end{pmatrix}+\sigma\begin{pmatrix}0&0\\0&1\end{pmatrix} \\ &= zu_0+\sigma u_1.\end{aligned} \tag{48}$$

Thus, Z is a 2×2 diagonal matrix whose main diagonal entries are the ordinary complex numbers z and σ. These are also the expansion coefficients of a linear combination of the two singular diagonal square matrices u_j, $j=0,1$.

Using the results obtained for coherent states with a shifted argument, let us examine the corresponding properties of coherent states whose argument is a linear combination of two complex numbers multiplying singular diagonal square 2×2 matrices.

First, let us make the following identifications:

$$\begin{aligned}&\varepsilon z+\lambda\sigma \equiv zu_0+\sigma u_1,\\ &\varepsilon \equiv u_0 = \begin{pmatrix}1&0\\0&0\end{pmatrix},\\ &\lambda \equiv u_1 = \begin{pmatrix}0&0\\0&1\end{pmatrix}.\end{aligned} \tag{49}$$

For this form of the complex number Z, the generalized Newton binomial expression simplifies considerably, taking into account the properties of the matrices u_j:

$$\begin{aligned}[Z]^l &\equiv [zu_0+\sigma u_1]^l \\ &= \sum_{m=0}^{l}\binom{{}_p\rho_q(l)}{{}_p\rho_q(m)}(zu_0)^{l-m}(\sigma u_1)^m \\ &= (zu_0)^l+(\sigma u_1)^l \\ &= z^l u_0+\sigma^l u_1.\end{aligned} \tag{50}$$

Only the terms involving a single projector survive, because the mixed products of u_0 and u_1 vanish.

In particular, we have

$$\begin{aligned}|Z|^2 &\equiv ZZ^* \\ &= (zu_0+\sigma u_1)(z^*u_0+\sigma^*u_1) \\ &= |z|^2u_0+|\sigma|^2u_1.\end{aligned} \tag{51}$$

The powers of Z can therefore be written as 2×2 diagonal matrices:

$$Z^m = z^m u_0+\sigma^m u_1 = \begin{pmatrix}z^m&0\\0&\sigma^m\end{pmatrix}. \tag{52}$$

We can apply the same procedure to the generalized hypergeometric function.

According to the considerations in Ref. [13], the expression for coherent states with a matrix argument is

$$|zu_0+\sigma u_1\rangle = \frac{1}{\sqrt{{}_pF_q(|zu_0+\sigma u_1|^2)}} \times \sum_{n=0}^{\infty}\frac{(zu_0+\sigma u_1)^n}{\sqrt{{}_p\rho_q(n)}}\,|n\rangle. \tag{53}$$

$$\begin{aligned}{}_pF_q(|Z|^2) &= \sum_{n=0}^{\infty}c_n(|Z|^2)^n \\ &= \sum_{n=0}^{\infty}c_n\big(|z|^2u_0+|\sigma|^2u_1\big)^n \\ &= u_0\sum_{n=0}^{\infty}c_n(|z|^2)^n+u_1\sum_{n=0}^{\infty}c_n(|\sigma|^2)^n \\ &= u_0\,{}_pF_q(|z|^2)+u_1\,{}_pF_q(|\sigma|^2).\end{aligned} \tag{54}$$

Using the properties of u_0 and u_1, namely $(u_j)^m = u_j$ for $m \geq 1$ and $u_i u_j = u_j u_i = 0$ for $i \neq j$, the normalization function of the coherent states with shifted arguments separates into two parts, each depending on one variable:

$$
\begin{aligned}
{}_pF_q(|zu_0 + \sigma u_1|^2) = u_0\, {}_pF_q(|z|^2) \\
+ u_1\, {}_pF_q(|\sigma|^2).
\end{aligned}
\tag{55}
$$

From a mathematical point of view, this relation represents a matrix version of Cauchy's functional equation, whose general expression is

$$
\mathcal{F}(x+y) = \mathcal{F}(x) + \mathcal{F}(y). \tag{56}
$$

In the case examined here, where the argument of the coherent states is matrix-valued, these relations can be written as follows.

$$
\begin{aligned}
\mathcal{F}(xu_0 + yu_1) &= \mathcal{F}(xu_0) + \mathcal{F}(yu_1) \\
&= \mathcal{F}(x)u_0 + \mathcal{F}(y)u_1.
\end{aligned}
\tag{57}
$$

The product of two such functions is

$$
\begin{aligned}
&\mathcal{F}(xu_0 + yu_1)\mathcal{G}(su_0 + \xi u_1) \\
&\quad = \big[\mathcal{F}(x)u_0 + \mathcal{F}(y)u_1\big]\big[\mathcal{G}(s)u_0 + \mathcal{G}(\xi)u_1\big] \\
&\quad = \mathcal{F}(x)\mathcal{G}(s)u_0 + \mathcal{F}(y)\mathcal{G}(\xi)u_1.
\end{aligned}
\tag{58}
$$

Since the matrices u_0 and u_1 are idempotent, they can be removed from the arguments of the respective functions, so that expressions involving two independent complex variables decouple:

$$
f\big(|z|^2u_0 + |\sigma|^2u_1\big) = u_0 f(|z|^2) + u_1 f(|\sigma|^2). \tag{59}
$$

Writing the complete coherent state $|zu_0 + \sigma u_1\rangle$ as an expansion over the basis vectors $|n\rangle$, we obtain

$$
\begin{aligned}
|zu_0 + \sigma u_1\rangle &= \big[{}_pF_q(|z|^2)u_0 + {}_pF_q(|\sigma|^2)u_1\big]^{-1/2} \\
&\quad \times \left(u_0 \sum_{n=0}^{\infty} \frac{z^n}{\sqrt{{}_p\rho_q(n)}}|n\rangle \right. \\
&\quad \left. + u_1 \sum_{n=0}^{\infty} \frac{\sigma^n}{\sqrt{{}_p\rho_q(n)}}|n\rangle \right) \\
&= u_0 \frac{\sqrt{{}_pF_q(|z|^2)}\, u_0}{\sqrt{{}_pF_q(|z|^2)u_0 + {}_pF_q(|\sigma|^2)u_1}}\,|z\rangle \\
&\quad + u_1 \frac{\sqrt{{}_pF_q(|\sigma|^2)}\, u_1}{\sqrt{{}_pF_q(|z|^2)u_0 + {}_pF_q(|\sigma|^2)u_1}}\,|\sigma\rangle,
\end{aligned}
\tag{60}
$$

where the coherent states associated with the individual variables are

$$
\begin{aligned}
|zu_0\rangle &\longrightarrow u_0 \frac{1}{\sqrt{{}_pF_q(|z|^2)}} \sum_{n=0}^{\infty} \frac{z^n}{\sqrt{{}_p\rho_q(n)}}|n\rangle, \\
|\sigma u_1\rangle &\longrightarrow u_1 \frac{1}{\sqrt{{}_pF_q(|\sigma|^2)}} \sum_{n=0}^{\infty} \frac{\sigma^n}{\sqrt{{}_p\rho_q(n)}}|n\rangle.
\end{aligned}
\tag{61}
$$

The normalization of each component is projector-valued:

$$
\begin{aligned}
&\langle zu_0|zu_0\rangle = \langle z|u_0^2|z\rangle = u_0, \\
&\langle \sigma u_1|\sigma u_1\rangle = \langle \sigma|u_1^2|\sigma\rangle = u_1, \\
&\langle zu_0|\sigma u_1\rangle = \langle z|u_0u_1|\sigma\rangle = 0.
\end{aligned}
\tag{62}
$$

Thus,

$$
\langle zu_0|zu_0\rangle + \langle \sigma u_1|\sigma u_1\rangle = u_0 + u_1 = I. \tag{63}
$$

In the above relations, the coherent states $|z\rangle$ are not ordinary vectors but matrix-valued vectors. The Fock vectors $|n\rangle$ are column vectors, whereas the coherent states are linear combinations with matrix coefficients. In expanded form, we can write

$$
\begin{aligned}
|z\rangle \longrightarrow \frac{1}{\sqrt{{}_pF_q(|z|^2)}} \left[\frac{1}{\sqrt{{}_p\rho_q(0)}}|0\rangle \right. \\
+ \frac{z}{\sqrt{{}_p\rho_q(1)}}|1\rangle + \cdots \\
\left. + \frac{z^n}{\sqrt{{}_p\rho_q(n)}}|n\rangle + \cdots \right].
\end{aligned}
\tag{64}
$$

The partial conclusion is that coherent states whose argument is a sum of two terms can be written as a linear combination of coherent states associated with the separate terms, with matrix-valued weights.

$$
\begin{aligned}
\mathcal{P}_{zu_0} &\equiv \frac{u_0\sqrt{{}_pF_q(|z|^2)}}{\sqrt{{}_pF_q(|z|^2)u_0 + {}_pF_q(|\sigma|^2)u_1}}, \\
\mathcal{P}_{\sigma u_1} &\equiv \frac{u_1\sqrt{{}_pF_q(|\sigma|^2)}}{\sqrt{{}_pF_q(|z|^2)u_0 + {}_pF_q(|\sigma|^2)u_1}}.
\end{aligned}
\tag{65}
$$

In short, we write

$$
|zu_0 + \sigma u_1\rangle = \mathcal{P}_{zu_0}|z\rangle u_0 + \mathcal{P}_{\sigma u_1}|\sigma\rangle u_1. \tag{66}
$$

It is not difficult to verify that these coherent states are normalized:

$$
\begin{aligned}
&\langle zu_0 + \sigma u_1|zu_0 + \sigma u_1\rangle \\
&= \big(\mathcal{P}_{zu_0}u_0\langle z| + \mathcal{P}_{\sigma u_1}u_1\langle\sigma|\big) \\
&\quad \times \big(\mathcal{P}_{zu_0}|z\rangle u_0 + \mathcal{P}_{\sigma u_1}|\sigma\rangle u_1\big) \\
&= (\mathcal{P}_{zu_0})^2 + (\mathcal{P}_{\sigma u_1})^2 = I.
\end{aligned}
\tag{67}
$$

Their associated projector is

$$
\begin{aligned}
&|zu_0 + \sigma u_1\rangle\langle zu_0 + \sigma u_1| \\
&= \big(\mathcal{P}_{zu_0}|z\rangle u_0 + \mathcal{P}_{\sigma u_1}|\sigma\rangle u_1\big) \\
&\quad \times \big(\mathcal{P}_{zu_0}\langle z|u_0 + \mathcal{P}_{\sigma u_1}\langle\sigma|u_1\big) \\
&= (\mathcal{P}_{zu_0})^2|z\rangle\langle z|u_0 + (\mathcal{P}_{\sigma u_1})^2|\sigma\rangle\langle\sigma|u_1.
\end{aligned}
\tag{68}
$$

The following limits reduce the coherent states with a matrix argument to coherent states labelled by a single variable:

$$
\begin{aligned}
&\lim_{z\to 0} |zu_0 + \sigma u_1\rangle = u_1|\sigma\rangle, \\
&\lim_{\sigma\to 0} |zu_0 + \sigma u_1\rangle = u_0|z\rangle.
\end{aligned}
\tag{69}
$$

Particular case 1: One-dimensional quantum harmonic oscillator. For $p = q = 0$, with empty parameter sets $\{a_i\}$ and $\{b_j\}$, the generalized hypergeometric function becomes ${}_0F_0(x) = \exp(x)$. The coherent states with a matrix argument are then written as

$$\begin{aligned}|zu_0+\sigma u_1\rangle &= \frac{1}{\sqrt{e^{|z|^2}u_0+e^{|\sigma|^2}u_1}} \\ &\quad\times\left(u_0\sum_{n=0}^{\infty}\frac{z^n}{\sqrt{n!}}|n\rangle\right. \\ &\quad\left.+u_1\sum_{n=0}^{\infty}\frac{\sigma^n}{\sqrt{n!}}|n\rangle\right) \\ &= \frac{1}{\sqrt{e^{|z|^2}u_0+e^{|\sigma|^2}u_1}} \\ &\quad\times\left(u_0e^{|z|^2/2}|z\rangle+u_1e^{|\sigma|^2/2}|\sigma\rangle\right) \\ &= \frac{e^{|z|^2/2}}{\sqrt{e^{|z|^2}u_0+e^{|\sigma|^2}u_1}}\,|z\rangle u_0 \\ &\quad+\frac{e^{|\sigma|^2/2}}{\sqrt{e^{|z|^2}u_0+e^{|\sigma|^2}u_1}}\,|\sigma\rangle u_1.\end{aligned} \tag{70}$$

The normalization follows by calculating the scalar product:

$$\begin{aligned}&\langle zu_0+\sigma u_1|zu_0+\sigma u_1\rangle \\ &= \frac{1}{e^{|z|^2}u_0+e^{|\sigma|^2}u_1} \\ &\quad\times\left(u_0e^{|z|^2/2}\langle z|+u_1e^{|\sigma|^2/2}\langle\sigma|\right) \\ &\quad\times\left(u_0e^{|z|^2/2}|z\rangle+u_1e^{|\sigma|^2/2}|\sigma\rangle\right) \\ &= \frac{e^{|z|^2}u_0+e^{|\sigma|^2}u_1}{e^{|z|^2}u_0+e^{|\sigma|^2}u_1} = I.\end{aligned} \tag{71}$$

This case corresponds to the one-dimensional quantum harmonic oscillator and hence to canonical coherent states.

As a side note, the denominator above is a full diagonal matrix. In accordance with the general power-series expansion,

$$\mathcal{F}(xu_j) = \mathcal{F}(x)u_j + \mathcal{F}(0)(I-u_j), \tag{72}$$

we recall the following useful relations:

$$e^xu_0+e^yu_1 = \begin{pmatrix}e^x&0\\0&0\end{pmatrix}+\begin{pmatrix}0&0\\0&e^y\end{pmatrix} = \begin{pmatrix}e^x&0\\0&e^y\end{pmatrix}. \tag{73}$$

$$\begin{aligned}e^{xu_j} &= I+(e^x-1)u_j, \qquad j=0,1, \\ e^{xu_0} &= e^xu_0+u_1 = \begin{pmatrix}e^x&0\\0&1\end{pmatrix}, \\ e^{xu_1} &= u_0+e^xu_1 = \begin{pmatrix}1&0\\0&e^x\end{pmatrix}.\end{aligned} \tag{74}$$

$$\begin{aligned}e^{xu_0}+e^{yu_1} &= \begin{pmatrix}e^x&0\\0&1\end{pmatrix}+\begin{pmatrix}1&0\\0&e^y\end{pmatrix} \\ &= \begin{pmatrix}e^x+1&0\\0&e^y+1\end{pmatrix}.\end{aligned} \tag{75}$$

$$\begin{aligned}e^{xu_0}+e^{xu_1} &= \begin{pmatrix}e^x+1&0\\0&e^x+1\end{pmatrix} \\ &= (e^x+1)I.\end{aligned} \tag{76}$$

For real x and y, using the principal matrix logarithm,

$$\ln(e^{xu_j}) = \ln(e^x)\,u_j = xu_j. \tag{77}$$

$$\ln(e^xu_0+e^yu_1) = xu_0+yu_1. \tag{78}$$

Particular case 2—A two-level system.

For a two-level system, we have

$$\begin{aligned}|zu_0+\sigma u_1\rangle &= \frac{1}{\sqrt{u_0\,{}_pF_q(|z|^2)+u_1\,{}_pF_q(|\sigma|^2)}} \\ &\quad\times\left(u_0\sum_{n=0}^{1}\frac{z^n}{\sqrt{{}_p\rho_q(n)}}|n\rangle+u_1\sum_{n=0}^{1}\frac{\sigma^n}{\sqrt{{}_p\rho_q(n)}}|n\rangle\right).\end{aligned} \tag{79}$$

$$\begin{aligned}\langle zu_0+\sigma u_1| &= \frac{1}{\sqrt{u_0\,{}_pF_q(|z|^2)+u_1\,{}_pF_q(|\sigma|^2)}} \\ &\quad\times\left(u_0\sum_{n=0}^{1}\frac{(z^*)^n}{\sqrt{{}_p\rho_q(n)}}\langle n|+u_1\sum_{n=0}^{1}\frac{(\sigma^*)^n}{\sqrt{{}_p\rho_q(n)}}\langle n|\right).\end{aligned} \tag{80}$$

The corresponding inner product is

$$\begin{aligned}&\langle zu_0+\sigma u_1\mid zu_0+\sigma u_1\rangle \\ &\quad= \frac{1}{u_0\,{}_pF_q(|z|^2)+u_1\,{}_pF_q(|\sigma|^2)} \\ &\qquad\times\left(u_0\sum_{n=0}^{1}\frac{(|z|^2)^n}{{}_p\rho_q(n)}+u_1\sum_{n=0}^{1}\frac{(|\sigma|^2)^n}{{}_p\rho_q(n)}\right),\end{aligned} \tag{81}$$

where

$${}_p\rho_q(0) = 1, \qquad {}_p\rho_q(1) = \frac{\prod_{j=1}^{q}b_j}{\prod_{i=1}^{p}a_i} \neq 0. \tag{82}$$

Coherent states with a shifted argument satisfy the completeness relation, or resolution of the identity operator, which is a fundamental property in constructing coherent states:

$$\int \mathrm{d}\mu(\varepsilon z+\lambda\sigma)\,|\varepsilon z+\lambda\sigma\rangle\langle\varepsilon z+\lambda\sigma| = I. \tag{83}$$

With $Z = \varepsilon z + \lambda\sigma$, this condition becomes

$$\int \mathrm{d}\mu(Z)\,|Z\rangle\langle Z| = I. \tag{84}$$

The corresponding integration measure on the integration domain is [23]

$$\begin{aligned}\mathrm{d}\mu(Z) &= \Gamma(a/b)\,\frac{\mathrm{d}^2 Z}{\pi}\\ &\times G^{q+1,0}_{p,q+1}\left(|Z|^2\,\middle|\,\begin{matrix}-;\,\{a_i-1\}_{i=1}^{p}\\ 0,\{b_j-1\}_{j=1}^{q};\,-\end{matrix}\right){}_pF_q(|Z|^2).\end{aligned} \tag{85}$$

Equivalently, in terms of the shifted argument,

$$\begin{aligned}\mathrm{d}\mu(\varepsilon z+\lambda\sigma) &= \Gamma(a/b)\,\mathrm{d}\big(|\varepsilon z+\lambda\sigma|^2\big)\,\frac{\mathrm{d}\varphi_Z}{2\pi}\\ &\times G^{q+1,0}_{p,q+1}\left(|\varepsilon z+\lambda\sigma|^2\,\middle|\,\begin{matrix}-;\,\{a_i-1\}_{i=1}^{p}\\ 0,\{b_j-1\}_{j=1}^{q};\,-\end{matrix}\right)\\ &\times {}_pF_q\big(|\varepsilon z+\lambda\sigma|^2\big)\,.\end{aligned} \tag{86}$$

To simplify the formulas, whenever there is no risk of confusion, we use a shorthand notation for Meijer's G-function, suppressing its parameters and displaying only its argument:

$$\begin{aligned}G^{q+1,0}_{p,q+1}\left(x\,\middle|\,\begin{matrix}-;\,\{a_i-1\}_{i=1}^{p}\\ 0,\{b_j-1\}_{j=1}^{q};\,-\end{matrix}\right) &\equiv G^{q+1,0}_{p,q+1}(x\mid\cdots),\\ \Phi(s;a-1,b-1) &= \frac{\Gamma(-s)\prod_{j=1}^{q}\Gamma(b_j-1-s)}{\prod_{i=1}^{p}\Gamma(a_i-1-s)}.\end{aligned} \tag{87}$$

We now consider the completeness condition for coherent states with a matrix argument. In this case, the projectors u_0 and u_1 replace the constants ε and λ, respectively: $\varepsilon = u_0$ and $\lambda = u_1$. Thus,

$$\begin{aligned}&\int \mathrm{d}\mu(zu_0+\sigma u_1)\,|zu_0+\sigma u_1\rangle\langle zu_0+\sigma u_1|\\ &\quad=\int \mathrm{d}\mu(zu_0+\sigma u_1)\Big[\big(\mathcal{P}_{zu_0}\big)^2|z\rangle\langle z|u_0\\ &\qquad\qquad+\big(\mathcal{P}_{\sigma u_1}\big)^2|\sigma\rangle\langle\sigma|u_1\Big] = I.\end{aligned} \tag{88}$$

With these substitutions, the corresponding integration measure is written as

$$\begin{aligned}\mathrm{d}\mu(zu_0+\sigma u_1) &= \Gamma(a/b)\,\frac{\mathrm{d}^2(zu_0+\sigma u_1)}{\pi}\\ &\times G^{q+1,0}_{p,q+1}\left(|zu_0|^2+|\sigma u_1|^2\,\middle|\cdots\right)\\ &\times {}_pF_q\big(u_0|z|^2+u_1|\sigma|^2\big)\,.\end{aligned} \tag{89}$$

The differential associated with $Z = zu_0 + \sigma u_1$ is written formally in terms of the two independent complex variables z and σ as follows:

$$\begin{aligned}\frac{\mathrm{d}^2 Z}{\pi} &\equiv \frac{\mathrm{d}^2(zu_0+\sigma u_1)}{\pi}\\ &= \frac{\partial}{\partial z}(zu_0+\sigma u_1)\frac{\mathrm{d}^2 z}{\pi}\\ &\quad+\frac{\partial}{\partial\sigma}(zu_0+\sigma u_1)\frac{\mathrm{d}^2\sigma}{\pi}\\ &= \frac{\mathrm{d}^2 z}{\pi}u_0+\frac{\mathrm{d}^2\sigma}{\pi}u_1\\ &= \frac{\mathrm{d}\varphi_z}{2\pi}\mathrm{d}(|z|^2)u_0+\frac{\mathrm{d}\varphi_\sigma}{2\pi}\mathrm{d}(|\sigma|^2)u_1.\end{aligned} \tag{90}$$

First, we examine Meijer's G-function appearing in the integration measure. Using its integral representation [18], we obtain

$$\begin{aligned}&G^{q+1,0}_{p,q+1}\left(x\,\middle|\,\begin{matrix}-;\,\{a_i-1\}_{i=1}^{p}\\ 0,\{b_j-1\}_{j=1}^{q};\,-\end{matrix}\right)\\ &\quad=\frac{1}{2\pi\mathrm{i}}\int_{\mathcal{L}}\frac{\Gamma(-s)\prod_{j=1}^{q}\Gamma(b_j-1-s)}{\prod_{i=1}^{p}\Gamma(a_i-1-s)}x^s\,\mathrm{d}s\\ &\quad\equiv\frac{1}{2\pi\mathrm{i}}\int_{\mathcal{L}}\Phi(s;a-1,b-1)\,x^s\,\mathrm{d}s.\end{aligned} \tag{91}$$

In our case, this gives

$$\begin{aligned}&G^{q+1,0}_{p,q+1}(|Z|^2\mid\cdots)\\ &\quad=G^{q+1,0}_{p,q+1}\left(|z|^2u_0+|\sigma|^2u_1\,\middle|\cdots\right)\\ &\quad=\frac{1}{2\pi\mathrm{i}}\int_{\mathcal{L}}\Phi(s;a-1,b-1)\left(|z|^2u_0+|\sigma|^2u_1\right)^s\mathrm{d}s\\ &\quad=\frac{u_0}{2\pi\mathrm{i}}\int_{\mathcal{L}}\Phi(s;a-1,b-1)(|z|^2)^s\,\mathrm{d}s\\ &\qquad+\frac{u_1}{2\pi\mathrm{i}}\int_{\mathcal{L}}\Phi(s;a-1,b-1)(|\sigma|^2)^s\,\mathrm{d}s\\ &\quad=u_0G^{q+1,0}_{p,q+1}(|z|^2\mid\cdots)+u_1G^{q+1,0}_{p,q+1}(|\sigma|^2\mid\cdots).\end{aligned} \tag{92}$$

Thus, the matrix-valued Meijer G-function decomposes into two scalar functions, depending on $|z|^2$ and $|\sigma|^2$, respectively.

Using these results, the integration measure becomes

$$\begin{aligned}&\mathrm{d}\mu(zu_0+\sigma u_1)\\ &\quad=\Gamma(a/b)\left[u_0\frac{\mathrm{d}\varphi_z}{2\pi}\mathrm{d}(|z|^2)+u_1\frac{\mathrm{d}\varphi_\sigma}{2\pi}\mathrm{d}(|\sigma|^2)\right]\\ &\qquad\times\left[u_0\,{}_pF_q(|z|^2)+u_1\,{}_pF_q(|\sigma|^2)\right]\\ &\qquad\times\Big[u_0G^{q+1,0}_{p,q+1}(|z|^2\mid\cdots)\\ &\qquad\qquad+u_1G^{q+1,0}_{p,q+1}(|\sigma|^2\mid\cdots)\Big]\,.\end{aligned} \tag{93}$$

Using the properties of the projectors, this expression can be simplified further.

$$\begin{aligned}\mathrm{d}\mu(zu_0+\sigma u_1) &= u_0\Gamma(a/b)\left[\frac{\mathrm{d}\varphi_z}{2\pi}\mathrm{d}(|z|^2)\right.\\ &\quad\left.\times\, G^{q+1,0}_{p,q+1}(|z|^2\mid\cdots)\,{}_pF_q(|z|^2)\right]\\ &\quad+u_1\Gamma(a/b)\left[\frac{\mathrm{d}\varphi_\sigma}{2\pi}\mathrm{d}(|\sigma|^2)\right.\\ &\quad\left.\times\, G^{q+1,0}_{p,q+1}(|\sigma|^2\mid\cdots)\,{}_pF_q(|\sigma|^2)\right]\\ &\equiv u_0\,\mathrm{d}\mu(z)+u_1\,\mathrm{d}\mu(\sigma).\end{aligned}\tag{94}$$

The resolution of the identity therefore becomes

$$\begin{aligned}&u_0\left[\int \mathrm{d}\mu(z)\left(\mathcal{P}_{zu_0}\right)^2|z\rangle\langle z|\right]\\ &\quad+u_1\left[\int \mathrm{d}\mu(\sigma)\left(\mathcal{P}_{\sigma u_1}\right)^2|\sigma\rangle\langle\sigma|\right]=I.\end{aligned}\tag{95}$$

The projector associated with the coherent state labelled by z is

$$\begin{aligned}|z\rangle\langle z| &= \frac{1}{{}_pF_q(|z|^2)}\\ &\quad\times\left[\sum_{n,m=0}^{\infty}\frac{z^n(z^*)^m}{\sqrt{{}_p\rho_q(n)}\sqrt{{}_p\rho_q(m)}}|n\rangle\langle m|\right],\end{aligned}\tag{96}$$

with an analogous expression for the variable σ.

We now integrate the first component:

$$\begin{aligned}\mathrm{Int}_z &\equiv u_0\left[\int \mathrm{d}\mu(z)\left(\mathcal{P}_{zu_0}\right)^2|z\rangle\langle z|\right]\\ &= u_0\Gamma(a/b)\sum_{n,m=0}^{\infty}\frac{|n\rangle\langle m|}{\sqrt{{}_p\rho_q(n)}\sqrt{{}_p\rho_q(m)}}\\ &\quad\times\int_0^{\infty}\mathrm{d}(|z|^2)\,G^{q+1,0}_{p,q+1}(|z|^2\mid\cdots)\\ &\quad\times\int_0^{2\pi}\frac{\mathrm{d}\varphi_z}{2\pi}\,z^n(z^*)^m\\ &= \Gamma(a/b)\left[\sum_{n=0}^{\infty}\frac{|n\rangle\langle n|}{{}_p\rho_q(n)}\frac{{}_p\rho_q(n)}{\Gamma(a/b)}\right]u_0\\ &= u_0\sum_{n=0}^{\infty}|n\rangle\langle n|=u_0.\end{aligned}\tag{97}$$

The angular integral satisfies

$$\int_0^{2\pi}\frac{\mathrm{d}\varphi_z}{2\pi}\,z^n(z^*)^m=(|z|^2)^n\delta_{nm}.\tag{98}$$

Thus, the off-diagonal terms vanish upon integration over the phase of z. The remaining radial integral is [23]

$$\begin{aligned}&\int_0^{\infty}\mathrm{d}(|z|^2)\,(|z|^2)^n\\ &\quad\times G^{q+1,0}_{p,q+1}\left(|z|^2\,\middle|\,\begin{matrix}-;\,\{a_i-1\}_{i=1}^{p}\\ 0,\{b_j-1\}_{j=1}^{q};-\end{matrix}\right)\\ &\quad=\frac{{}_p\rho_q(n)}{\Gamma(a/b)}.\end{aligned}\tag{99}$$

Consequently,

$$\begin{aligned}\mathrm{Int}_z &= \Gamma(a/b)\left[\sum_{n=0}^{\infty}\frac{|n\rangle\langle n|}{{}_p\rho_q(n)}\frac{{}_p\rho_q(n)}{\Gamma(a/b)}\right]u_0\\ &= u_0\sum_{n=0}^{\infty}|n\rangle\langle n|=u_0.\end{aligned}\tag{100}$$

Similarly, integration over σ yields $\mathrm{Int}_\sigma=u_1$. Hence,

$$\mathrm{Int}_z+\mathrm{Int}_\sigma=u_0+u_1=I.\tag{101}$$

The integral therefore reproduces the identity operator.

The preceding calculation gives the identity matrix as the sum of the two components. Thus, with the componentwise interpretation of the measure, the coherent states satisfy the resolution of the identity. This is the third condition in Klauder's prescription [19].

The first two conditions concern normalization and continuity. The states are normalized and generally nonorthogonal:

$$\begin{aligned}&\langle zu_0+\sigma u_1\mid z'u_0+\sigma'u_1\rangle\\ &\quad=\langle z|z'\rangle u_0+\langle\sigma|z'\rangle u_1u_0\\ &\qquad+\langle z|\sigma'\rangle u_0u_1+\langle\sigma|\sigma'\rangle u_1\\ &\quad=\langle z|z'\rangle u_0+\langle\sigma|\sigma'\rangle u_1.\end{aligned}\tag{102}$$

For $z'=z$ and $\sigma'=\sigma$, this expression equals $I=u_0+u_1$. For distinct labels, the overlap is generally nonzero, so the states are generally nonorthogonal.

The coherent states depend continuously on the complex labels z and σ. Indeed, using the operator norm for the corresponding maps from $\mathbb{C}^2$ into $\mathbb{C}^2\otimes\mathcal{H}_{\mathrm{Fock}}$, we have

$$\begin{aligned}&\big\|\,|zu_0+\sigma u_1\rangle-|z'u_0+\sigma'u_1\rangle\,\big\|\\ &\quad=\max\left\{\big\||z\rangle-|z'\rangle\big\|,\big\||\sigma\rangle-|\sigma'\rangle\big\|\right\}\longrightarrow 0\\ &\qquad z\longrightarrow z',\quad \sigma\longrightarrow\sigma'.\end{aligned}\tag{103}$$

Finally, the states satisfy the resolution of the identity, as established above:

$$\begin{aligned}&\int\mathrm{d}\mu(zu_0+\sigma u_1)\,|zu_0+\sigma u_1\rangle\langle zu_0+\sigma u_1|\\ &\quad=u_0\left[\int\mathrm{d}\mu(z)\left(\mathcal{P}_{zu_0}\right)^2|z\rangle\langle z|\right]\\ &\qquad+u_1\left[\int\mathrm{d}\mu(\sigma)\left(\mathcal{P}_{\sigma u_1}\right)^2|\sigma\rangle\langle\sigma|\right]\\ &\quad=u_0+u_1=I.\end{aligned}\tag{104}$$

For applications, we consider the expectation values of observables $\mathcal{A}$ characterizing the system. For an observable acting on the Fock-space factor, its matrix-valued coherent-state expectation is

$$\begin{aligned}\langle\mathcal{A}\rangle_{z,\sigma} &\equiv \langle zu_0+\sigma u_1|\mathcal{A}|zu_0+\sigma u_1\rangle \\ &= \left[u_0\,{}_pF_q(|z|^2)+u_1\,{}_pF_q(|\sigma|^2)\right]^{-1} \\ &\quad\times\sum_{n,n'=0}^{\infty}\frac{u_0(z^*)^n z^{n'}+u_1(\sigma^*)^n\sigma^{n'}}{\sqrt{{}_p\rho_q(n)\,{}_p\rho_q(n')}} \\ &\quad\times\langle n|\mathcal{A}|n'\rangle.\end{aligned} \tag{105}$$

If the observable is diagonal in the Fock basis, $\mathcal{A}|n\rangle = A(n)|n\rangle$, and its eigenvalues admit a power-series expansion $A(n)=\sum_{\ell=0}^{\infty}c_\ell n^\ell$, the preceding expression can be simplified further.

$$\begin{aligned}\langle\mathcal{A}\rangle_{z,\sigma} &= \left[u_0\,{}_pF_q(|z|^2)+u_1\,{}_pF_q(|\sigma|^2)\right]^{-1} \\ &\quad\times\sum_{n=0}^{\infty}\frac{u_0(|z|^2)^n+u_1(|\sigma|^2)^n}{{}_p\rho_q(n)}\sum_{\ell=0}^{\infty}c_\ell n^\ell \\ &= \left[u_0\,{}_pF_q(|z|^2)+u_1\,{}_pF_q(|\sigma|^2)\right]^{-1} \\ &\quad\times\sum_{\ell=0}^{\infty}c_\ell\left[u_0\sum_{n=0}^{\infty}\frac{n^\ell(|z|^2)^n}{{}_p\rho_q(n)}+u_1\sum_{n=0}^{\infty}\frac{n^\ell(|\sigma|^2)^n}{{}_p\rho_q(n)}\right] \\ &= \left[u_0\,{}_pF_q(|z|^2)+u_1\,{}_pF_q(|\sigma|^2)\right]^{-1} \\ &\quad\times\left[u_0\sum_{\ell=0}^{\infty}c_\ell\Theta^\ell_{|z|^2}\,{}_pF_q(|z|^2)\right. \\ &\qquad\left.+u_1\sum_{\ell=0}^{\infty}c_\ell\Theta^\ell_{|\sigma|^2}\,{}_pF_q(|\sigma|^2)\right] \\ &= \left[u_0\,{}_pF_q(|z|^2)+u_1\,{}_pF_q(|\sigma|^2)\right]^{-1} \\ &\quad\times\left[u_0A(\Theta_{|z|^2})\,{}_pF_q(|z|^2)\right. \\ &\qquad\left.+u_1A(\Theta_{|\sigma|^2})\,{}_pF_q(|\sigma|^2)\right].\end{aligned} \tag{106}$$

The last equality follows by replacing n with the Euler differential operator, $A(n)\mapsto A(\Theta_x)$, where $\Theta_x = x\,\partial/\partial x$ and $x=|z|^2$ or $x=|\sigma|^2$. The interchange of sums and derivatives is understood where the corresponding series converge.

For a coherent state labelled by a single complex variable, for example z, the expectation value is

$$\begin{aligned}\langle\mathcal{A}\rangle_z &\equiv \langle z|\mathcal{A}|z\rangle \\ &= \frac{1}{{}_pF_q(|z|^2)}\sum_{n=0}^{\infty}\frac{(|z|^2)^n}{{}_p\rho_q(n)}A(n) \\ &= \frac{1}{{}_pF_q(|z|^2)}\sum_{\ell=0}^{\infty}c_\ell\sum_{n=0}^{\infty}\frac{n^\ell(|z|^2)^n}{{}_p\rho_q(n)} \\ &= \frac{1}{{}_pF_q(|z|^2)}\sum_{\ell=0}^{\infty}c_\ell\Theta^\ell_{|z|^2}\,{}_pF_q(|z|^2) \\ &= \frac{A(\Theta_{|z|^2})\,{}_pF_q(|z|^2)}{{}_pF_q(|z|^2)}.\end{aligned} \tag{107}$$

Consequently, the expectation value in the matrix-labelled state decomposes into the expectation values associated with the two individual coherent states:

$$\begin{aligned}\langle\mathcal{A}\rangle_{z,\sigma} &= u_0\big(\mathcal{P}_{zu_0}\big)^2\langle\mathcal{A}\rangle_z+u_1\big(\mathcal{P}_{\sigma u_1}\big)^2\langle\mathcal{A}\rangle_\sigma \\ &= u_0\langle\mathcal{A}\rangle_z+u_1\langle\mathcal{A}\rangle_\sigma.\end{aligned} \tag{108}$$

5 Mixed States

We return to a quantum system in thermodynamic equilibrium with its environment. Its mixed state is described by the canonical density operator

$$\rho=\frac{1}{Z(\beta)}\sum_{n=0}^{\infty}e^{-\beta E_n}|n\rangle\langle n|. \tag{109}$$

In the coherent-state representation, the density operator is associated with quasiprobability distributions, including the Husimi Q-function and the Glauber–Sudarshan P-representation, the latter appearing in its diagonal coherent-state expansion.

The Husimi Q-function is defined through the expectation value of the density operator in the coherent-state representation:

$$\begin{aligned}Q(|zu_0+\sigma u_1|^2) &\equiv \langle zu_0+\sigma u_1|\rho|zu_0+\sigma u_1\rangle \\ &= \frac{1}{Z(\beta)}\sum_{n=0}^{\infty}e^{-\beta E_n}\langle zu_0+\sigma u_1|n\rangle \\ &\qquad\times\langle n|zu_0+\sigma u_1\rangle \\ &= \frac{1}{Z(\beta)}\left[u_0\,{}_pF_q(|z|^2)+u_1\,{}_pF_q(|\sigma|^2)\right]^{-1} \\ &\quad\times\sum_{n=0}^{\infty}e^{-\beta E_n}\frac{|zu_0+\sigma u_1|^{2n}}{{}_p\rho_q(n)} \\ &= \frac{1}{Z(\beta)}\left[u_0\,{}_pF_q(|z|^2)+u_1\,{}_pF_q(|\sigma|^2)\right]^{-1} \\ &\quad\times\sum_{n=0}^{\infty}e^{-\beta E_n}\left[u_0\frac{(|z|^2)^n}{{}_p\rho_q(n)}+u_1\frac{(|\sigma|^2)^n}{{}_p\rho_q(n)}\right].\end{aligned} \tag{110}$$

Finally, we obtain

$$\begin{aligned}Q(|zu_0+\sigma u_1|^2) &= u_0\big(\mathcal{P}_{zu_0}\big)^2Q(|z|^2) \\ &\quad+u_1\big(\mathcal{P}_{\sigma u_1}\big)^2Q(|\sigma|^2).\end{aligned} \tag{111}$$

Thus, the matrix-valued Husimi function decomposes into the Husimi functions associated with the individual variables:

$$Q(|z|^2)=\frac{1}{Z(\beta)\,{}_pF_q(|z|^2)}\sum_{n=0}^{\infty}e^{-\beta E_n}\frac{(|z|^2)^n}{{}_p\rho_q(n)}. \tag{112}$$

An analogous expression holds for σ. This is the usual Husimi function in the coherent-state representation labelled by a single complex variable. The Husimi function is nonnegative.

On the one hand, the density operator has the expansion over Fock-state projectors

$$\rho = \sum_{n=0}^{\infty} \frac{e^{-\beta E_n}}{Z(\beta)} |n\rangle\langle n|. \tag{113}$$

On the other hand, the quasiprobability distribution $P_{p,q}$ appears as a weight in the diagonal coherent-state representation:

$$\begin{aligned}\rho &= \int \mathrm{d}\mu(Z)\, P_{p,q}(|Z|^2)\, |Z\rangle\langle Z| \\ &= \sum_{n=0}^{\infty} \frac{|n\rangle\langle n|}{{}_p\rho_q(n)} \int \mathrm{d}\mu(Z)\, P_{p,q}(|Z|^2) \frac{(|Z|^2)^n}{{}_pF_q(|Z|^2)}.\end{aligned} \tag{114}$$

Equating the coefficients gives the moment condition

$$\int \mathrm{d}\mu(Z)\, P_{p,q}(|Z|^2) \frac{(|Z|^2)^n}{{}_pF_q(|Z|^2)} = \frac{e^{-\beta E_n}}{Z(\beta)} {}_p\rho_q(n). \tag{115}$$

Using the explicit integration measure, this becomes

$$\begin{aligned}&\int \frac{\mathrm{d}^2 Z}{\pi}\, G^{q+1,0}_{p,q+1}(|Z|^2 \mid \cdots) P_{p,q}(|Z|^2)(|Z|^2)^n \\ &\quad = \frac{e^{-\beta E_n}\, {}_p\rho_q(n)}{\Gamma(a/b)\, Z(\beta)}.\end{aligned} \tag{116}$$

Returning to the variables z and σ, we write

$$\begin{aligned}\rho = \int \mathrm{d}\mu(zu_0 + \sigma u_1)\, P_{p,q}\big(|z|^2 u_0 + |\sigma|^2 u_1\big) \\ \times |zu_0 + \sigma u_1\rangle\langle zu_0 + \sigma u_1|.\end{aligned} \tag{117}$$

This expression must agree with the expansion of the density operator in terms of the Fock-state projectors $|n\rangle\langle n|$.

$$\begin{aligned}&\frac{1}{Z(\beta)} \sum_{n=0}^{\infty} e^{-\beta E_n} |n\rangle\langle n| \\ &\quad = \int \mathrm{d}\mu(zu_0 + \sigma u_1)\, P_{p,q}\big(|z|^2 u_0 + |\sigma|^2 u_1\big) \\ &\qquad \times |zu_0 + \sigma u_1\rangle\langle zu_0 + \sigma u_1|.\end{aligned} \tag{118}$$

Writing the coherent-state projector in the following form,

$$\begin{aligned}&|zu_0 + \sigma u_1\rangle\langle zu_0 + \sigma u_1| \\ &\quad = \big[{}_pF_q\big(|zu_0 + \sigma u_1|^2\big)\big]^{-1} \\ &\qquad \times \sum_{n=0}^{\infty} \frac{\big(|z|^2 u_0 + |\sigma|^2 u_1\big)^n}{{}_p\rho_q(n)} |n\rangle\langle n|,\end{aligned} \tag{119}$$

we obtain

$$\begin{aligned}&\left[\frac{1}{Z(\beta)} \sum_{n=0}^{\infty} e^{-\beta E_n}\right] |n\rangle\langle n| \\ &\quad = \left[\int \mathrm{d}\mu(zu_0 + \sigma u_1)\right. \\ &\qquad \times \frac{P_{p,q}\big(|z|^2 u_0 + |\sigma|^2 u_1\big)}{{}_pF_q(|zu_0 + \sigma u_1|^2)} \\ &\qquad \left. \times \frac{\big(|z|^2 u_0 + |\sigma|^2 u_1\big)^n}{{}_p\rho_q(n)}\right] |n\rangle\langle n|.\end{aligned} \tag{120}$$

Equality of the corresponding coefficients requires

$$\begin{aligned}&\int \mathrm{d}\mu(zu_0 + \sigma u_1) \\ &\quad \times \frac{P_{p,q}\big(|z|^2 u_0 + |\sigma|^2 u_1\big)}{{}_pF_q(|zu_0 + \sigma u_1|^2)} \big(|z|^2 u_0 + |\sigma|^2 u_1\big)^n \\ &\qquad = \frac{e^{-\beta E_n}}{Z(\beta)} {}_p\rho_q(n).\end{aligned} \tag{121}$$

Substituting the expressions for the integration measure and the coherent states gives

$$\begin{aligned}\rho = \Gamma(a/b) \int &\left[\frac{\mathrm{d}\varphi_z}{2\pi} \mathrm{d}(|z|^2) u_0 + \frac{\mathrm{d}\varphi_\sigma}{2\pi} \mathrm{d}(|\sigma|^2) u_1\right] \\ &\times \big[u_0\, {}_pF_q(|z|^2) + u_1\, {}_pF_q(|\sigma|^2)\big] \\ &\times P_{p,q}\big(|z|^2 u_0 + |\sigma|^2 u_1\big) \\ &\times \Big[u_0 G^{q+1,0}_{p,q+1}(|z|^2 \mid \cdots) \\ &\qquad + u_1 G^{q+1,0}_{p,q+1}(|\sigma|^2 \mid \cdots)\Big] \\ &\times \Big[u_0 \big(\mathcal{P}_{zu_0}\big)^2 |z\rangle\langle z| \\ &\qquad + u_1 \big(\mathcal{P}_{\sigma u_1}\big)^2 |\sigma\rangle\langle\sigma|\Big].\end{aligned} \tag{122}$$

The properties of the projectors also allow the function $P_{p,q}$ to be decomposed into two functions, each depending on a single variable:

$$\begin{aligned}&P_{p,q}\big(|z|^2 u_0 + |\sigma|^2 u_1\big) \\ &\quad = u_0 P_{p,q}(|z|^2) + u_1 P_{p,q}(|\sigma|^2).\end{aligned} \tag{123}$$

Multiplying the factors and using $u_i u_j = 0$ for $i \neq j$, we obtain

$$\begin{aligned}\rho = u_0 \Gamma(a/b) &\int_0^{\infty} \mathrm{d}(|z|^2)\, {}_pF_q(|z|^2) P_{p,q}(|z|^2) \\ &\times G^{q+1,0}_{p,q+1}\left(|z|^2 \,\middle|\, \begin{matrix} -;\, \{a_i - 1\}_{i=1}^p \\ 0, \{b_j - 1\}_{j=1}^q;\, - \end{matrix}\right) |z\rangle\langle z| \\ &+ u_1 \Gamma(a/b) \int_0^{\infty} \mathrm{d}(|\sigma|^2)\, {}_pF_q(|\sigma|^2) P_{p,q}(|\sigma|^2) \\ &\times G^{q+1,0}_{p,q+1}\left(|\sigma|^2 \,\middle|\, \begin{matrix} -;\, \{a_i - 1\}_{i=1}^p \\ 0, \{b_j - 1\}_{j=1}^q;\, - \end{matrix}\right) |\sigma\rangle\langle\sigma|.\end{aligned} \tag{124}$$

The density operator is therefore expressed as the sum of two components.

$$\rho = u_0\rho_z + u_1\rho_\sigma. \tag{125}$$

The variables z and σ enter symmetrically, so the corresponding expressions have the same form. We therefore evaluate the component associated with z:

$$\begin{aligned}\rho_z = \Gamma(a/b)\int_0^\infty \mathrm{d}(|z|^2)\,{}_pF_q(|z|^2)P_{p,q}(|z|^2)\\ \times G^{q+1,0}_{p,q+1}(|z|^2\mid\cdots)\int_0^{2\pi}\frac{\mathrm{d}\varphi_z}{2\pi}\,|z\rangle\langle z|.\end{aligned} \tag{126}$$

After angular integration, this gives

$$\begin{aligned}\rho_z = \Gamma(a/b)\sum_{n=0}^\infty \frac{|n\rangle\langle n|}{{}_p\rho_q(n)}\int_0^\infty \mathrm{d}(|z|^2)\,P_{p,q}(|z|^2)\\ \times G^{q+1,0}_{p,q+1}(|z|^2\mid\cdots)(|z|^2)^n.\end{aligned} \tag{127}$$

As in Eq. (121), comparison with the canonical density operator yields

$$\begin{aligned}\int_0^\infty \mathrm{d}(|z|^2)\,P_{p,q}(|z|^2)G^{q+1,0}_{p,q+1}(|z|^2\mid\cdots)(|z|^2)^n\\ = \frac{e^{-\beta E_n}\,{}_p\rho_q(n)}{\Gamma(a/b)\,Z(\beta)}.\end{aligned} \tag{128}$$

This is a Stieltjes moment problem [20] for the unknown function $P_{p,q}(|z|^2)G^{q+1,0}_{p,q+1}(|z|^2\mid\cdots)$. The structure function ${}_p\rho_q(n)$ is expressed in terms of Euler gamma functions; see Eq. (36).

Solving the moment problem requires specifying the dependence of the energy eigenvalues on the quantum number, $E_n = f(n)$. Nonlinear spectra generally require additional techniques. For quadratic spectra, such as that of the Morse oscillator, specific procedures are available [21].

Consider a system with a linear energy spectrum, $E_n = \hbar\omega n + E_0$. In this case,

$$\begin{aligned}Z(\beta) &= \sum_{n=0}^\infty e^{-\beta E_n}\\ &= e^{-\beta E_0}\sum_{n=0}^\infty \left(e^{-\beta\hbar\omega}\right)^n\\ &= \frac{e^{-\beta E_0}}{1-e^{-\beta\hbar\omega}},\\ \frac{e^{-\beta E_n}}{Z(\beta)} &= \left(1-e^{-\beta\hbar\omega}\right)\left(e^{-\beta\hbar\omega}\right)^n.\end{aligned} \tag{129}$$

The moment equation therefore becomes

$$\begin{aligned}\int_0^\infty \mathrm{d}(|z|^2)\,P_{p,q}(|z|^2)G^{q+1,0}_{p,q+1}(|z|^2\mid\cdots)(|z|^2)^n\\ = \left(1-e^{-\beta\hbar\omega}\right)\left(e^{-\beta\hbar\omega}\right)^n\\ \times\Gamma(n+1)\frac{\prod_{j=1}^q\Gamma(b_j+n)}{\prod_{i=1}^p\Gamma(a_i+n)}.\end{aligned} \tag{130}$$

Setting $n = s-1$ gives the Mellin-transform expression. The corresponding solution can then be sought through the inverse Mellin transform [22]:

$$\begin{aligned}\int_0^\infty \mathrm{d}(|z|^2)\,P_{p,q}(|z|^2)G^{q+1,0}_{p,q+1}(|z|^2\mid\cdots)(|z|^2)^{s-1}\\ = \frac{e^{\beta\hbar\omega}-1}{(e^{\beta\hbar\omega})^s}\Gamma(s)\frac{\prod_{j=1}^q\Gamma(b_j-1+s)}{\prod_{i=1}^p\Gamma(a_i-1+s)}.\end{aligned} \tag{131}$$

The resulting P-quasiprobability distribution for a system with a linear energy spectrum is [23]

$$\begin{aligned}P_{p,q}(|z|^2) &= \left(e^{\beta\hbar\omega}-1\right)\\ &\times\frac{G^{q+1,0}_{p,q+1}\left(e^{\beta\hbar\omega}|z|^2\,\middle|\,\begin{matrix}-;\{a_i-1\}_{i=1}^p\\ 0,\{b_j-1\}_{j=1}^q;-\end{matrix}\right)}{G^{q+1,0}_{p,q+1}\left(|z|^2\,\middle|\,\begin{matrix}-;\{a_i-1\}_{i=1}^p\\ 0,\{b_j-1\}_{j=1}^q;-\end{matrix}\right)}\\ &\equiv\left(e^{\beta\hbar\omega}-1\right)\frac{G^{q+1,0}_{p,q+1}\left(e^{\beta\hbar\omega}|z|^2\mid\cdots\right)}{G^{q+1,0}_{p,q+1}(|z|^2\mid\cdots)}.\end{aligned} \tag{132}$$

An analogous expression is obtained for the variable σ.

The thermal expectation value of an observable $\mathcal{A}$ in the mixed state described by ρ is

$$\langle\mathcal{A}\rangle = \mathrm{Tr}(\rho\mathcal{A})u_0\,\mathrm{Tr}(\rho_z\mathcal{A}) + u_1\,\mathrm{Tr}(\rho_\sigma\mathcal{A}). \tag{133}$$

We now apply these results to the one-dimensional harmonic oscillator restricted to its first two energy levels:

$$\begin{aligned}E_n &= \hbar\omega\,e(n) = \hbar\omega\left(n+\frac{1}{2}\right),\\ E_0 &= \frac{1}{2}\hbar\omega,\qquad E_1 = \frac{3}{2}\hbar\omega.\end{aligned} \tag{134}$$

The dimensionless energy expression can be represented, for the structure-function construction, by

$$\begin{aligned}e(n) &= n\frac{\prod_{j=1}^q(b_j-1+n)}{\prod_{i=1}^p(a_i-1+n)},\\ p&=1,\qquad q=1,\qquad a_1=1,\qquad b_1=\frac{3}{2}.\end{aligned} \tag{135}$$

The corresponding structure function is

$$
\begin{aligned}
{}_p\rho_q(n) &= \Gamma(a/b)\,\Gamma(n+1)\frac{\prod_{j=1}^{q}\Gamma(b_j+n)}{\prod_{i=1}^{p}\Gamma(a_i+n)},\\
{}_1\rho_1(n) &= \frac{2}{\sqrt{\pi}}\,\Gamma\!\left(\frac{3}{2}+n\right),\\
{}_1\rho_1(0) &= 1, \qquad {}_1\rho_1(1) = \frac{3}{2}.
\end{aligned}
\tag{136}
$$

Starting from the coherent-state expansion in the variable Z, we write

$$
\begin{aligned}
|Z\rangle &= \frac{1}{\sqrt{{}_1F_1(|Z|^2)}}\sum_{n=0}^{1}\frac{Z^n}{\sqrt{{}_1\rho_1(n)}}|n\rangle,\\
{}_1F_1(|Z|^2) &\longrightarrow \sum_{n=0}^{1}\frac{(1)_n}{\left(\frac{3}{2}\right)_n}\frac{(|Z|^2)^n}{n!}\\
&= 1+\frac{2}{3}|Z|^2 \equiv \mathcal{N}_2(|Z|^2).
\end{aligned}
\tag{137}
$$

Here, the normalization is the first-degree polynomial $\mathcal{N}_2(|Z|^2)$ obtained by truncating the hypergeometric series. It is not the full confluent hypergeometric function.

The normalized two-level state is therefore

$$
\begin{aligned}
|Z\rangle &= \frac{1}{\sqrt{\mathcal{N}_2(|Z|^2)}}|0\rangle + \frac{Z}{\sqrt{{}_1\rho_1(1)}\sqrt{\mathcal{N}_2(|Z|^2)}}|1\rangle\\
&= \frac{1}{\sqrt{1+\frac{2}{3}|Z|^2}}\begin{pmatrix}1\\0\end{pmatrix} + \frac{\sqrt{\frac{2}{3}}\,Z}{\sqrt{1+\frac{2}{3}|Z|^2}}\begin{pmatrix}0\\1\end{pmatrix}.
\end{aligned}
\tag{138}
$$

The diagonal part of the coherent-state projector is

$$
\begin{aligned}
\int_0^{2\pi}\frac{\mathrm{d}\varphi_Z}{2\pi}\,|Z\rangle\langle Z| &= \frac{1}{1+\frac{2}{3}|Z|^2}u_0\\
&\quad + \frac{\frac{2}{3}|Z|^2}{1+\frac{2}{3}|Z|^2}u_1.
\end{aligned}
\tag{139}
$$

The density operator and the partition function for the thermal state of this two-level system are

$$
\begin{aligned}
\rho &= \sum_{n=0}^{1}\frac{e^{-\beta\hbar\omega(n+\frac{1}{2})}}{Z(\beta)}|n\rangle\langle n|\\
&= \frac{e^{-\frac{1}{2}\beta\hbar\omega}}{Z(\beta)}u_0 + \frac{e^{-\frac{3}{2}\beta\hbar\omega}}{Z(\beta)}u_1,\\
Z(\beta) &= e^{-\beta E_0}+e^{-\beta E_1}\\
&= e^{-\frac{1}{2}\beta\hbar\omega}+e^{-\frac{3}{2}\beta\hbar\omega}.
\end{aligned}
\tag{140}
$$

We now examine the integral representation of the density operator for this truncated system:

$$
\begin{aligned}
\rho &= \int \mathrm{d}\mu(Z)\,P_{1,1}(|Z|^2)|Z\rangle\langle Z|\\
&= \frac{1}{Z(\beta)}\sum_{n=0}^{1}e^{-\beta\hbar\omega(n+\frac{1}{2})}u_n.
\end{aligned}
\tag{141}
$$

Applying the formal expression in Eq. (132) gives

$$
\begin{aligned}
P_{1,1}(|Z|^2) &= \left(e^{\beta\hbar\omega}-1\right)\\
&\quad\times\frac{G_{1,2}^{2,0}\left(e^{\beta\hbar\omega}|Z|^2\,\middle|\,\begin{matrix}-;\,0\\0,\frac{1}{2};\,-\end{matrix}\right)}{G_{1,2}^{2,0}\left(|Z|^2\,\middle|\,\begin{matrix}-;\,0\\0,\frac{1}{2};\,-\end{matrix}\right)}\\
&= \left(e^{\beta\hbar\omega}-1\right)\frac{G_{0,1}^{1,0}\left(e^{\beta\hbar\omega}|Z|^2\,\middle|\,\frac{1}{2}\right)}{G_{0,1}^{1,0}\left(|Z|^2\,\middle|\,\frac{1}{2}\right)}\\
&= \left(e^{\beta\hbar\omega}-1\right)e^{\frac{1}{2}\beta\hbar\omega}e^{-(e^{\beta\hbar\omega}-1)|Z|^2}\\
&= \left(e^{\frac{3}{2}\beta\hbar\omega}-e^{\frac{1}{2}\beta\hbar\omega}\right)e^{-(e^{\beta\hbar\omega}-1)|Z|^2}.
\end{aligned}
\tag{142}
$$

Here, we used the index-reduction property of Meijer's G-function. According to Eq. (85), the measure is

$$
\begin{aligned}
\mathrm{d}\mu(Z) &= \frac{2}{\sqrt{\pi}}\frac{\mathrm{d}^2Z}{\pi}G_{0,1}^{1,0}\left(|Z|^2\,\middle|\,\frac{1}{2}\right){}_1F_1(|Z|^2)\\
&= \frac{2}{\sqrt{\pi}}\frac{\mathrm{d}^2Z}{\pi}e^{-|Z|^2}|Z|\,{}_1F_1(|Z|^2).
\end{aligned}
\tag{143}
$$

After angular integration, substitution of the coherent-state projector gives the coefficient comparison

$$
\begin{aligned}
\rho &= \sum_{n=0}^{1}\frac{u_n}{{}_1\rho_1(n)}\int \mathrm{d}\mu(Z)\,P_{1,1}(|Z|^2)\frac{(|Z|^2)^n}{\mathcal{N}_2(|Z|^2)}\\
&= \frac{1}{Z(\beta)}\sum_{n=0}^{1}e^{-\beta\hbar\omega(n+\frac{1}{2})}u_n.
\end{aligned}
\tag{144}
$$

The corresponding moment conditions are

$$
\begin{aligned}
&\int \mathrm{d}\mu(Z)\,P_{1,1}(|Z|^2)\frac{(|Z|^2)^n}{\mathcal{N}_2(|Z|^2)}\\
&\quad= \frac{e^{-\beta\hbar\omega(n+\frac{1}{2})}}{Z(\beta)}{}_1\rho_1(n)\\
&\quad= \frac{2}{\sqrt{\pi}}\frac{e^{-\frac{1}{2}\beta\hbar\omega}}{Z(\beta)}\frac{\Gamma\left(\frac{3}{2}+n\right)}{\left(e^{\beta\hbar\omega}\right)^n}, \qquad n=0,1.
\end{aligned}
\tag{145}
$$

Substituting this result into the density-operator expression gives

$$\begin{aligned}\rho &= \frac{2}{\sqrt{\pi}}\,\frac{e^{-\frac{1}{2}\beta\hbar\omega}}{Z(\beta)}\sum_{n=0}^{1}\frac{|n\rangle\langle n|}{{}_1\rho_1(n)}\\ &\quad\times\left(e^{-\beta\hbar\omega}\right)^n\Gamma\left(\frac{3}{2}+n\right)\\ &= \frac{2}{\sqrt{\pi}}\,\frac{e^{-\frac{1}{2}\beta\hbar\omega}}{Z(\beta)}\left[\Gamma\left(\frac{3}{2}\right)u_0+\frac{2}{3}e^{-\beta\hbar\omega}\Gamma\left(\frac{5}{2}\right)u_1\right]\\ &= \frac{1}{1+e^{-\beta\hbar\omega}}u_0+\frac{1}{1+e^{\beta\hbar\omega}}u_1\\ &= \frac{1}{2+e^{\beta\hbar\omega}+e^{-\beta\hbar\omega}}\begin{pmatrix}1+e^{\beta\hbar\omega} & 0\\ 0 & 1+e^{-\beta\hbar\omega}\end{pmatrix}.\end{aligned} \tag{146}$$

The trace of this density operator is $\operatorname{Tr}\rho = 1$, as required.

This calculation compares two representations of the density operator: its expansion over the orthogonal Fock-state projectors and its integral representation in terms of coherent-state projectors.

From another perspective, the density operator of a two-level system, here obtained by retaining two energy levels of a harmonic oscillator, can describe a qubit in thermal equilibrium with its environment at $T = (\beta k_{\mathrm{B}})^{-1}$. Such a system may be referred to as a thermal qubit.

6 Some Applications

Coherent states provide a connection between classical and quantum mechanics and help describe the classical limit of quantum systems, following Schrödinger's original motivation in 1926. Their applications include quantum optics, condensed-matter physics, chemistry, radar theory, and mathematical physics. They are also connected to quantum information and quantum computing through their relation to qubits [24–26].

Because coherent states can represent logical qubits in quantum computing [27], we examine how the coherent states with matrix arguments considered here relate to qubit states.

As shown previously, a coherent state with a complex label Z has the expansion

$$|Z\rangle = \frac{1}{\sqrt{{}_pF_q(|Z|^2)}}\sum_{n=0}^{n_{\max}}\frac{Z^n}{\sqrt{{}_p\rho_q(n)}}|n\rangle. \tag{147}$$

For a two-level system, obtained by retaining only the first two terms of the series and renormalizing, this becomes

$$\begin{aligned}|Z\rangle &= \frac{1}{\sqrt{\mathcal{N}_2(|Z|^2)}}\sum_{n=0}^{1}\frac{Z^n}{\sqrt{{}_p\rho_q(n)}}|n\rangle\\ &= \frac{1}{\sqrt{1+\frac{|Z|^2}{{}_p\rho_q(1)}}}|0\rangle+\frac{Z/\sqrt{{}_p\rho_q(1)}}{\sqrt{1+\frac{|Z|^2}{{}_p\rho_q(1)}}}|1\rangle,\end{aligned} \tag{148}$$

where $\mathcal{N}_2(|Z|^2) = 1+|Z|^2/{}_p\rho_q(1)$. where the two-level normalization is $\mathcal{N}_2(|Z|^2) = 1+|Z|^2/{}_p\rho_q(1)$, with

$${}_p\rho_q(1) = \frac{\prod_{j=1}^{q} b_j}{\prod_{i=1}^{p} a_i}. \tag{149}$$

The squared moduli of the coefficients of the ground state $|0\rangle$ and the excited state $|1\rangle$ sum to unity. Thus, the normalized two-level state has the form of a qubit.

Returning to matrix notation, we write

$$Z = zu_0+\sigma u_1 = \begin{pmatrix}z & 0\\ 0 & \sigma\end{pmatrix}. \tag{150}$$

The corresponding matrix-labelled state is

$$\begin{aligned}&\left|\begin{pmatrix}z & 0\\ 0 & \sigma\end{pmatrix}\right\rangle\\ &\quad=\left[I+\frac{1}{{}_p\rho_q(1)}\begin{pmatrix}|z|^2 & 0\\ 0 & |\sigma|^2\end{pmatrix}\right]^{-1/2}|0\rangle\\ &\qquad+\frac{1}{\sqrt{{}_p\rho_q(1)}}\begin{pmatrix}z & 0\\ 0 & \sigma\end{pmatrix}\\ &\qquad\times\left[I+\frac{1}{{}_p\rho_q(1)}\begin{pmatrix}|z|^2 & 0\\ 0 & |\sigma|^2\end{pmatrix}\right]^{-1/2}|1\rangle.\end{aligned} \tag{151}$$

This construction provides a matrix-labelled family of two-level states. Different physical implementations of qubits include photonic, thermal, superconducting, and spin systems. In the present mathematical setting, the matrix argument depends on two complex parameters.

The continuous range of these parameters produces infinitely many states. This does not, by itself, imply an infinite capacity for storing or retrieving classical information.

Another important concept in quantum information and quantum computing is the von Neumann entropy [28]. For a mixed state described by a density operator ρ, it is defined by

$$S = -\operatorname{Tr}(\rho\log\rho). \tag{152}$$

We now evaluate this expression when the density operator is a 2×2 diagonal matrix:

$$\begin{aligned}\rho &= \sum_{n=0}^{1} \frac{e^{-\beta E_n}}{Z(\beta)} |n\rangle\langle n| = \begin{pmatrix} \dfrac{e^{-\beta E_0}}{Z(\beta)} & 0 \\ 0 & \dfrac{e^{-\beta E_1}}{Z(\beta)} \end{pmatrix} \\ &= \begin{pmatrix} w_0 & 0 \\ 0 & w_1 \end{pmatrix} = w_0 u_0 + w_1 u_1, \\ w_n &= \frac{e^{-\beta E_n}}{Z(\beta)}, \qquad n = 0, 1, \\ Z(\beta) &= \sum_{n=0}^{1} e^{-\beta E_n} = e^{-\beta E_0} + e^{-\beta E_1}.\end{aligned} \tag{153}$$

Recall the trace formula for a product of operators:

$$\begin{aligned}\mathrm{Tr}(AB) &= \sum_n \langle n|AB|n\rangle \\ &= \sum_n \sum_m \langle n|A|m\rangle\langle m|B|n\rangle.\end{aligned} \tag{154}$$

For the diagonal density operator, $\langle n|f(\rho)|m\rangle = f(w_n)\delta_{nm}$. Using these relations, we obtain the entropy expression below.

$$\mathrm{Tr}(\rho \log \rho) = \sum_{n=0}^{1} \sum_{m=0}^{1} \langle n|\rho|m\rangle\langle m| \log \rho|n\rangle. \tag{155}$$

If $\|\rho - I\| < 1$, the logarithm can be computed using its power-series expansion; see, for example, Gradshteyn and Ryzhik [29]:

$$\log \rho = \log[I + (\rho - I)] = -\sum_{k=1}^{\infty} \frac{(-1)^k}{k} (\rho - I)^k. \tag{156}$$

Since ρ is diagonal in the Fock basis, its diagonal matrix elements satisfy

$$\begin{aligned}\langle n| \log \rho|n\rangle &= \langle n| \log[I + (\rho - I)] \, |n\rangle \\ &= -\sum_{k=1}^{\infty} \frac{(-1)^k}{k} \langle n|(\rho - I)^k|n\rangle \\ &= -\sum_{k=1}^{\infty} \frac{(-1)^k}{k} (w_n - 1)^k \\ &= \log w_n.\end{aligned} \tag{157}$$

The von Neumann entropy therefore becomes

$$\begin{aligned}S &= -\,\mathrm{Tr}(\rho \log \rho) \\ &= -\sum_{n=0}^{1} w_n \langle n| \log \rho|n\rangle \\ &= \sum_{n=0}^{1} w_n \sum_{k=1}^{\infty} \frac{(-1)^k}{k} (w_n - 1)^k \\ &= -\left(w_0 \log w_0 + w_1 \log w_1\right).\end{aligned} \tag{158}$$

Thus, the entropy of a mixed state of a two-level system is

$$S = -\left(w_0 \log w_0 + w_1 \log w_1\right). \tag{159}$$

Since $0 \le w_0, w_1 \le 1$ and $w_0 + w_1 = 1$, the entropy is nonnegative, with the convention $0 \log 0 = 0$. This expression coincides with the Shannon entropy of the eigenvalue distribution.

The same result follows directly from matrix calculus and the cyclic property of the trace, $\mathrm{Tr}(AB) = \mathrm{Tr}(BA)$; see the Appendix.

7 Concluding Remarks

The coherent states examined in this paper are labelled by a linear combination of two singular diagonal projectors with complex coefficients. This construction is related to coherent states with shifted arguments [13], while using the algebraic properties of the projectors.

The main simplification follows from the complementary projector relations $u_0 + u_1 = I$ and $u_0 u_1 = u_1 u_0 = 0$. For functions defined on the corresponding spectra, these relations give

$$\mathcal{F}(x u_0 + y u_1) = \mathcal{F}(x) u_0 + \mathcal{F}(y) u_1. \tag{160}$$

Moreover, expressions involving the complex variables z and σ can be written as

$$\mathcal{F}(z, \sigma) = u_0 \mathcal{P}_{z u_0} \mathcal{F}(z) + u_1 \mathcal{P}_{\sigma u_1} \mathcal{F}(\sigma). \tag{161}$$

Expressions involving their squared moduli take the form

$$\begin{aligned}\mathcal{F}(|z|^2, |\sigma|^2) = u_0 \big(\mathcal{P}_{z u_0}\big)^2 \mathcal{F}(|z|^2) \\ + u_1 \big(\mathcal{P}_{\sigma u_1}\big)^2 \mathcal{F}(|\sigma|^2).\end{aligned} \tag{162}$$

These expressions separate the contributions associated with the two complex variables. With the matrix normalization used here, the factors satisfy $\mathcal{P}_{z u_0} = u_0$ and $\mathcal{P}_{\sigma u_1} = u_1$, so the decomposition reduces to the two complementary projector components.

This structure allows the contributions of the two complex labels to be treated separately, unlike a shifted scalar argument that combines them into a single complex number. We considered the construction for pure states and examined its extension to thermal states described by a density operator. As applications, we discussed its relation to two-level states and the von Neumann entropy.

For a two-level system in thermal equilibrium with its environment, the density operator depends on the equilibrium temperature. The corresponding normalized two-level state provides a connection with the description of a thermal qubit.

The matrix-labelling construction gives a two-level scalar parametrization, but its interpretation as a physical qubit requires a specified encoding. Any physical implementation must also address isolation from the environment, resistance to noise and decoherence, controllability, and measurement.

Although the present construction uses two complex variables, the projector-based procedure can be extended to a finite number N of complex variables by replacing the 2×2 diagonal matrices with $N \times N$ diagonal matrices.

Appendix A: Von Neumann Entropy in Matrix Form

We derive the von Neumann entropy formula using matrix notation.

$$
\begin{aligned}
S &= -\operatorname{Tr}(\rho \log \rho) \\
&= -\sum_{n=0}^{1} \langle n|\rho \log \rho|n\rangle \\
&= -\sum_{n,m=0}^{1} \langle n|\rho|m\rangle\langle m|\log \rho|n\rangle \\
&= -\sum_{n=0}^{1} \left\langle n \left| \begin{pmatrix} w_0 & 0 \\ 0 & w_1 \end{pmatrix} \right| n \right\rangle \\
&\quad \times \left\langle n \left| \log \begin{pmatrix} w_0 & 0 \\ 0 & w_1 \end{pmatrix} \right| n \right\rangle \\
&= -\sum_{n=0}^{1} \left\langle n \left| \begin{pmatrix} w_0 & 0 \\ 0 & w_1 \end{pmatrix} \right| n \right\rangle \\
&\quad \times \sum_{k=1}^{\infty} \frac{(-1)^{k+1}}{k} \left\langle n \left| \left[\begin{pmatrix} w_0 & 0 \\ 0 & w_1 \end{pmatrix} - I \right]^k \right| n \right\rangle .
\end{aligned}
\tag{A.1}
$$

The diagonal matrix elements are obtained from

$$
\begin{aligned}
\langle 0|\rho|0\rangle &= \begin{pmatrix} 1 & 0 \end{pmatrix} \begin{pmatrix} w_0 & 0 \\ 0 & w_1 \end{pmatrix} \begin{pmatrix} 1 \\ 0 \end{pmatrix} = w_0, \\
\langle 1|\rho|1\rangle &= \begin{pmatrix} 0 & 1 \end{pmatrix} \begin{pmatrix} w_0 & 0 \\ 0 & w_1 \end{pmatrix} \begin{pmatrix} 0 \\ 1 \end{pmatrix} = w_1.
\end{aligned}
\tag{A.2}
$$

Moreover,

$$
\begin{aligned}
(\rho - I)^k &= \left[\begin{pmatrix} w_0 & 0 \\ 0 & w_1 \end{pmatrix} - I \right]^k \\
&= \begin{pmatrix} w_0 - 1 & 0 \\ 0 & w_1 - 1 \end{pmatrix}^k \\
&= \begin{pmatrix} (w_0 - 1)^k & 0 \\ 0 & (w_1 - 1)^k \end{pmatrix} .
\end{aligned}
\tag{A.3}
$$

Consequently,

$$
\begin{aligned}
&\langle 0|(\rho - I)^k|0\rangle \\
&\quad = \begin{pmatrix} 1 & 0 \end{pmatrix} \begin{pmatrix} (w_0 - 1)^k & 0 \\ 0 & (w_1 - 1)^k \end{pmatrix} \begin{pmatrix} 1 \\ 0 \end{pmatrix} \\
&\quad = (w_0 - 1)^k, \\
&\langle 1|(\rho - I)^k|1\rangle \\
&\quad = \begin{pmatrix} 0 & 1 \end{pmatrix} \begin{pmatrix} (w_0 - 1)^k & 0 \\ 0 & (w_1 - 1)^k \end{pmatrix} \begin{pmatrix} 0 \\ 1 \end{pmatrix} \\
&\quad = (w_1 - 1)^k .
\end{aligned}
\tag{A.4}
$$

For $0 < w_0, w_1 < 1$, the logarithmic series converge. The entropy therefore becomes

$$
\begin{aligned}
S &= -\langle 0|\rho|0\rangle \sum_{k=1}^{\infty} \frac{(-1)^{k+1}}{k} \langle 0|(\rho - I)^k|0\rangle \\
&\quad - \langle 1|\rho|1\rangle \sum_{k=1}^{\infty} \frac{(-1)^{k+1}}{k} \langle 1|(\rho - I)^k|1\rangle \\
&= -w_0 \sum_{k=1}^{\infty} \frac{(-1)^{k+1}}{k} (w_0 - 1)^k \\
&\quad - w_1 \sum_{k=1}^{\infty} \frac{(-1)^{k+1}}{k} (w_1 - 1)^k \\
&= -\left(w_0 \log w_0 + w_1 \log w_1 \right) .
\end{aligned}
\tag{A.5}
$$

The result extends continuously to zero eigenvalues using the convention $0 \log 0 = 0$. □

Acknowledgement

The author is deeply grateful to the (anonymous) reviewers for their pertinent observations on the manuscript and is convinced that they will help improving the quality of the paper.

References

1. E. Schrödinger, "Der stetige Übergang von der Mikro- zur Makromechanik," Naturwissenschaften **14**(28), 664–666 (1926). doi:10.1007/BF01507634.
2. R. J. Glauber, "Coherent and Incoherent States of the Radiation Field," Physical Review **131**(6), 2766–2788 (1963). doi:10.1103/PhysRev.131.2766.
3. J. R. Klauder and B.-S. Skagerstam, *Coherent States: Applications in Physics and Mathematical Physics* (World Scientific, Singapore, 1985). ISBN: 978-9971-966-52-2. doi:10.1142/0096.
4. A. Perelomov, *Generalized Coherent States and Their Applications* (Springer, Berlin, Heidelberg, 1986). ISBN: 978-3-540-15912-4. doi:10.1007/978-3-642-61629-7.

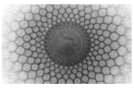
5. J.-P. Gazeau, *Coherent States in Quantum Physics* (Wiley-VCH, Berlin, 2009). ISBN: 978-3-527-40709-5. doi:10.1002/9783527628285.
6. V. V. Dodonov, "'Nonclassical' states in quantum optics: a 'squeezed' review of the first 75 years," Journal of Optics B: Quantum and Semiclassical Optics **4**(1), R1–R33 (2002). doi:10.1088/1464-4266/4/1/201.
7. S. Bera, S. Das, and A. Banerjee, "Bicomplex generalized hypergeometric functions and their applications," Journal of Mathematical Analysis and Applications **550**(1), 129490 (2025). doi:10.1016/j.jmaa.2025.129490.
8. S. Bera, S. Das, and A. Banerjee, "On the Bessel function and n-dimensional Hankel transform with Bicomplex arguments and coherent states," arXiv:2507.16973 [math.CV] (2025). doi:10.48550/arXiv.2507.16973.
9. K. Thirulogasanthar and A. L. Hohouéto, "Vector coherent states with matrix moment problems," Journal of Physics A: Mathematical and General **37**(40), 9531–9548 (2004). doi:10.1088/0305-4470/37/40/014.
10. K. Thirulogasanthar, G. Honnouvo, and A. Krzyżak, "Multi-matrix vector coherent states," Annals of Physics **314**(1), 119–144 (2004). doi:10.1016/j.aop.2004.07.006.
11. A. Dehghani, "General displaced SU(1,1) number states: Revisited," Journal of Mathematical Physics **55**, 043502 (2014). doi:10.1063/1.4868618.
12. J.-P. Gazeau and M. A. del Olmo, "SU(1,1)-displaced coherent states, photon counting, and squeezing," Journal of the Optical Society of America B **40**(5), 1083–1091 (2023). doi:10.1364/JOSAB.484284.
13. D. Popov, "Generalized coherent states with shifted (displaced) arguments," *Transactions in Theoretical and Mathematical Physics* **3**(3), 133–155 (2026). arXiv:2511.10285 [quant-ph] (2025). DOI: 10.30511/ttmp.2026.2095670.1087.
14. G. Hamel, "Eine Basis aller Zahlen und die unstetigen Lösungen der Funktionalgleichung: $f(x+y) = f(x) + f(y)$," Mathematische Annalen **60**(3), 459–462 (1905). doi:10.1007/BF01457624.
15. M. Kuczma, *An Introduction to the Theory of Functional Equations and Inequalities: Cauchy's Equation and Jensen's Inequality*, 2nd ed., edited by A. Gilányi (Birkhäuser, Basel, 2009). ISBN: 978-3-7643-8748-8. doi:10.1007/978-3-7643-8749-5.
16. S. T. Ali, M. Engliš, and J.-P. Gazeau, "Vector coherent states from Plancherel's theorem, Clifford algebras and matrix domains," Journal of Physics A: Mathematical and General **37**(23), 6067–6089 (2004). doi:10.1088/0305-4470/37/23/008.
17. I. Aremua and M. N. Hounkonnou, "Matrix Vector Coherent States for Landau Levels," Advanced Studies in Theoretical Physics **14**, 237–266 (2020). doi:10.12988/astp.2020.9728.
18. R. Beals and J. Szmigielski, "Meijer G-Functions: A Gentle Introduction," Notices of the American Mathematical Society **60**(7), 866–872 (2013). doi:10.1090/noti1016.
19. J. R. Klauder, "Continuous-Representation Theory. I. Postulates of Continuous-Representation Theory," Journal of Mathematical Physics **4**(8), 1055–1058 (1963). doi:10.1063/1.1704034.
20. J. R. Klauder, K. A. Penson, and J.-M. Sixdeniers, "Constructing coherent states through solutions of Stieltjes and Hausdorff moment problems," Physical Review A **64**(1), 013817 (2001). doi:10.1103/PhysRevA.64.013817.
21. D. Popov, S.-H. Dong, N. Pop, V. Sajfert, and S. Şimon, "Construction of the Barut–Girardello quasi coherent states for the Morse potential," Annals of Physics **339**, 122–134 (2013). doi:10.1016/j.aop.2013.08.018.
22. A. M. Mathai and R. K. Saxena, *Generalized Hypergeometric Functions with Applications in Statistics and Physical Sciences*, Lecture Notes in Mathematics, Vol. 348 (Springer, Berlin, Heidelberg, 1973). ISBN: 978-3-540-06482-4. Series ISSN: 0075-8434. doi:10.1007/BFb0060468.
23. D. Popov and M. Popov, "Some operatorial properties of the generalized hypergeometric coherent states," Physica Scripta **90**(3), 035101 (2015). doi:10.1088/0031-8949/90/3/035101.
24. W.-M. Zhang, D. H. Feng, and R. Gilmore, "Coherent states: Theory and some applications," Reviews of Modern Physics **62**, 867–927 (1990). doi:10.1103/RevModPhys.62.867.
25. J. R. Klauder and B.-S. Skagerstam, *Coherent States: Applications in Physics and Mathematical Physics* (World Scientific, Singapore, 1985). ISBN: 978-9971-966-52-2. doi:10.1142/0096.
26. J.-P. Antoine, F. Bagarello, and J.-P. Gazeau (eds.), *Coherent States and Their Applications: A Contemporary Panorama*, Springer Proceedings in Physics, Vol. 205 (Springer, Cham, 2018). ISBN: 978-3-319-76731-4. Series ISSN: 0930-8989. doi:10.1007/978-3-319-76732-1.
27. Dušan Popov, I. Zaharie, V. Sajfert, I. Luminosu, and Deian Popov, "Quantum Information in the Frame of Coherent States Representation," International Journal of Theoretical Physics **47**(5), 1441–1454 (2008). doi:10.1007/s10773-007-9586-9.

28. M. A. Nielsen and I. L. Chuang, *Quantum Computation and Quantum Information*, 10th anniversary ed. (Cambridge University Press, Cambridge, 2010). ISBN: 978-1-107-00217-3. doi:10.1017/CBO9780511976667.

29. I. S. Gradshteyn and I. M. Ryzhik, *Table of Integrals, Series, and Products*, 7th ed., edited by A. Jeffrey and D. Zwillinger (Academic Press, Amsterdam, 2007). ISBN: 978-0-12-373637-6.

TTMP vol 3 (4), 2026
doi: 10.30511/TTMP.2026.2107096.1099

Transactions in Theoretical and Mathematical Physics



Symmetry Reductions of Boundary Layer Equations of Second Grade Fluids

Mehmet Pakdemirli[1,a]

[1] Department of Mechanical Engineering, Manisa Celal Bayar University, 45140, Muradiye, Manisa, Turkey

Received: 26 September 2026 / Accepted: 07 November 2026 / Published: 10 November 2026

Abstract Boundary layer flow of a second grade fluid is considered. Symmetry analysis has been applied to the equations. The arbitrary functions are the outer velocity appearing in the equations and the two functions in the boundary conditions. The specific forms of the outer velocity for which the principal Lie algebra extends is discussed first. For generalized boundary conditions with three arbitrary functions including the outer velocity, a further group classification is presented. The boundary conditions include classical no slip boundary layer flow, stretching/shrinking sheet flow, Falkner-Skan flow, flow with suction/injection, stagnation point flow and prescribed wall velocities. Group classification results are summarized in tables to guide the researchers. While the main aim in this study is to present a complete group classification for the outer velocity and the generalized boundary conditions, specific boundary conditions are also treated as an example. Flow due to stretching of the permeable plate with suction/injection is considered. With the aid of symmetries, the partial boundary value problem is reduced to an ordinary boundary value problem. It is shown that the reduced boundary value problem possesses exact solutions. While the impermeable wall and permeable wall with suction leads to one solution within the exponential family, the injection case leads to two solutions within the exponential family. This work can be used as a reference work in determining the existence of similarity transformations under various flow conditions for second grade fluids.

keywords: Non-Newtonian Fluids, Boundary Layer Equations, Symmetries of Differential Equations, Stretching Sheet Flow, Suction/Injection.

[a]e-mail: pakdemirli@gmail.com

1 Introduction

The treatment of differential equations in search of exact analytical solutions dates back to the 19th century, with the seminal work of Sophus Lie [1]. Especially for nonlinear equations, the symmetry method proposed by Lie remains the most unified and systematic approach. Many exact solutions obtained by ad hoc methods can be realized to be the consequences of the so-called symmetries of the differential equations. So far, the method has found applications in many mathematical physics problems classified in handbooks [2–4]. The theory is well established and discussed in many reference books [5–7]. To handle the involved algebra in the calculations, symbolic computational programs were written [4, 8]. Pakdemirli [9] presented the symmetry method for solutions of differential equations in a simplified form with minimal theory.

To cover many specific cases, researchers often introduce arbitrary parameters and/or functions into the mathematical models and/or boundary/initial conditions [9]. When the functions/parameters remain in their most general forms, this corresponds to the minimal symmetries, called the principal Lie algebra. The symmetries may extend for some specific forms of the functions/parameters. Determining the minimal symmetries and the higher algebras corresponding to specific forms is the task of group classification [9]. If both the equation and the conditions contain several arbitrary functions/parameters, then a group classification with respect to those in the equation must be performed first, followed by those in the conditions. The present work applies this joint classification approach to the second-grade boundary-layer model with an arbitrary outer velocity and prescribed wall velocities.

This study considers the boundary-layer flow of a second-grade fluid. Coleman and Noll [10] introduced the stress-constitutive relationship for such fluids. Dunn and Fosdick [11] derived the thermodynamic compatibility conditions for the model. Rajagopal et al. [12] discussed theoretical arguments for the existence of a boundary layer in second-grade fluids. Pakdemirli and Şuhubi [13] derived the boundary-layer equations for second-grade fluids using special curvilinear coordinates. They used streamlines and the velocity potentials orthogonal to them as the independent coordinates [14]. This coordinate system helps keep the equations independent of the objects immersed in the fluid. Pakdemirli and Şuhubi [15] calculated the symmetries using exterior differential forms, an alternative to Lie group theory, and presented a reduction for stagnation-point flow. The same curvilinear coordinate system has been employed for third-grade fluids [16], for a special third-grade fluid [17] and for power-law fluids [18].

One mathematical problem in treating second-grade fluids is the paucity of boundary conditions. For the model to be mathematically well posed for a two-dimensional steady-state flow, four boundary conditions are required, but the physical conditions provide only three. Beard and Walters [19] suggested a technique that uses regular perturbation expansions. Because the equation is singular, the regular expansion reduces the order of the equation, eliminating the need for the extra condition. The method is questionable in perturbation theory, where singular problems should be treated by constructing inner and outer expansions (regular solution) and matching them [20, 21]. Garg and Rajagopal [22] instead used physical reasoning for the extra condition and suggested that the solutions be bounded or smooth at infinity. In this work, we follow the second approach of Garg and Rajagopal [22]. Ariel [23] discussed the possibility of obtaining numerical solutions without considering the extra boundary condition at infinity.

Researchers have extensively studied various flow geometries and types to solve boundary-layer flow for second-grade fluid models and their modifications. Examples include stretching sheet flow, flow with suction/injection, stagnation point flow, wedge flow, magnetohydrodynamic (MHD) flow, and nanofluid flow. These models also incorporate heat transfer equations. Abbas et al. [24] investigated the MHD flow with velocity slip, thermal radiation and chemical reaction. Dey and Borah [25] treated the MHD nanofluid flow over a stretching sheet. Reddy et al. [26] investigated MHD flow of a second-grade nanofluid. Hosseinzadeh et al. [27] studied the MHD flow on a curved stretching surface. Nadeem et al. [28] investigated steady-state flow through a horizontal cylinder. Sajid et al. [29] also treated unsteady equations and heat transfer over an expanding boundary. The unsteady flow behaviour was also considered for time-dependent boundary conditions [30]. The moving-plate problem is another flow geometry discussed [31]. Vajravelu and Roper [32] provided an exact exponential solution for stretching-sheet motion with an impermeable wall. A closely related fluid model is the modified second-grade fluid, for which the flow due to plate expansion was analysed [33]. To incorporate shear-thinning and shear-thickening effects into second-grade fluids, power-law second-grade fluids were employed as another modified model [34]. The unsteady case of the model was also considered [35]. When the second-grade effects are eliminated, the model is a special third-grade fluid [36]. The same fluid model was used to investigate flow over a contracting boundary with a magnetic field and thermal radiation [37]. Multiple boundary layers for the second- and third-grade models were extensively treated [38].

One problem in treating stretching sheet flows is the uniqueness of solutions. A proof of uniqueness of solutions is given for stretching sheet motion of second-grade fluids with no suction or injection [39]. For the special non-Newtonian fluid model, Swain et al. [40] reported two solutions. Our results for the stretching sheet solutions with injection have also produced two distinct decaying solutions. However, in the no suction/injection and suction cases, we do not encounter two solutions, which we discuss in the relevant section.

The above-referenced papers all deal with special boundary value problems. In general, they use Lie group theory or its special transformations such as the scaling transformation to obtain an ordinary differential system. The resulting boundary value problems are then solved by exact analytical methods (if they exist), approximate analytical methods (perturbation theory, homotopy analysis method, Taylor series approximations, etc.) or numerical methods (Runge–Kutta with shooting, finite difference methods, etc.). Unlike previous literature, this work does not solve a specific boundary value problem; instead, it analyses the conditions for the success of similarity transformations. To achieve this task, we incorporate an arbitrary outer velocity into the equations and two arbitrary functions into the boundary conditions. The generalised conditions therefore cover a wide range of flow geometries, such as classical no-slip boundary layer flow, stretching sheet flow, stagnation point flow, wedge flow, prescribed wall velocities, suction/injection flow, etc. When all functions remain in their arbitrary forms, no symmetries survive, and constructing similarity solutions becomes impossible. However, for special forms

of the outer velocity function and boundary-condition functions, some symmetries survive, enabling similarity transformations. First, we present the group classification with respect to the outer velocity appearing in the equations, and we summarise the results in a table. Next, we outline the group classification with respect to boundary conditions that include the same outer velocity and summarise the results in tables. Using the given tables and the derived classification equations, we can systematically determine whether similarity solutions exist, rather than relying on trial-and-error methods.

Finally, a sample expanding sheet problem has been treated. The permeable sheet allows for suction or injection. The similarity transformation for the problem was determined. The reduced differential equation belongs to the class of stiff equations, which are hard to solve with initial-value methods. However, for the problem considered, exact analytical solutions exist and are presented. We find that only one solution exists within the exponential family for the cases of impermeable walls and permeable walls with suction. In the case of injection, however, two solutions within the exponential family exist, from which the upper-branch solutions are selected.

2 Boundary layer equations and symmetries

The stress-constitutive relation for an incompressible second-grade fluid is [10]

$$\mathbf{t} = -p\mathbf{I} + \mu\mathbf{A}_1 + \alpha_1\mathbf{A}_2 + \alpha_2\mathbf{A}_1^2, \tag{1}$$

where p is the spherical pressure, μ is the Newtonian viscosity, and α_1 and α_2 are the material constants for the second-grade fluid. The Rivlin–Ericksen tensors are defined as

$$\begin{aligned} \mathbf{A}_1 &= \mathbf{L} + \mathbf{L}^{\mathsf{T}}, \\ \mathbf{A}_2 &= \dot{\mathbf{A}}_1 + \mathbf{A}_1\mathbf{L} + \mathbf{L}^{\mathsf{T}}\mathbf{A}_1, \\ \mathbf{L} &= \operatorname{grad}\mathbf{v}, \end{aligned} \tag{2}$$

where $\mathbf{v}$ is the velocity vector and the dot denotes the total time derivative. For stable solutions that are compatible with thermodynamics, the viscosity and material constants obey [11]

$$\alpha_1 + \alpha_2 = 0, \qquad \mu \geq 0, \qquad \alpha_1 \geq 0. \tag{3}$$

The dimensionless steady-state two-dimensional boundary layer equations are

$$\frac{\partial u}{\partial x} + \frac{\partial v}{\partial y} = 0, \tag{4}$$

$$\begin{aligned} u\frac{\partial u}{\partial x} + v\frac{\partial u}{\partial y} &= U\frac{dU}{dx} + \frac{\partial^2 u}{\partial y^2} \\ &\quad + k_1\left(v\frac{\partial^3 u}{\partial y^3} + u\frac{\partial^3 u}{\partial x\,\partial y^2}\right. \\ &\quad \left. + \frac{\partial u}{\partial x}\frac{\partial^2 u}{\partial y^2} - \frac{\partial u}{\partial y}\frac{\partial^2 u}{\partial x\,\partial y}\right), \end{aligned} \tag{5}$$

where u is the x-component of velocity and v is the y-component inside the boundary layer, and $U(x)$ is the velocity distribution outside the boundary layer, where the flow is inviscid. The parameter k_1 is the dimensionless second-grade material constant. A systematic derivation of the equations using the method of matched asymptotic expansions for a special curvilinear coordinate system was presented earlier [13]. Take $u = W_\varphi$, $v = W_\psi$, $q_B = 1$, and $Q_B = 0$ in the equations to retrieve the above equations in Cartesian coordinates. Alternatively, $m = 0$ can be taken in the equations given by Aksoy et al. [33] and Pakdemirli et al. [34].

The associated conditions are taken fairly general to cover many different flow geometries, as already discussed in the introduction,

$$\begin{aligned} &u(x,0) = A(x), \qquad v(x,0) = B(x), \\ &u(x,\infty) = U(x), \qquad \frac{\partial u}{\partial y}(x,\infty) = 0. \end{aligned} \tag{6}$$

We apply symmetry analysis to Eqs. (4) and (5) [5, 9]. The group transformations are

$$x^* = x + \epsilon\xi_1(x,y,u,v), \tag{7}$$
$$y^* = y + \epsilon\xi_2(x,y,u,v), \tag{8}$$
$$u^* = u + \epsilon\eta^1(x,y,u,v), \tag{9}$$
$$v^* = v + \epsilon\eta^2(x,y,u,v), \tag{10}$$

where ϵ is the group transformation parameter. The generator for the transformation is

$$X = \xi_1\frac{\partial}{\partial x} + \xi_2\frac{\partial}{\partial y} + \eta^1\frac{\partial}{\partial u} + \eta^2\frac{\partial}{\partial v}. \tag{11}$$

The symmetry classification below is carried out for a fixed nonzero second-grade coefficient $k_1 > 0$. The Newtonian limit $k_1 = 0$ is used in Section 5 to check the explicit solution formulas; its enlarged symmetry algebra is outside the scope of the present classification.

Using the straightforward algebra outlined in Bluman and Kumei [5] and Pakdemirli [9], the infinitesimals are eventually found to be

$$\xi_1 = ax + b, \tag{12}$$
$$\xi_2 = c(x), \tag{13}$$
$$\eta^1 = au, \tag{14}$$
$$\eta^2 = c'(x)u. \tag{15}$$

The condition imposed on $U(x)$ is

$$(ax+b)\frac{d}{dx}(UU') - aUU' = 0. \tag{16}$$

The classification of the outer velocity in the equation is based on the above equation. In its most general case, the Lie algebra consists of two finite-parameter transformations and one infinite-parameter transformation $c(x)$. The base generators are

$$\begin{aligned} X_1 &= x\frac{\partial}{\partial x} + u\frac{\partial}{\partial u}, \qquad X_2 = \frac{\partial}{\partial x}, \\ X_\infty &= c(x)\frac{\partial}{\partial y} + c'(x)u\frac{\partial}{\partial v}, \end{aligned} \tag{17}$$

where X_1 represents scalings in the x and u variables and X_2 represents translations in the x-coordinate. Results are compatible with the previous work [15, 33].

3 Group classification (equations)

In Eqs. (4) and (5), group classification is performed with respect to $U(x)$ based on Eq. (16). If the outer velocity is in its most general arbitrary form, then satisfying Eq. (16) requires $a = b = 0$, leaving only the infinite-parameter base symmetry

$$\begin{aligned} \xi_1 &= 0, \qquad \xi_2 = c(x), \\ \eta^1 &= 0, \qquad \eta^2 = c'(x)u. \end{aligned} \tag{18}$$

The above symmetries are the minimal base symmetries when the boundary conditions are disregarded.

To obtain the symmetry extensions, we solve the classifying relation. From Eq. (16), we have

$$\frac{d(UU')}{UU'} = \frac{a\,dx}{ax+b}, \tag{19}$$

with a solution

$$UU' = c_1(ax+b). \tag{20}$$

Upon separation,

$$U\,dU = c_1(ax+b)\,dx, \tag{21}$$

and integrating gives

$$U(x) = \sqrt{C(x+x_0)^2 + D}, \qquad C \neq 0. \tag{22}$$

For this specific form, the infinitesimals are given by Eqs. (12)–(15) with the condition $b = ax_0$. Other special cases follow from the classifying relation.

If $a = 0$, Eq. (16) gives $b\,\frac{d}{dx}(UU') = 0$. The solution for $b \neq 0$ is

$$U(x) = \sqrt{c_1 x + c_2}. \tag{23}$$

The symmetries for this case are

$$\begin{aligned} \xi_1 &= b, \qquad \xi_2 = c(x), \\ \eta^1 &= 0, \qquad \eta^2 = c'(x)u. \end{aligned} \tag{24}$$

If $U = U_0$ is constant or $U = 0$, Eq. (16) is identically satisfied, and the symmetries are in the general form given by Eqs. (12)–(15).

For the linear profile $U = U_0 x$ with $U_0 \neq 0$, Eq. (16) gives $bU_0^2 = 0$. Thus $b = 0$, and the remaining symmetries are

$$\begin{aligned} \xi_1 &= ax, \qquad \xi_2 = c(x), \\ \eta^1 &= au, \qquad \eta^2 = c'(x)u. \end{aligned} \tag{25}$$

If $b = 0$ and $a \neq 0$, Eq. (16) reduces to $x\,\frac{d}{dx}(UU') - UU' = 0$, with a solution

$$U(x) = \sqrt{c_1 x^2 + c_2}. \tag{26}$$

The symmetries for this case are again given by Eq. (25).

Finally, for $U = K(x + x_0)$ with $K \neq 0$, Eq. (16) is satisfied when $b = ax_0$. Table 1 summarises the results.

4 Group classification (boundary conditions)

The conditions are selected in a fairly general form,

$$\begin{aligned} u(x,0) &= A(x), \qquad v(x,0) = B(x), \\ u(x,\infty) &= U(x), \qquad \frac{\partial u}{\partial y}(x,\infty) = 0. \end{aligned} \tag{27}$$

The general form of the conditions includes no-slip flow, stretching-sheet flow, suction or injection, parallel-plate flow, wedge flow, and prescribed wall velocities. For nonlinear partial differential systems, both the equations and the conditions must admit the corresponding Lie group of transformations [5, 9]. Applying the generator obtained from the equations to the boundary conditions may reduce or eliminate the symmetries. The arbitrary functions in the conditions allow us to identify the specific forms for which symmetries survive. For linear partial differential systems, similarity solutions may exist even when the conditions are not invariant [5]. We apply the generator to the finite boundaries and to the boundary conditions.

i) Boundary $y = 0$.

Applying the generator X in Eq. (11) to the boundary $y = 0$ gives

$$\begin{aligned} &X(y)|_{y=0} = 0 \\ &\quad \Longrightarrow \quad \xi_2|_{y=0} = 0 \quad \Longrightarrow \quad c(x) = 0. \end{aligned} \tag{28}$$

Table 1 Group classification (equations).

Outer velocity	Infinitesimals	Parameter restrictions
$U(x)$ arbitrary	$\xi_1 = 0,\ \xi_2 = c(x),\ \eta^1 = 0,\ \eta^2 = c'(x)u$	$a = b = 0$
$U = 0$ or $U = U_0$	$\xi_1 = ax + b,\ \xi_2 = c(x),\ \eta^1 = au,\ \eta^2 = c'(x)u$	No restrictions
$U = \sqrt{c_1 x + c_2}$	$\xi_1 = b,\ \xi_2 = c(x),\ \eta^1 = 0,\ \eta^2 = c'(x)u$	$a = 0$
$U = \sqrt{c_1 x^2 + c_2}$	$\xi_1 = ax,\ \xi_2 = c(x),\ \eta^1 = au,\ \eta^2 = c'(x)u$	$b = 0$
$U = \sqrt{C(x + x_0)^2 + D}$		
$C \neq 0$	$\xi_1 = ax + b,\ \xi_2 = c(x),\ \eta^1 = au,\ \eta^2 = c'(x)u$	$b = ax_0$
$U = K(x + x_0)$		
$K \neq 0$	$\xi_1 = ax + b,\ \xi_2 = c(x),\ \eta^1 = au,\ \eta^2 = c'(x)u$	$b = ax_0$

Therefore, when conditions are imposed at the boundary $y = 0$, the infinite-parameter Lie group of transformations cannot be used for similarity reductions. The boundary at infinity, $y = \infty$, imposes no additional restriction on the generator [5].

ii) Condition $u(x, 0) = A(x)$.

Applying the generator to the first boundary condition gives

$$\begin{aligned} &X\big(u - A(x)\big)\big|_{y=0,\, u=A(x)} = 0 \\ &\quad\Longrightarrow\quad \eta^1\big|_{y=0,\, u=A(x)} = \xi_1|_{y=0}\, A'(x). \end{aligned} \tag{29}$$

Substituting Eqs. (12) and (14) gives

$$aA = (ax + b)A'. \tag{30}$$

If $A(x)$ is arbitrary, Eq. (30) requires $a = b = 0$, and no symmetries survive. If $A = 0$, the classifying relation is identically satisfied and imposes no further restriction. For a nonzero constant $A = A_0$, the relation requires $a = 0$, leaving only the translational symmetry associated with b. For $A = A_0 x$ with $A_0 \neq 0$, as in the stretching-sheet problem, the relation requires $b = 0$, leaving only the scaling symmetry associated with a. More generally, a nonconstant affine profile $A = K_A(x + x_A)$ satisfies the relation when $b = ax_A$. Table 2 summarises the results.

iii) Condition $v(x, 0) = B(x)$.

Applying the generator to the second boundary condition gives

$$\begin{aligned} &X\big(v - B(x)\big)\big|_{y=0,\, u=A(x),\, v=B(x)} = 0 \\ &\quad\Longrightarrow\quad \eta^2\big|_{y=0,\, u=A(x),\, v=B(x)} = \xi_1|_{y=0}\, B'(x). \end{aligned} \tag{31}$$

Since $c(x) = 0$ by Eq. (28), we have $\eta^2 = 0$. The classifying relation is therefore

$$0 = (ax + b)B'. \tag{32}$$

If $B(x)$ is arbitrary, Eq. (32) requires $a = b = 0$, and no nontrivial symmetry survives. If $B = 0$ or $B = B_0$ is constant, the relation is identically satisfied. Thus an impermeable wall or a wall with constant suction or injection imposes no further restriction on the symmetries. Table 3 summarises the results.

iv) Condition $u(x, \infty) = U(x)$.

Applying the generator to the third boundary condition gives

$$\begin{aligned} &X\big(u - U(x)\big)\big|_{u=U(x)} = 0 \\ &\quad\Longrightarrow\quad \eta^1\big|_{u=U(x)} = \xi_1 U'(x). \end{aligned} \tag{33}$$

Substituting Eqs. (12) and (14) yields

$$aU = (ax + b)U'. \tag{34}$$

The outer velocity must satisfy the classifying relations from both the boundary layer equations and the third boundary condition, Eqs. (16) and (34). Table 4 gives the restrictions imposed by the third boundary condition.

v) Condition $u_y(x, \infty) = 0$.

Applying the first prolongation of the generator to the fourth boundary condition gives

$$X^{(1)}(u_y)\Big|_{u_y=0} = 0 \Longrightarrow\quad \eta_2^1\big|_{u_y=0} = 0. \tag{35}$$

The prolonged infinitesimal is obtained from the recursion formulas [5, 9]. For the symmetries considered here, it is

$$\eta_2^1 = au_y. \tag{36}$$

Since η_2^1 vanishes at $u_y = 0$, Eq. (35) imposes no further restriction.

Table 5 collects the classifying relations.

For a specific boundary value problem governed by Eqs. (4)–(6), the admissible similarity transformations can be determined by combining the restrictions in Tables 1–4 or by solving the classifying relations in Table 5 jointly. The constants defining each prescribed profile are held fixed when determining the admitted symmetry algebra. All classifying relations must be satisfied

Table 2 Group classification (first boundary condition).

First boundary condition	Infinitesimals	Parameter restrictions
$A(x)$ arbitrary	$\xi_1 = 0,\ \xi_2 = 0,\ \eta^1 = 0,\ \eta^2 = 0$	$a = b = c(x) = 0$
$A = 0$	$\xi_1 = ax + b,\ \xi_2 = 0,\ \eta^1 = au,\ \eta^2 = 0$	$c(x) = 0$
$A = A_0,\ A_0 \neq 0$	$\xi_1 = b,\ \xi_2 = 0,\ \eta^1 = 0,\ \eta^2 = 0$	$a = c(x) = 0$
$A = A_0 x,\ A_0 \neq 0$	$\xi_1 = ax,\ \xi_2 = 0,\ \eta^1 = au,\ \eta^2 = 0$	$b = c(x) = 0$
$A = K_A(x + x_A)$		
$K_A \neq 0$	$\xi_1 = ax + b,\ \xi_2 = 0,\ \eta^1 = au,\ \eta^2 = 0$	$c(x) = 0,\ b = ax_A$

Table 3 Group classification (second boundary condition).

Second boundary condition	Infinitesimals	Parameter restrictions
$B(x)$ arbitrary	$\xi_1 = 0,\ \xi_2 = 0,\ \eta^1 = 0,\ \eta^2 = 0$	$a = b = c(x) = 0$
$B = 0$	$\xi_1 = ax + b,\ \xi_2 = 0,\ \eta^1 = au,\ \eta^2 = 0$	$c(x) = 0$
$B = B_0$	$\xi_1 = ax + b,\ \xi_2 = 0,\ \eta^1 = au,\ \eta^2 = 0$	$c(x) = 0$

Table 4 Group classification (third boundary condition).

Third boundary condition	Infinitesimals	Parameter restrictions
$U(x)$ arbitrary	$\xi_1 = 0,\ \xi_2 = 0,\ \eta^1 = 0,\ \eta^2 = 0$	$a = b = c(x) = 0$
$U = 0$	$\xi_1 = ax + b,\ \xi_2 = 0,\ \eta^1 = au,\ \eta^2 = 0$	$c(x) = 0$
$U = U_0,\ U_0 \neq 0$	$\xi_1 = b,\ \xi_2 = 0,\ \eta^1 = 0,\ \eta^2 = 0$	$a = c(x) = 0$
$U = U_0 x,\ U_0 \neq 0$	$\xi_1 = ax,\ \xi_2 = 0,\ \eta^1 = au,\ \eta^2 = 0$	$b = c(x) = 0$
$U = K_U(x + x_U)$		
$K_U \neq 0$	$\xi_1 = ax + b,\ \xi_2 = 0,\ \eta^1 = au,\ \eta^2 = 0$	$c(x) = 0,\ b = ax_U$

Table 5 Classifying relations.

Origin	Relation
Boundary layer equations	$(ax + b)\frac{d}{dx}(UU') - aUU' = 0$
First boundary condition	$aA = (ax + b)A'$
Second boundary condition	$0 = (ax + b)B'$
Third boundary condition	$aU = (ax + b)U'$

by the same generator. In particular, nonconstant affine wall and outer velocities admit a common scaling about a shifted origin only when their shifts coincide.

5 Stretching sheet with suction/injection

As a sample boundary value problem, we consider a stretching sheet with constant suction or injection. The fluid moves with the stretching sheet, and the outer velocity at infinity is zero. The boundary conditions are

$$\begin{aligned} &u(x,0) = A_0 x, \qquad v(x,0) = B_0, \\ &u(x,\infty) = 0, \qquad \frac{\partial u}{\partial y}(x,\infty) = 0. \end{aligned} \tag{37}$$

We assume $A_0 > 0$ for the stretching sheet. For $U = 0$, $A = A_0 x$, and $B = B_0$, the restrictions in Tables 1–4, or equivalently the relations in Table 5, give $b = c(x) = 0$. The infinitesimals are

$$\begin{aligned} &\xi_1 = ax, \qquad \xi_2 = 0, \\ &\eta^1 = au, \qquad \eta^2 = 0. \end{aligned} \tag{38}$$

For $a \neq 0$, the characteristic equations for the similarity transformation, after rescaling the group parameter, are

$$\begin{aligned} &\frac{dx}{ds} = x, \qquad \frac{dy}{ds} = 0, \\ &\frac{du}{ds} = u, \qquad \frac{dv}{ds} = 0. \end{aligned} \tag{39}$$

Since y is invariant, the independent similarity variable is

$$\xi = y. \tag{40}$$

The first and third characteristic equations give u/x as an invariant where $x \neq 0$. Thus the velocity in the x-direction is

$$u = xf(\xi). \tag{41}$$

Similarly, v is invariant, so the velocity in the y-direction is

$$v = g(\xi). \tag{42}$$

Substituting Eqs. (40)–(42) into Eqs. (4) and (5) gives the ordinary differential system

$$f + g' = 0, \tag{43}$$

$$f^2 + gf' = f'' + k_1\big(gf''' + 2ff'' - (f')^2\big). \tag{44}$$

The reduced boundary conditions are

$$\begin{aligned} f(0) &= A_0, \qquad g(0) = B_0, \\ f(\infty) &= 0, \qquad f'(\infty) = 0. \end{aligned} \tag{45}$$

The reduced equations are stiff, which makes Runge–Kutta shooting difficult. Shooting requires choosing two initial values so that the conditions at infinity are satisfied. Finite-difference methods are often used for similar problems. Here, the following exponential ansatz satisfies the boundary conditions and yields exact solutions for suitable values of μ and B_1:

$$\begin{aligned} f(\xi) &= A_0 e^{-\mu\xi}, \\ g(\xi) &= B_0 + B_1\big(1 - e^{-\mu\xi}\big), \qquad \mu > 0. \end{aligned} \tag{46}$$

Substitution into Eq. (43) gives

$$B_1 = -\frac{A_0}{\mu}. \tag{47}$$

Using this relation in Eq. (44) yields

$$p(\mu) = k_1 B_0 \mu^3 - (1 + k_1 A_0)\mu^2 - B_0\mu + A_0 = 0. \tag{48}$$

Only positive real roots give decaying exponential profiles that satisfy the conditions at infinity.

For a Newtonian fluid, $k_1 = 0$, and Eq. (48) has a single positive root,

$$\mu = \frac{-B_0 + \sqrt{B_0^2 + 4A_0}}{2} \qquad \text{(Newtonian)}. \tag{49}$$

In the absence of suction or injection, $B_0 = 0$, and the single positive root is

$$\mu = \sqrt{\frac{A_0}{1 + k_1 A_0}} \qquad \text{(no suction/injection)}. \tag{50}$$

For $A_0 > 0$ and $k_1 > 0$, Eq. (48) has exactly one positive root when $B_0 \le 0$ and exactly two positive roots when $B_0 > 0$. Thus the exponential family (46) contains one decaying solution for an impermeable wall or for suction, and two distinct decaying solutions for injection. For $k_1 = 0$, there is one positive root for every B_0. These counts apply to the exponential family.

Table 6 Numerical results for the parameter μ.

A_0	B_0	k_1	μ	Number of positive roots
1	1	1	0.5550, 2.2470	Two
1.5	1	1	0.6728, 2.6640	Two
2	1	1	0.7459, 3.1149	Two
1	−1	1	0.8019	One
1	0	1	0.7071	One
1	1	0	0.6180	One
1	1	2	0.5000, 1.6180	Two

For suction, Descartes' rule of signs gives exactly one positive root. The case $B_0 = 0$ follows from Eq. (50). For injection, $p(0) = A_0 > 0$, $p\big(k_1^{-1/2}\big) = -\frac{1}{k_1} < 0$, and $\lim_{\mu\to+\infty} p(\mu) = +\infty$. There is therefore one positive root on each side of $k_1^{-1/2}$, and Descartes' rule of signs excludes additional positive roots.

The roots of Eq. (48) are determined using the following root-finding algorithm with fourth-order convergence [41].

$$\begin{aligned} \mu_{n+1} = \mu_n &- \frac{p(\mu_n)}{p'(\mu_n)} - \frac{p(\mu_n)^2 p''(\mu_n)}{2[p'(\mu_n)]^3} \\ &+ p(\mu_n)^3 \frac{p'(\mu_n)p'''(\mu_n) - 3[p''(\mu_n)]^2}{6[p'(\mu_n)]^5}. \end{aligned} \tag{51}$$

Table 6 lists the positive roots of the cubic polynomial used to generate the figures.

Returning to the original variables, the analytical solutions are

$$\begin{aligned} u &= xf(y) = A_0 x e^{-\mu y}, \\ v &= g(y) = B_0 - \frac{A_0}{\mu}\big(1 - e^{-\mu y}\big), \qquad \mu > 0. \end{aligned} \tag{52}$$

Figures 1 and 2 show the profiles f and g, associated with the x- and y-components of velocity, respectively, for various stretching rates. As the stretching rate increases, the tangential velocity increases near the wall (Fig. 1). Farther from the wall, the profiles cross in a narrow region and then approach the zero outer velocity. The normal velocity decreases as the stretching rate increases (Fig. 2).

For $B_0 = 1$, each stretching rate shown admits two decaying exponential solutions, as listed in Table 6. The figures show the branch associated with the smaller positive root of Eq. (48), which gives slower decay of the tangential velocity. The temporal stability of the two branches remains undetermined.

Figures 3 and 4 show the effect of suction and injection. The values $B_0 = -1$, $B_0 = 1$, and $B_0 = 0$ correspond to suction, injection, and an impermeable wall, respectively.

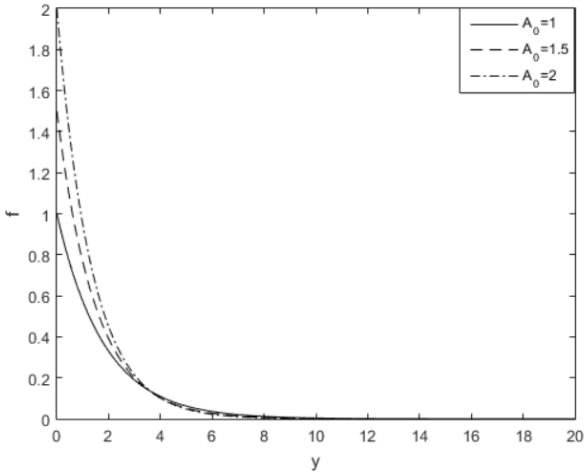


Fig. 1 Profiles of f for various stretching-sheet rates A_0, with $B_0 = 1$ and $k_1 = 1$.

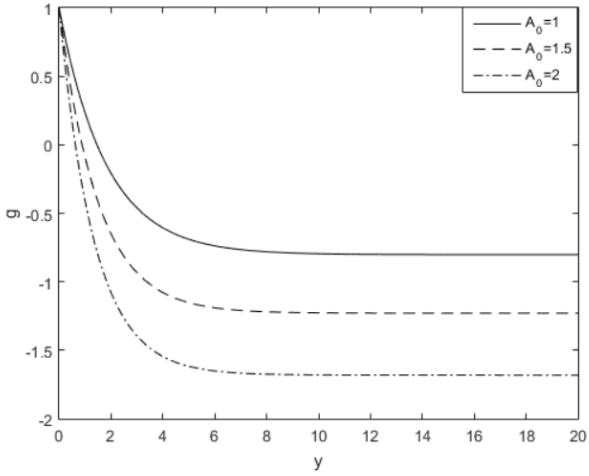


Fig. 2 Profiles of g for various stretching-sheet rates A_0, with $B_0 = 1$ and $k_1 = 1$.

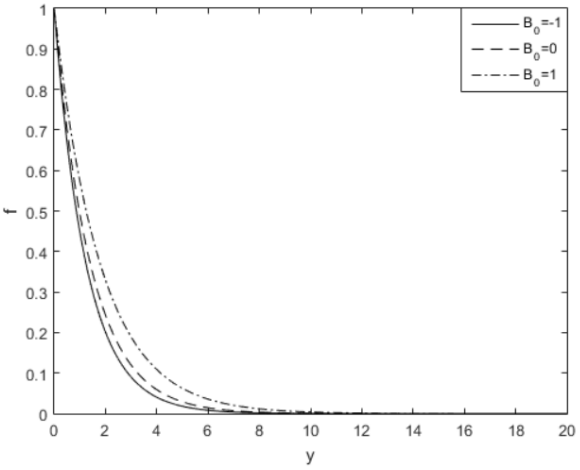


Fig. 3 Profiles of f for various suction and injection velocities B_0, with $A_0 = 1$ and $k_1 = 1$.

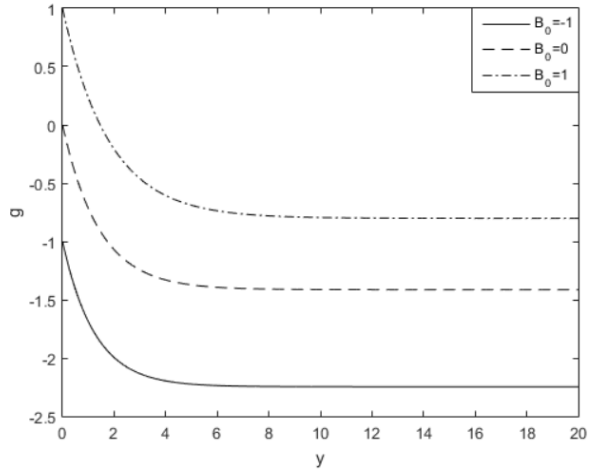


Fig. 4 Profiles of g for various suction and injection velocities B_0, with $A_0 = 1$ and $k_1 = 1$.

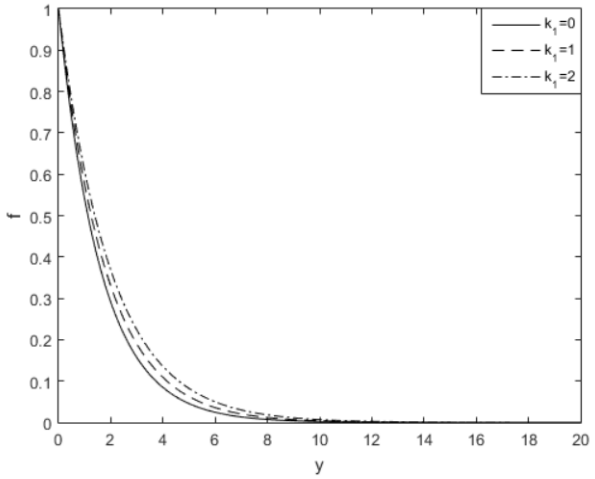


Fig. 5 Profiles of f for various second-grade coefficients k_1, with $A_0 = 1$ and $B_0 = 1$.

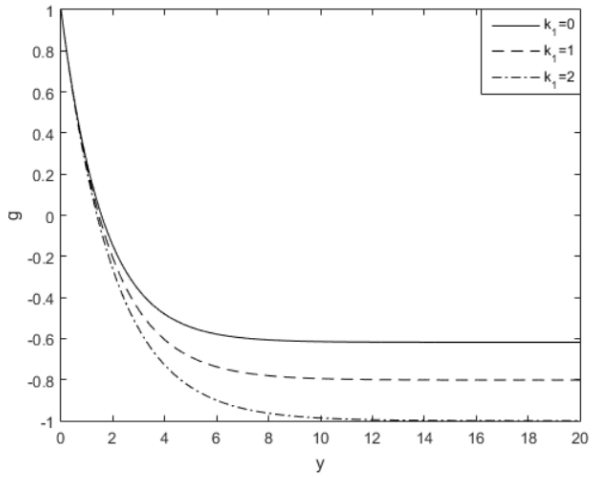


Fig. 6 Profiles of g for various second-grade coefficients k_1, with $A_0 = 1$ and $B_0 = 1$.

As the wall condition changes from suction to injection, the tangential velocity increases slightly within the boundary layer (Fig. 3). The normal velocity approaches a negative value far from the wall, even in the injection case (Fig. 4). Among the cases shown, only injection admits two decaying exponential solutions. The profiles shown for injection correspond to the smaller positive root μ of Eq. (48).

Figures 5 and 6 show the effect of the dimensionless second-grade coefficient k_1. The value $k_1 = 0$ corresponds to the Newtonian limit. For the second-grade fluid, we consider positive values of k_1, consistent with the thermodynamic compatibility conditions in Eq. (3).

As k_1 increases, the tangential velocity decays more slowly and the boundary layer thickens (Fig. 5). The normal velocity decreases with increasing k_1 away from the wall (Fig. 6).

6 Concluding remarks

This study considers the flow of a second-grade fluid. The boundary layer restrictions are considered. Fairly general boundary conditions are used to cover a range of flow conditions. We use a symmetry group approach for both the equations and the boundary conditions. This work systematically classifies, for the present second-grade boundary-layer model, the outer-velocity and prescribed wall-velocity profiles compatible with Lie point symmetry reductions. The tables systematically outline the conditions under which similarity-type solutions exist. Using these classifications, we treat the stretching sheet problem with suction/injection. The scaling symmetry reduces the original system to an ordinary differential system. We present exact analytical solutions for the reduced system. We discuss the effects of stretching-sheet rates, suction or injection, and the non-Newtonian coefficient. We find that the boundary value problem has two solutions within the exponential family for injection. For suction or no suction/injection, however, there is only one solution within the exponential family. This study focuses on the classification problem, which reveals the existence of similarity transformations for special forms of the outer velocity and boundary conditions. Detailed analysis of specific boundary value problems and physical interpretations of the results is beyond the scope and left for further research.

References

1. S. Lie, *Vorlesungen über continuierliche Gruppen mit geometrischen und anderen Anwendungen*, edited by G. Scheffers, B. G. Teubner, Leipzig, 1893.
2. N. H. Ibragimov (ed.), *CRC Handbook of Lie Group Analysis of Differential Equations*, Vol. 1: *Symmetries, Exact Solutions, and Conservation Laws*, CRC Press, Boca Raton, 1993. DOI: 10.1201/9781003419808.
3. N. H. Ibragimov (ed.), *CRC Handbook of Lie Group Analysis of Differential Equations*, Vol. 2: *Applications in Engineering and Physical Sciences*, CRC Press, Boca Raton, 1995.
4. N. H. Ibragimov (ed.), *CRC Handbook of Lie Group Analysis of Differential Equations*, Vol. 3: *New Trends in Theoretical Developments and Computational Methods*, CRC Press, Boca Raton, 1996. DOI: 10.1201/9781003575221.
5. G. W. Bluman and S. Kumei, *Symmetries and Differential Equations*, Springer-Verlag, New York, 1989. DOI: 10.1007/978-1-4757-4307-4.
6. P. J. Olver, *Applications of Lie Groups to Differential Equations*, Springer-Verlag, New York, 1986. DOI: 10.1007/978-1-4684-0274-2.
7. H. Stephani, *Differential Equations: Their Solution Using Symmetries*, Cambridge University Press, Cambridge, 1989. DOI: 10.1017/CBO9780511599941.
8. G. Baumann, *Symmetry Analysis of Differential Equations with Mathematica*, Springer-Verlag, New York, 2000. DOI: 10.1007/978-1-4612-2110-4.
9. M. Pakdemirli, *Solutions of Differential Equations by Symmetry Methods*, Deep Science, New Delhi, 2026.
10. B. D. Coleman and W. Noll, An approximation theorem for functionals, with applications in continuum mechanics, *Archive for Rational Mechanics and Analysis* **6** (1960), 355–370. DOI: 10.1007/BF00276168.
11. J. E. Dunn and R. L. Fosdick, Thermodynamics, stability, and boundedness of fluids of complexity 2 and fluids of second grade, *Archive for Rational Mechanics and Analysis* **56**(3) (1974), 191–252. DOI: 10.1007/BF00280970.
12. K. R. Rajagopal, A. S. Gupta, and A. S. Wineman, On a boundary layer theory for non-Newtonian fluids, *International Journal of Engineering Science* **18**(6) (1980), 875–883. DOI: 10.1016/0020-7225(80)90035-X.
13. M. Pakdemirli and E. S. Şuhubi, Boundary layer theory for second order fluids, *International Journal of Engineering Science* **30**(4) (1992), 523–532. DOI: 10.1016/0020-7225(92)90042-F.
14. S. Kaplun, The role of coordinate systems in boundary-layer theory, *Journal of Applied Mathe-*

matics and Physics ZAMP **5**(2) (1954), 111–135. DOI: 10.1007/BF01600771.

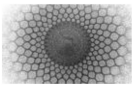
15. M. Pakdemirli and E. S. Şuhubi, Similarity solutions of boundary layer equations for second order fluids, *International Journal of Engineering Science* **30**(5) (1992), 611–629. DOI: 10.1016/0020-7225(92)90006-3.
16. M. Pakdemirli, The boundary layer equations of third-grade fluids, *International Journal of Non-Linear Mechanics* **27**(5) (1992), 785–793. DOI: 10.1016/0020-7462(92)90034-5.
17. M. Yürüsoy, Similarity solutions to boundary layer equations for third-grade non-Newtonian fluid in special coordinate system, *Journal of Theoretical and Applied Mechanics* **41**(4) (2003), 775–787.
18. M. Pakdemirli, Boundary layer flow of power-law fluids past arbitrary profiles, *IMA Journal of Applied Mathematics* **50**(2) (1993), 133–148. DOI: 10.1093/imamat/50.2.133.
19. D. W. Beard and K. Walters, Elastico-viscous boundary-layer flows I. Two-dimensional flow near a stagnation point, *Mathematical Proceedings of the Cambridge Philosophical Society* **60**(3) (1964), 667–674. DOI: 10.1017/S0305004100038147.
20. A. H. Nayfeh, *Introduction to Perturbation Techniques*, John Wiley & Sons, New York, 1981.
21. M. Pakdemirli and İ. T. Dolapci, *New Trends in Perturbation Methods with Applications*, Cambridge Scholars Publishing, Newcastle upon Tyne, 2026.
22. V. K. Garg and K. R. Rajagopal, Flow of a non-Newtonian fluid past a wedge, *Acta Mechanica* **88**(1–2) (1991), 113–123. DOI: 10.1007/BF01170596.
23. P. D. Ariel, On extra boundary condition in the stagnation point flow of a second grade fluid, *International Journal of Engineering Science* **40**(2) (2002), 145–162. DOI: 10.1016/S0020-7225(01)00031-3.
24. Z. Abbas, A. Gull, G. Nazik, M. Y. Rafiq, and M. Mujahid, Investigation of oscillatory second-grade fluid flow through porous media under slip and thermal influences, *Physics Open* **26** (2026), 100363. DOI: 10.1016/j.physo.2025.100363.
25. D. Dey and R. Borah, MHD nanofluid flow with energy transfer over a porous stretching surface by using a second-grade fluid model, *Numerical Heat Transfer, Part A: Applications* **86**(5) (2025), 1313–1327. DOI: 10.1080/10407782.2023.2278715.
26. S. C. Reddy, K. K. Asogwa, M. F. Yassen, Adnan, Z. Iqbal, S. M-Eldin, B. Ali, and Swarnalatha KM, Dynamics of MHD second-grade nanofluid flow with activation energy across a curved stretching surface, *Frontiers in Energy Research* **10** (2022), 1007159. DOI: 10.3389/fenrg.2022.1007159.
27. K. Hosseinzadeh, M. R. Mardani, M. Paikar, A. Hasibi, T. Tavangar, M. Nimafar, and M. B. Shafii, Investigation of second grade viscoelastic non-Newtonian nanofluid flow on the curve stretching surface in presence of MHD, *Results in Engineering* **17** (2023), 100838. DOI: 10.1016/j.rineng.2022.100838.
28. S. Nadeem, A. Rehman, C. Lee, and J. Lee, Boundary layer flow of second grade fluid in a cylinder with heat transfer, *Mathematical Problems in Engineering* **2012**(1) (2012), 640289. DOI: 10.1155/2012/640289.
29. M. Sajid, I. Ahmad, T. Hayat, and M. Ayub, Unsteady flow and heat transfer of a second grade fluid over a stretching sheet, *Communications in Nonlinear Science and Numerical Simulation* **14**(1) (2009), 96–108. DOI: 10.1016/j.cnsns.2007.07.014.
30. S. T. Saeed, M. B. Riaz, D. Baleanu, A. Akgül, and S. M. Husnine, Exact analysis of second grade fluid with generalized boundary conditions, *Intelligent Automation & Soft Computing* **28**(2) (2021), 547–559. DOI: 10.32604/iasc.2021.015982.
31. K. Sadeghy and M. Sharifi, Local similarity solution for the flow of a "second-grade" viscoelastic fluid above a moving plate, *International Journal of Non-Linear Mechanics* **39**(8) (2004), 1265–1273. DOI: 10.1016/j.ijnonlinmec.2003.08.005.
32. K. Vajravelu and T. Roper, Flow and heat transfer in a second grade fluid over a stretching sheet, *International Journal of Non-Linear Mechanics* **34**(6) (1999), 1031–1036. DOI: 10.1016/S0020-7462(98)00073-0.
33. Y. Aksoy, M. Pakdemirli, and C. M. Khalique, Boundary layer equations and stretching sheet solutions for the modified second grade fluid, *International Journal of Engineering Science* **45**(10) (2007), 829–841. DOI: 10.1016/j.ijengsci.2007.05.006.
34. M. Pakdemirli, Y. Aksoy, M. Yürüsoy, and C. M. Khalique, Symmetries of boundary layer equations of power-law fluids of second grade, *Acta Mechanica Sinica* **24**(6) (2008), 661–670. DOI: 10.1007/s10409-008-0172-z.
35. A. Keçebaş and M. Yürüsoy, Numerical solutions of unsteady boundary layer equations for a generalized second grade fluid, *Journal of Theoretical and Applied Mechanics* **49**(1) (2011), 71–82.
36. M. Yürüsoy and M. Pakdemirli, Exact solutions of boundary layer equations of a special non-Newtonian fluid over a stretching sheet, *Mechanics Research Communications* **26**(2) (1999), 171–175.

DOI: 10.1016/S0093-6413(99)00009-9.

37. R. S. Chowdhury, G. M. Sarkar, B. Sahoo, and B. Diyali, Statistical and numerical analysis of the flow of a special third grade fluid driven by a shrinking surface, *European Journal of Mechanics – B/Fluids* **113** (2025), 204275. DOI: 10.1016/j.euromechflu.2025.204275.
38. M. Pakdemirli, Conventional and multiple deck boundary layer approach to second and third grade fluids, *International Journal of Engineering Science* **32**(1) (1994), 141–154. DOI: 10.1016/0020-7225(94)90156-2.
39. W. C. Troy, E. A. Overman, G. B. Ermentrout, and J. P. Keener, Uniqueness of flow of a second-order fluid past a stretching sheet, *Quarterly of Applied Mathematics* **44**(4) (1987), 753–755. DOI: 10.1090/qam/872826.
40. S. Swain, G. M. Sarkar, and B. Sahoo, Dual solutions and linear temporal stability analysis of mixed convection flow of non-Newtonian special third grade fluid with thermal radiation, *International Journal of Thermal Sciences* **189** (2023), 108262. DOI: 10.1016/j.ijthermalsci.2023.108262.
41. M. Pakdemirli and H. Boyacı, Generation of root finding algorithms via perturbation theory and some formulas, *Applied Mathematics and Computation* **184** (2007), 783–788. DOI: 10.1016/j.amc.2006.05.207.

TTMP vol 3 (4), 2026
doi: 10.30511/TTMP.2026.2108620.1101

Transactions in Theoretical and Mathematical Physics



Analytical, Numerical, and PINN Analysis of the ABC Fractional GK Equation: A Compatibility-Aware Benchmark Study

Md. Akher Chowdhury[1], **Md. Masudar Rahman**[2,a], **Md. Zahangir Alam**[2], **Md. Ashik Iqbal**[3]

[1]Department of Mathematics, Begum Rokeya University, Rangpur-5404, Bangladesh
[2]Department of Mathematics, Bangladesh Army University of Engineering & Technology, Natore, Bangladesh
[3]Department of Applied Mathematics, University of Rajshahi, Rajshahi-6205, Bangladesh

Received: 11 Ocotber 2026 / Accepted: 10 November 2026 / Published: 14 November 2026

Abstract We develop a framework for comparing analytical, numerical, and machine-learning solutions of a time-fractional Gardner–Kawahara (GK) equation with the Atangana–Baleanu derivative in the Caputo sense (ABC). We construct a forced benchmark in which the nonlocal Mittag–Leffler (ML) memory law, the prescribed initial state, and the source term are compatible at the initial time. We solve the same benchmark using three approaches: a Laplace–Adomian decomposition method (LADM), a Fourier pseudospectral discretization with an AB predictor–corrector scheme for the history term, and a physics-informed neural network (PINN) based on the equivalent Atangana–Baleanu integral equation.

We assess the six-component LADM approximation over the selected short-time interval. At the lowest fractional order considered, the last retained component is less than 1% of the total solution, and the normalized integral residual is approximately 3.10×10^{-3}. The numerical solution exhibits coarse-to-refined relative differences of order 10^{-8} to 10^{-7}. At $t = 0.10$, the relative L_2 error between the numerical and LADM solutions ranges from 4.42×10^{-8} for $\alpha = 1.00$ to 2.92×10^{-3} for $\alpha = 0.85$. For $\alpha = 0.90$, the PINN reproduces the numerical wave field with relative L_2 errors of 1.07% over the full space–time domain and 1.26% at the final time.

Both the LADM and numerical solutions show that decreasing the fractional order strengthens the forced transient response in this benchmark. The benchmark provides a reproducible setting for cross-validating semi-analytical decomposition, spectral computation, and physics-informed learning for the ABC fractional GK equation.

Keywords: Gardner-Kawahara equation; Laplace Adomian decomposition; Fourier pseudo spectral; predictor-corrector method; physics-informed neural network

1 Introduction

Fractional calculus extends differentiation and integration from integer orders to non-integer orders and provides a mathematical language for systems with hereditary effects, anomalous transport, long-range temporal dependence, and nonlocal constitutive behaviour [1–4]. Based on the Riemann–Liouville and Caputo operators, classical fractional models have been widely used, but their power-law kernels are singular at the origin. The AB family of operators was proposed with a non-singular, nonlocal ML kernel, providing an alternative memory law that retains a Caputo-like treatment of initial data while avoiding a singular kernel [5, 6]. Numerical approximations and time-integration procedures for the AB derivative have since been developed for a variety of fractional differential equations [7–10].

[a]Corresponding author: masudarmath@gmail.com

The Kawahara equation is a fifth-order nonlinear dispersive evolution equation associated with oscillatory solitary waves, capillary–gravity wave propagation, and magneto-acoustic phenomena-related problems [11]. In near-critical interfacial-wave forms, the GK equation arises as a natural extension that combines quadratic and cubic nonlinearities with third- and fifth-order dispersion [12]. This combination makes the model substantially richer than the classical KdV, modified KdV, or Kawahara equations because the competing nonlinear and dispersive mechanisms can alter amplitude, polarity, oscillatory tails, and propagation structure.

A broad literature has addressed Kawahara-type equations by both the analytical and numerical techniques. The Adomian decomposition method has been used for classical and fractional Kawahara models [13–16], while AB memory has been introduced into a modified Kawahara equation and treated using a homotopy-analysis-transform framework [17]. Also, the exact or semi-analytical solutions have been developed for fractional Kawahara equations under conformable or Caputo-type formulations [18, 19]. For this type of GK equation, recent numerical studies have used high-order B-spline collocation and finite-element strategies [20, 21]. Fourier pseudo-spectral methods are also attractive for periodic, high-order dispersive equations because derivatives can be computed with spectral accuracy via fast Fourier transforms [22].

In parallel, physics-informed neural networks (PINNs) have emerged as a framework for embedding differential equations directly into neural-network training [23–26]. By incorporating history-dependent residuals, fractional PINNs extend this concept to nonlocal operators [24]. Recently, PINNs have been used for inverse GK parameter identification [27], and a dedicated PINN framework has been reported for modified Kawahara equations [28]. These developments establish the feasibility of learning high-order nonlinear wave dynamics, but they do not eliminate the need for independent analytical and numerical validation, particularly when a nonlocal fractional derivative is present.

A vital issue in ABC fractional evolution problems is the compatibility between the initial state and the local part of the associated AB integral operator. If a nonzero initial profile is combined with a spatial operator that is already nonzero at $t = 0$, a naive benchmark will exhibit an apparent start-up mismatch even when the algebraic derivation is otherwise correct. As a result, the present work adopts a zero initial state and a time-dependent forcing that vanishes at $t = 0$, which produces a nontrivial wave after the initial instant while preserving compatibility of the fractional model.

1.1 Novelty and contributions

The novelty of this paper lies in the combined formulation and validation strategy. In the literature reviewed for this study, individual works have considered ABC-modified Kawahara models [17], Caputo or conformable fractional Kawahara equations [15, 18, 19], classical GK numerical schemes [20, 21], and PINN formulations for classical Gardner–Kawahara or modified Kawahara equations [27, 28]. The reviewed studies do not provide the same combination of an ABC time-fractional GK equation containing both quadratic and cubic nonlinearities; an explicitly compatibility-aware forced benchmark; a Laplace–Adomian analytical approximation; an independent Fourier pseudo-spectral ABC history solver; and a PINN validated against the converged numerical field on the same benchmark.

Therefore, the study makes four connected contributions. First, it formulates a compatible forced ABC GK test problem that avoids the start-up inconsistency encountered with an incompatible nonzero initial state. Secondly, it constructs and validates a six-component LADM approximation for several fractional orders. Thirdly, it produces an independent grid-converged Fourier pseudo-spectral solution and uses it to quantify the truncation error of the analytical series. Lastly, it demonstrates that an integral-form PINN can recover the representative fractional wave field from the governing physics and constraints, thereby providing a three-way analytical-numerical-PINN assessment rather than a single-method demonstration. So, a further contribution is the consolidated cross-method visualization: fractional-order profiles, space-time surfaces, pairwise solution overlays, and absolute-error diagnostics are compared

under the same parameter set, so agreement is assessed visually and quantitatively rather than by a single error metric.

The remainder of the paper is organized as follows. In Section 2, we state the AB definitions used throughout the work. Section 3 gives the analytical, numerical, and PINN methodologies. Sections 4, 5, and 6 present the corresponding applications and results. Section 7 compares the three solution strategies. Section 8 positions the results relative to related studies. In Section 9, we give the main conclusions and future directions.

2 AB Fractional Definitions

Let $0 < \alpha \le 1$ and f be sufficiently smooth on $[0,T]$. The AB derivative in the Caputo sense is defined by [5, 6]

$$
\begin{aligned}
{}^{\mathrm{ABC}}D_t^{\alpha} f(t) = \frac{B(\alpha)}{1-\alpha}\int_0^t f'(\tau) \\
\times E_\alpha\left[-\frac{\alpha}{1-\alpha}(t-\tau)^{\alpha}\right]\mathrm{d}\tau,
\end{aligned}
\tag{1}
$$

where $E_\alpha(z)$ denotes the one-parameter ML function,

$$
E_\alpha(z) = \sum_{k=0}^{\infty} \frac{z^k}{\Gamma(\alpha k+1)}. \tag{2}
$$

The normalization function satisfies $B(0) = B(1) = 1$. In the present computations, we use the normalization

$$
B(\alpha) = 1-\alpha+\frac{\alpha}{\Gamma(\alpha)}, \tag{3}
$$

which is adopted consistently in the analytical, numerical, and PINN implementations. The Laplace transform of the ABC derivative can be written as

$$
\mathscr{L}\left\{{}^{\mathrm{ABC}}D_t^{\alpha} f(t)\right\}(s) = \frac{B(\alpha)}{1-\alpha}\frac{s^{\alpha}F(s)-s^{\alpha-1}f(0)}{s^{\alpha}+\alpha/(1-\alpha)}. \tag{4}
$$

The fractional integral associated with the AB operator is [5, 6]

$$
\begin{aligned}
{}^{\mathrm{AB}}I_t^{\alpha} f(t) = \frac{1-\alpha}{B(\alpha)} f(t) \\
+\frac{\alpha}{B(\alpha)\Gamma(\alpha)}\int_0^t (t-\tau)^{\alpha-1} f(\tau)\,\mathrm{d}\tau.
\end{aligned}
\tag{5}
$$

Equation (5) contains a local contribution and a history integral. This decomposition is central to all three methods used below. LADM applies it analytically, the numerical scheme approximates the history integral by product integration, and the PINN enforces the same integral relation through its physics loss.

3 Methodology

The general forced ABC fractional Gardner–Kawahara equation considered in this work is

$$
\begin{aligned}
{}^{\mathrm{ABC}}D_t^{\alpha} u + cu_x + auu_x - bu^2u_x \\
+\mu u_{xxx} + \nu u_{xxxxx} = S(x,t), \qquad 0 < \alpha \le 1.
\end{aligned}
\tag{6}
$$

We define the GK spatial operator by

$$
\mathscr{G}(u) = cu_x + auu_x - bu^2u_x + \mu u_{xxx} + \nu u_{xxxxx}. \tag{7}
$$

The evolution equation takes the compact form

$$
{}^{\mathrm{ABC}}D_t^{\alpha} u = S(x,t) - \mathscr{G}(u). \tag{8}
$$

Periodic spatial boundary conditions are used in the benchmark because they are naturally compatible with the Fourier discretization and the periodic forcing selected in Section 4.

3.1 Analytical Methodology: Laplace–Adomian Decomposition Method

Applying the Laplace transform in time to Eq. (16), using Eq. (4), and then inverting gives the equivalent AB integral equation

$$
\begin{aligned}
u(x,t) = \phi(x) + {}^{\mathrm{AB}}I_t^{\alpha}\left[S(x,t) - \mathscr{G}(u)\right], \\
\phi(x) = u(x,0).
\end{aligned}
\tag{9}
$$

The LADM solution is expanded as

$$
u(x,t) = \sum_{n=0}^{\infty} u_n(x,t), \tag{10}
$$

where the quadratic nonlinear term uu_x is decomposed into Adomian components

$$
A_n = \frac{1}{n!}\frac{\mathrm{d}^n}{\mathrm{d}\lambda^n}\left[\left(\sum_{k=0}^{\infty}\lambda^k u_k\right)\left(\sum_{k=0}^{\infty}\lambda^k u_{k,x}\right)\right]_{\lambda=0}, \tag{11}
$$

while the cubic-gradient term u^2u_x is written as

$$
C_n = \frac{1}{n!}\frac{\mathrm{d}^n}{\mathrm{d}\lambda^n}\left[\left(\sum_{k=0}^{\infty}\lambda^k u_k\right)^2\left(\sum_{k=0}^{\infty}\lambda^k u_{k,x}\right)\right]_{\lambda=0}. \tag{12}
$$

The nth decomposed spatial contribution is therefore

$$
G_n = cu_{n,x} + aA_n - bC_n + \mu u_{n,xxx} + \nu u_{n,xxxxx}. \tag{13}
$$

For a forced problem, the leading component is chosen as

$$u_0(x,t) = \phi(x) + {}^{\mathrm{AB}}I_t^{\alpha} S(x,t), \tag{14}$$

and the remaining components are generated recursively through

$$u_{n+1}(x,t) = -{}^{\mathrm{AB}}I_t^{\alpha} G_n(x,t), \qquad n = 0,1,2,\ldots. \tag{15}$$

After $M+1$ components, the analytical approximation is The evolution equation takes the compact form

$${}^{\mathrm{ABC}}D_t^{\alpha} u = S(x,t) - \mathscr{G}(u). \tag{16}$$

Periodic spatial boundary conditions are used in the benchmark because they are naturally compatible with the Fourier discretization and the periodic forcing selected in Section 4.

3.2 Analytical Methodology: Laplace–Adomian Decomposition Method

Applying the Laplace transform in time to Eq. (16), using Eq. (4), and then inverting gives the equivalent AB integral equation

$$\begin{aligned} u(x,t) &= \phi(x) + {}^{\mathrm{AB}}I_t^{\alpha}\left[S(x,t) - \mathscr{G}(u)\right], \\ \phi(x) &= u(x,0). \end{aligned} \tag{17}$$

The LADM solution is expanded as

$$u(x,t) = \sum_{n=0}^{\infty} u_n(x,t), \tag{18}$$

where the quadratic nonlinear term uu_x is decomposed into Adomian components

$$A_n = \frac{1}{n!}\frac{\mathrm{d}^n}{\mathrm{d}\lambda^n}\left[\left(\sum_{k=0}^{\infty}\lambda^k u_k\right)\left(\sum_{k=0}^{\infty}\lambda^k u_{k,x}\right)\right]_{\lambda=0}, \tag{19}$$

while the cubic-gradient term u^2u_x is written as

$$C_n = \frac{1}{n!}\frac{\mathrm{d}^n}{\mathrm{d}\lambda^n}\left[\left(\sum_{k=0}^{\infty}\lambda^k u_k\right)^2\left(\sum_{k=0}^{\infty}\lambda^k u_{k,x}\right)\right]_{\lambda=0}. \tag{20}$$

The nth decomposed spatial contribution is therefore

$$G_n = cu_{n,x} + aA_n - bC_n + \mu u_{n,xxx} + \nu u_{n,xxxxx}. \tag{21}$$

For a forced problem, the leading component is chosen as

$$u_0(x,t) = \phi(x) + {}^{\mathrm{AB}}I_t^{\alpha} S(x,t), \tag{22}$$

and the remaining components are generated recursively through

$$u_{n+1}(x,t) = -{}^{\mathrm{AB}}I_t^{\alpha} G_n(x,t), \qquad n = 0,1,2,\ldots. \tag{23}$$

After $M+1$ components, the analytical approximation is

$$u_{\mathrm{LADM}}^{(M)}(x,t) = \sum_{n=0}^{M} u_n(x,t). \tag{24}$$

The convergence assessment in Section 4 is based on the relative size of the last retained component, preservation of the initial condition, and substitution of the truncated series into the integral equation. The AB integral form is particularly useful because it avoids direct numerical evaluation of the ML kernel during the LADM recursion.

3.3 Numerical Methodology: Fourier Pseudo-spectral ABC Predictor–Corrector Scheme

On the periodic spatial interval $[-\pi,\pi]$, we introduce a uniform Fourier grid,

$$\begin{aligned} x_j &= -\pi + j\Delta x, \qquad \Delta x = \frac{2\pi}{N_x}, \\ & j = 0,1,\ldots,N_x-1, \end{aligned} \tag{25}$$

and discretize the time interval as

$$t_n = n\Delta t, \qquad \Delta t = \frac{T}{N_t}, \quad n = 0,1,\ldots,N_t. \tag{26}$$

If $\widehat{U}(k,t)$ denotes the discrete Fourier transform of the nodal vector $U(t)$, then the mth spatial derivative is evaluated spectrally by

$$D_x^m U = \mathscr{F}^{-1}\left[(\mathrm{i}k)^m \widehat{U}\right]. \tag{27}$$

A two-thirds de-aliasing filter is applied to nonlinear products to reduce aliasing contamination. After spatial discretization, Eq. (16) becomes the fractional system

$$\begin{aligned} {}^{\mathrm{ABC}}D_t^{\alpha} U(t) &= F(U,t) \\ &= S(t) - \mathscr{G}_h(U). \end{aligned} \tag{28}$$

Using Eq. (5), the discrete history contribution is constructed by product-linear integration. Let

$$\delta_m^{(\alpha)} = (m+1)^{\alpha} - m^{\alpha}. \tag{29}$$

The linear-interpolation weights used over each past subinterval are

$$A_m = \frac{(m+1)^{\alpha+1} - m^{\alpha+1}}{\alpha+1} - \frac{m\,\delta_m^{(\alpha)}}{\alpha}, \tag{30}$$

and

$$B_m = \frac{(m+1)\delta_m^{(\alpha)}}{\alpha} - \frac{(m+1)^{\alpha+1} - m^{\alpha+1}}{\alpha+1}. \tag{31}$$

At each new time level, the memory integral is approximated by a weighted sum of previous right-hand-side values. A predictor is first formed from the known history, and a corrected value is then obtained by re-evaluating the nonlinear terms. In Fourier space, the stiff third- and fifth-order linear dispersive contributions are treated semi-implicitly, while the nonlinear terms are updated by fixed-point iteration. This separation reduces the severe time-step restriction that would otherwise arise from the fifth-order derivative. The solver thus combines spectral differentiation in space, AB history quadrature in time, and a semi-implicit corrector. The numerical method is validated in two independent ways, by comparison with the LADM solution and by a grid-refinement test. The refined numerical field is subsequently used as the principal reference for PINN assessment.

3.4 Physics-Informed Neural Network Methodology

The PINN approximates the solution by a neural function $u_\theta(x,t)$, where θ denotes all trainable weights and biases. On the periodic spatial domain, the coordinate x is encoded through $\sin x$ and $\cos x$, so that periodicity is built into the network representation:

$$u_\theta(x,t) = \mathscr{N}_\theta(\sin x, \cos x, t). \tag{32}$$

To avoid repeatedly evaluating the ML derivative, the PINN enforces the equivalent AB integral equation. We define

$$\begin{aligned} F_\theta = S(x,t) - \big[&c(u_\theta)_x + a u_\theta (u_\theta)_x \\ &- b u_\theta^2 (u_\theta)_x + \mu (u_\theta)_{xxx} + \nu (u_\theta)_{xxxxx}\big]. \end{aligned} \tag{33}$$

The spatial derivatives are obtained by automatic differentiation. The physics residual is then

$$\begin{aligned} R_\theta = u_\theta - \phi(x) &- \frac{1-\alpha}{B(\alpha)} F_\theta \\ &- \frac{\alpha}{B(\alpha)\Gamma(\alpha)} \int_0^t (t-\tau)^{\alpha-1} F_\theta(x,\tau)\,\mathrm{d}\tau. \end{aligned} \tag{34}$$

The history integral is discretized on ordered time levels using the same class of product-integration weights as in Section 3.2. With a characteristic solution scale U_s, the normalized physics loss is

$$\mathscr{L}_f = \frac{1}{N_f} \sum_{i=1}^{N_f} \left| \frac{R_\theta(x_i,t_i)}{U_s} \right|^2. \tag{35}$$

When the initial condition is enforced softly, the total loss may include an additional initial-condition term. In the present implementation, the initial condition is imposed as a hard output constraint. Its contribution to the training loss is therefore identically zero, and the optimized objective is the fractional physics residual loss.

4 Analytical Application and Results

We now apply the analytical formulation to a compatibility-aware forced ABC fractional GK benchmark. The source term is selected to vanish at the initial time so that the zero initial state, the local part of the AB integral, and the spatial operator are mutually consistent.

4.1 Selected Compatible Test Problem

The benchmark equation is

$$\begin{aligned} {}^{\mathrm{ABC}}D_t^\alpha u + 2u_x + \frac{5}{7} u u_x - \frac{15}{7} u^2 u_x \\ + \frac{1}{3} u_{xxx} + \frac{1}{42} u_{xxxxx} = t \sin x. \end{aligned} \tag{36}$$

The computational domain is

$$-\pi \le x \le \pi, \qquad 0 \le t \le 0.10. \tag{37}$$

The initial condition is

$$u(x,0) = 0, \tag{38}$$

and periodic boundary conditions are imposed:

$$\begin{aligned} &u(-\pi,t) = u(\pi,t), \\ &\partial_x^m u(-\pi,t) = \partial_x^m u(\pi,t), \qquad m = 1,2,\ldots,5. \end{aligned} \tag{39}$$

The fixed parameters are

$$\begin{aligned} &c = 2, \qquad a = \frac{5}{7}, \qquad b = \frac{15}{7}, \\ &\mu = \frac{1}{3}, \qquad \nu = \frac{1}{42}. \end{aligned} \tag{40}$$

The fractional orders considered are

$$\alpha = 1.00, \quad 0.95, \quad 0.90, \quad 0.85. \tag{41}$$

At $t = 0$, the solution and all its spatial derivatives vanish, and the forcing $t \sin x$ is also zero. The initial state is therefore compatible with the governing equation and its AB integral representation.

4.2 LADM Application

Since the initial state is zero, the leading LADM component is generated entirely by the forcing:

$$u_0(x,t) = {}^{\mathrm{AB}}I_t^{\alpha}[t \sin x]. \tag{42}$$

Using Eq. (5), we obtain

$$u_0(x,t) = \sin x \left[\frac{1-\alpha}{B(\alpha)} t + \frac{\alpha}{B(\alpha)\Gamma(\alpha+2)} t^{\alpha+1} \right]. \tag{43}$$

For $\alpha = 1$, this reduces to

$$u_0(x,t) = \frac{t^2}{2} \sin x. \tag{44}$$

The higher components are generated as follows:

$$u_1 = -{}^{\mathrm{AB}}I_t^{\alpha}[G_0], \tag{45}$$

$$u_2 = -{}^{\mathrm{AB}}I_t^{\alpha}[G_1], \tag{46}$$

and, in general,

$$u_{n+1} = -{}^{\mathrm{AB}}I_t^{\alpha}[G_n]. \tag{47}$$

Six components, u_0 through u_5, are retained. The final analytical approximation is therefore

$$u_{\mathrm{LADM}}^{(5)}(x,t) = \sum_{n=0}^{5} u_n(x,t). \tag{48}$$

4.3 Analytical Evaluation and Validation

The relative magnitude of the final retained component is measured by

$$\eta_5 = \frac{\|u_5\|_2}{\|u_{\mathrm{LADM}}^{(5)}\|_2}. \tag{49}$$

Initial-condition consistency is checked at a small positive time ε through

$$E_{\mathrm{IC}} = \max_x \left| u_{\mathrm{LADM}}^{(5)}(x,\varepsilon) \right|. \tag{50}$$

The integral-equation residual is

$$R_I = u_{\mathrm{LADM}}^{(5)} - {}^{\mathrm{AB}}I_t^{\alpha} \left[t \sin x - \mathscr{G}\left(u_{\mathrm{LADM}}^{(5)} \right) \right], \tag{51}$$

with normalized measure

$$E_R = \frac{\|R_I\|_2}{\|u_{\mathrm{LADM}}^{(5)}\|_2}. \tag{52}$$

Table 1 Validation of the six-component LADM approximation at $t = 0.10$.

α	η_5	Relative residual	Maximum IC error
1.00	$5.48562432 \times 10^{-8}$	$1.15874427 \times 10^{-9}$	$5.00000000 \times 10^{-17}$
0.95	$8.34878532 \times 10^{-5}$	$1.15016034 \times 10^{-5}$	$5.12977160 \times 10^{-10}$
0.90	$1.32648851 \times 10^{-3}$	$3.30414648 \times 10^{-4}$	$1.04469768 \times 10^{-9}$
0.85	$8.47731817 \times 10^{-3}$	$3.10022266 \times 10^{-3}$	$1.58203849 \times 10^{-9}$

At $t = 0.10$, the last retained component contributes less than 1% of the accumulated solution magnitude even for $\alpha = 0.85$. The normalized residual is approximately 0.31% in that case, and the initial-condition diagnostic remains below 1.6×10^{-9} for all the fractional cases.

Figure 1 shows a systematic increase in the forced response as the fractional order decreases from 1.00 to 0.85. With the forcing and coefficients held fixed, the larger amplitude reflects the change in the transient response under the ABC memory law. The profiles also exhibit a modest spatial shift and a change in shape, indicating that memory interacts with both nonlinearity and higher-order dispersion.

Figure 2 shows the evolution of the $\alpha = 0.90$ solution from the zero initial state. The wave amplitude grows under

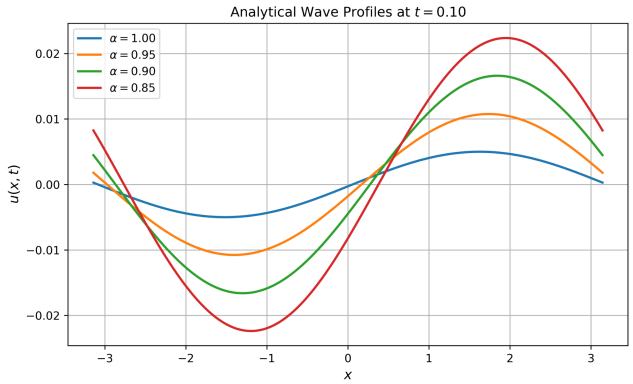


Fig. 1 Analytical LADM wave profiles for different fractional orders at $t = 0.10$.

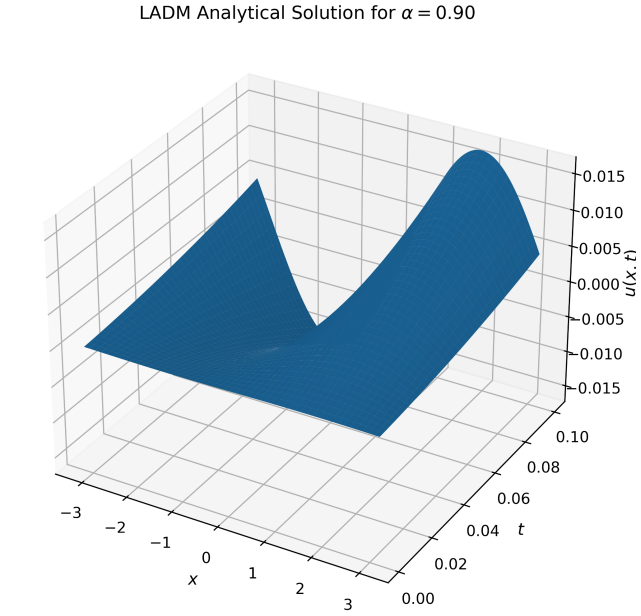


Fig. 2 Three-dimensional LADM solution for $\alpha = 0.90$ over the space–time domain.

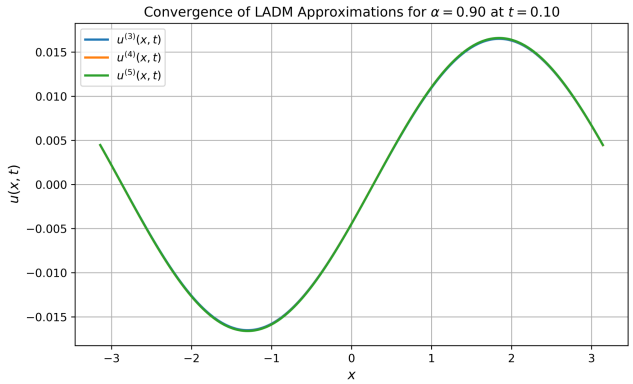


Fig. 3 Successive LADM approximations for $\alpha = 0.90$ at $t = 0.10$.

the forcing while the periodic spatial structure is preserved. The plotted surface is smooth through the initial transient. Figure 3 provides a visual comparison of the third-, fourth-, and fifth-order truncations. The curves are nearly indistinguishable at $t = 0.10$, consistent with the diagnostics in Table 1 and supporting the use of the six-component truncation in subsequent comparisons.

5 Numerical Application and Results

The numerical scheme of Section 3.2 is applied to the same benchmark, so that differences between the numerical and analytical approximations can be attributed to the solution methods under comparison.

5.1 Computational Setup

The numerical equation, domain, initial condition, and parameters are given in Eqs. (36)–(41). The spatial and temporal resolutions of the refined computation are

$$N_x = 128, \qquad N_t = 800, \tag{53}$$

and the coarser computation uses

$$N_x = 64, \qquad N_t = 400. \tag{54}$$

The pointwise difference between the numerical and LADM solutions is

$$E(x,t) = \left| u_{\mathrm{Num}}(x,t) - u_{\mathrm{LADM}}(x,t) \right|, \tag{55}$$

with relative L_2 error

$$E_{L_2} = \frac{\| u_{\mathrm{Num}} - u_{\mathrm{LADM}} \|_2}{\| u_{\mathrm{LADM}} \|_2}, \tag{56}$$

and maximum error

$$E_{\max} = \max_x \left| u_{\mathrm{Num}} - u_{\mathrm{LADM}} \right|. \tag{57}$$

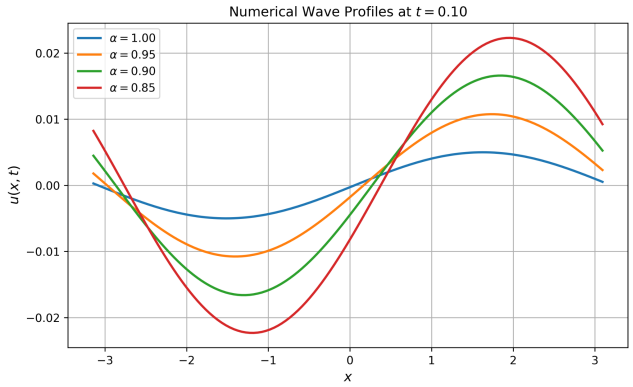


Fig. 4 Numerical wave profiles for different fractional orders at $t = 0.10$.

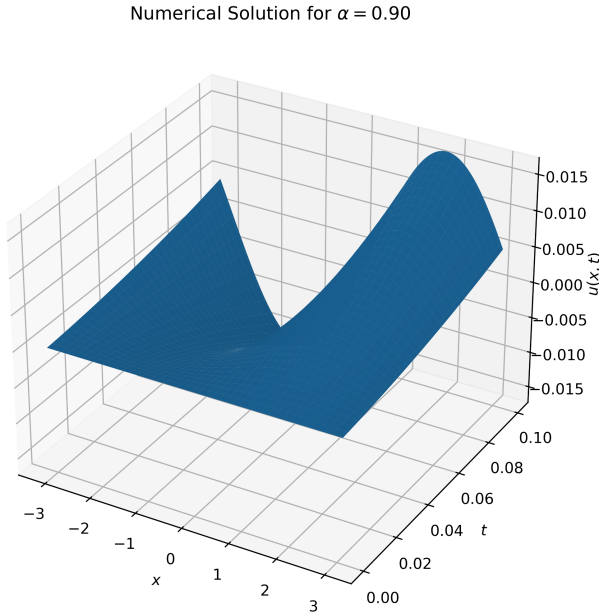


Fig. 5 Three-dimensional numerical solution for $\alpha = 0.90$ over the space–time domain.

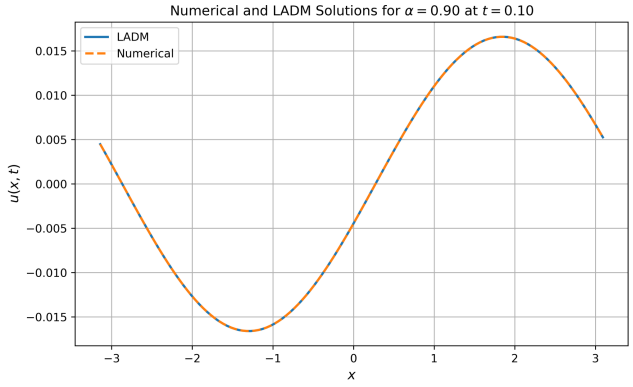


Fig. 6 Comparison between the numerical and six-component LADM solutions for $\alpha = 0.90$ at $t = 0.10$.

5.2 Numerical Results and Validation

Figure 4 reproduces the trend observed in the LADM solutions. Lower values of α lead to a stronger response under the same forcing. The three-dimensional numerical field in Figure 5 closely matches the analytical evolution in Figure 2. The solution starts from zero, remains smooth and periodic, and grows continuously over the selected time interval. For $\alpha = 0.90$, the numerical and analytical profiles in Figure 6 are visually indistinguishable over nearly the entire domain.

Table 2 Numerical-versus-LADM errors at $t = 0.10$.

α	Relative L_2 error	Maximum error
1.00	$4.42450475 \times 10^{-8}$	$2.21130576 \times 10^{-10}$
0.95	$1.14100547 \times 10^{-5}$	$1.27636378 \times 10^{-7}$
0.90	$3.21049038 \times 10^{-4}$	$5.65700071 \times 10^{-6}$
0.85	$2.91561950 \times 10^{-3}$	$7.04892195 \times 10^{-5}$

The numerical and LADM solutions agree closely for all four orders. At $\alpha = 0.90$, the relative L_2 difference is approximately 3.21×10^{-4}, or 0.0321%. Even at $\alpha = 0.85$, the relative error remains below 0.3%. The absolute-error

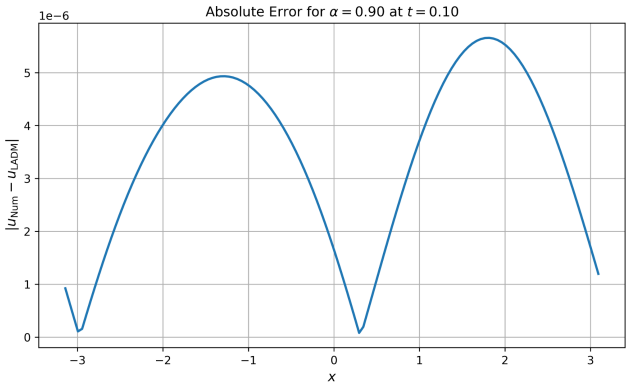


Fig. 7 Absolute difference between the numerical and LADM solutions for $\alpha = 0.90$ at $t = 0.10$.

profile in Figure 7 remains of order 10^{-6}. The error is largest in regions of high curvature and large amplitude, while its magnitude is several orders below that of the solution itself.

Table 3 Grid-refinement comparison between the 64×400 and 128×800 solutions.

α	Relative difference	Maximum difference
1.00	$1.32170402 \times 10^{-7}$	$6.60212680 \times 10^{-10}$
0.95	$7.46495903 \times 10^{-8}$	$8.03592498 \times 10^{-10}$
0.90	$5.63526560 \times 10^{-8}$	$9.37358500 \times 10^{-10}$
0.85	$4.64938066 \times 10^{-8}$	$1.04185851 \times 10^{-9}$

The relative grid-refinement differences in Table 3 range from order 10^{-8} to order 10^{-7}. For the lower fractional orders, these differences are several orders of magnitude smaller than the differences between the numerical and LADM solutions. This suggests that finite LADM truncation accounts for most of the discrepancy at those orders.

6 Physics-Informed Neural Network Application and Results

The PINN is applied to the representative fractional case $\alpha = 0.90$. The analytical and numerical results establish the fractional-order trend across four values of α. The PINN experiment tests whether a compact neural approximation can recover the fractional wave field from the governing physics. The predicted field is then compared with the refined numerical solution.

6.1 PINN Setup and Training Configuration

For $\alpha = 0.90$, the governing equation is

$$
\begin{aligned}
{}^{\mathrm{ABC}}D_t^{0.90}u + 2u_x + \frac{4}{7}uu_x - \frac{15}{7}u^2u_x \\
+ \frac{1}{3}u_{xxx} + \frac{1}{42}u_{xxxxx} = t\sin x.
\end{aligned}
\tag{58}
$$

The domain and initial condition are

$$
-\pi \le x \le \pi, \qquad 0 \le t \le 0.10, \qquad u(x,0) = 0. \tag{59}
$$

The network architecture is

$$
3 \longrightarrow 40 \longrightarrow 40 \longrightarrow 40 \longrightarrow 1, \tag{60}
$$

where the three inputs are $(\sin x, \cos x, t)$ and the output is the predicted wave amplitude. The hidden layers use hyperbolic tangent activation. The initial condition is imposed exactly through the transformed output

$$
\begin{aligned}
u_\theta(x,t) &= A_s \frac{t}{T}\widehat{u}_\theta(x,t), \\
A_s &= 0.03, \qquad T = 0.10.
\end{aligned}
\tag{61}
$$

Thus $u_\theta(x,0) = 0$ for all network parameters.

Table 4 PINN training configuration.

Quantity	Value
Fractional order	$\alpha = 0.90$
Spatial training points	$N_x = 20$
Temporal training points	$N_t = 21$
Hidden layers	3
Neurons per hidden layer	40
Activation	tanh
Optimizer	Adam
Learning rate	10^{-3}
Epochs	500
Floating-point precision	64-bit
Characteristic output scale	$A_s = 0.03$
Residual normalization scale	$U_s = 0.02$
Initial condition	Hard enforced
Spatial periodicity	$\sin x, \cos x$ encoding

With the adopted normalization, $B(0.90) = 0.9422008488$ and

$$
\frac{1-\alpha}{B(\alpha)} = 0.1061344830. \tag{62}
$$

The PINN right-hand side is

$$
\begin{aligned}
F_\theta = t\sin x - \Big[2(u_\theta)_x + \frac{4}{7}u_\theta(u_\theta)_x - \frac{15}{7}u_\theta^2(u_\theta)_x \\
+ \frac{1}{3}(u_\theta)_{xxx} + \frac{1}{42}(u_\theta)_{xxxxx} \Big].
\end{aligned}
\tag{63}
$$

The integral-form residual is

$$
\begin{aligned}
R_\theta = u_\theta - \frac{1-\alpha}{B(\alpha)}F_\theta \\
- \frac{\alpha}{B(\alpha)\Gamma(\alpha)} \int_0^t (t-\tau)^{\alpha-1} F_\theta(x,\tau)\,\mathrm{d}\tau,
\end{aligned}
\tag{64}
$$

and the optimized loss is the normalized mean-square residual

$$
\mathscr{L} = \frac{1}{N_f}\sum_{i=1}^{N_f} \left| \frac{R_\theta(x_i,t_i)}{0.02} \right|^2. \tag{65}
$$

Because the initial condition is imposed exactly, the initial-condition loss remains zero throughout training.

6.2 Training Convergence

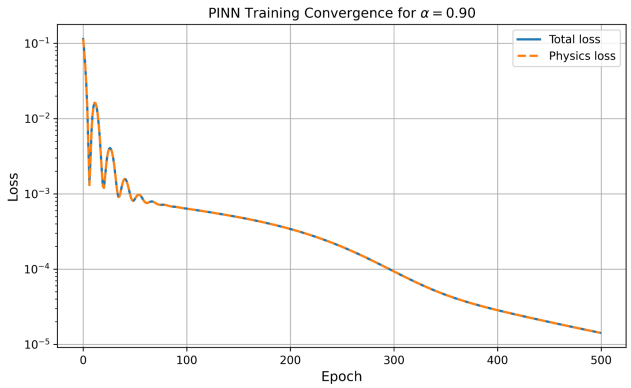


Fig. 8 PINN training-loss convergence for $\alpha = 0.90$.

The Adam training loss decreases from 1.140067×10^{-1} at the first epoch to approximately 1.426858×10^{-5} after 500 epochs. A final reevaluation gives

$$\mathscr{L}_{\text{final}} = 1.41754693 \times 10^{-5}, \qquad \mathscr{L}_{\text{IC}} = 0. \tag{66}$$

Figure 8 shows a steep initial reduction in the training loss followed by a slower, smooth decay. The loss shows no late-stage divergence despite the fifth-order spatial differentiation and the nonlocal time-history term.

6.3 PINN Validation Against the Numerical Solution

The trained PINN is evaluated on the 801×128 numerical reference grid generated in Section 5. The full space–time relative error is

$$E_{L_2}^{\text{ST}} = \frac{\|u_{\text{PINN}} - u_{\text{Num}}\|_2}{\|u_{\text{Num}}\|_2} = 1.07337185 \times 10^{-2}, \tag{67}$$

and the maximum space–time error is

$$E_{\max}^{\text{ST}} = 3.71971182 \times 10^{-4}. \tag{68}$$

At $t = 0.10$,

$$E_{L_2}^{t=0.10} = 1.25957586 \times 10^{-2}, \tag{69}$$

with

$$E_{\max}^{t=0.10} = 3.71971182 \times 10^{-4}. \tag{70}$$

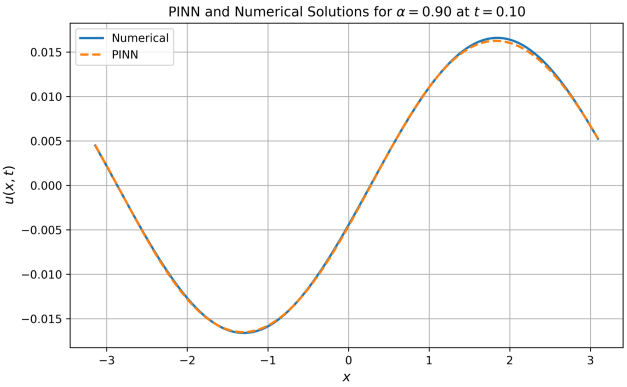


Fig. 9 Comparison between the PINN and numerical solutions for $\alpha = 0.90$ at $t = 0.10$.

The relative error is approximately 1.07% over the full space–time domain and 1.26% at the final time.

Figure 9 shows that the PINN captures both the negative trough and the positive crest of the numerical solution. The profiles remain close across the periodic interval, with the most visible discrepancy near the largest positive crest.

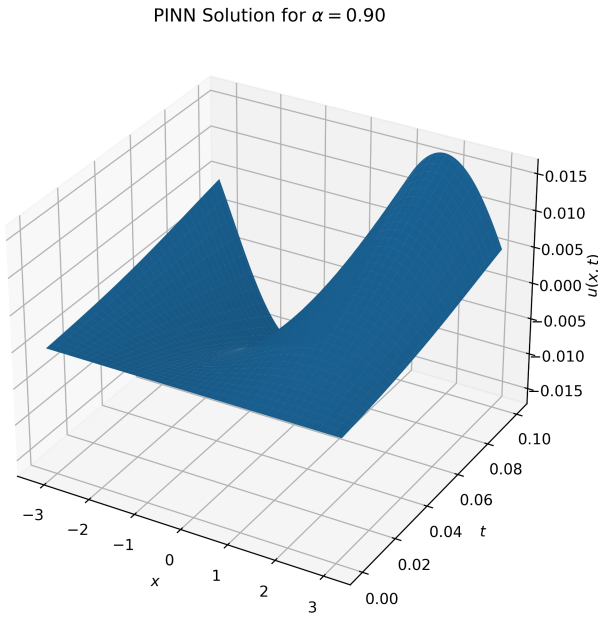


Fig. 10 Three-dimensional PINN solution for $\alpha = 0.90$ over the space–time domain.

The PINN surface in Figure 10 reproduces the overall space–time structure of the analytical and numerical solutions. The hard initial constraint makes the solution exactly

zero at $t = 0$, and the solution then grows smoothly under the forcing.

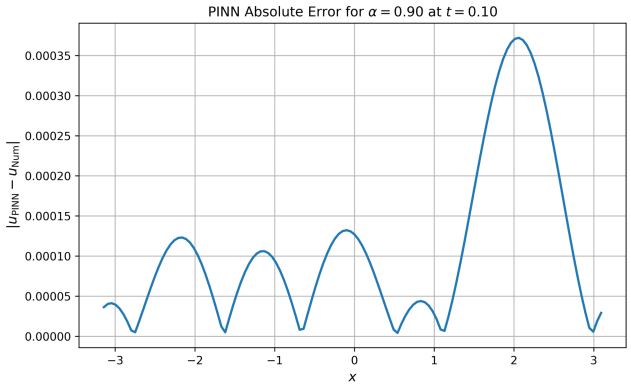


Fig. 11 Absolute PINN error relative to the numerical solution for $\alpha = 0.90$ at $t = 0.10$.

The final-time error profile in Figure 11 remains below 4×10^{-4}. The largest discrepancy occurs near the dominant positive crest, where the amplitude and spatial curvature are strongest.

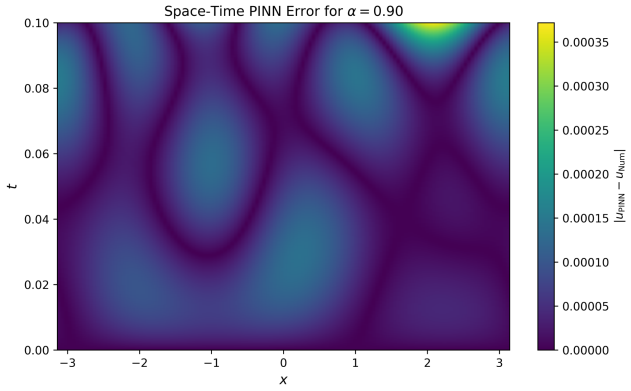


Fig. 12 Space–time absolute-error distribution between the PINN and numerical solutions for $\alpha = 0.90$.

The heat map in Figure 12 shows that the PINN error is smallest near the initial time and becomes more pronounced toward $t = 0.10$, especially around the growing crest. This pattern is consistent with the increasing difficulty of approximating the forced nonlinear wave as its amplitude grows. The error remains small compared with the solution scale across the domain.

7 Comparative Assessment of LADM, Numerical, and PINN Solutions

The three methods serve different mathematical roles. LADM provides an explicit truncated series that shows how forcing, nonlinearity, dispersion, and fractional memory enter successive corrections. The Fourier pseudospectral solver provides a numerical reference by resolving the periodic spatial derivatives spectrally. The grid-refinement test quantifies the sensitivity of that reference to the spatial and temporal resolutions tested. The PINN provides a global approximation constrained by the governing integral equation. For $\alpha = 0.90$, the relative difference between the numerical and LADM solutions at $t = 0.10$ is 3.21049×10^{-4}, whereas the relative difference between the coarse and refined numerical grids is 5.63527×10^{-8}. The difference between the two numerical grids is thus several orders of magnitude smaller than the numerical–LADM difference. The PINN has a full-domain relative error of 1.07337×10^{-2} and a final-time relative error of 1.25958×10^{-2} against the numerical reference. It reproduces the principal wave shape with a relative error of approximately 1% over the space–time domain.

The following comparisons bring together the fractional-order response, the full space–time surfaces, and the pairwise profiles and errors reported in Sections 4–6.

7.1 Fractional-Order Response Consistency

Figure 13 shows that the LADM and Fourier pseudospectral solutions predict the same dependence on the fractional order. At each tested value of α, the two profiles agree closely in phase and overall shape. In both computations, the amplitude increases as α decreases. The agreement between the two methods supports the interpretation that the stronger response arises from the ABC memory law.

7.2 Three-Way Space–Time Surface Comparison

The three surfaces in Figure 14 start from the zero initial state and show a periodic wave that grows under the forcing. The LADM and numerical surfaces are visually almost

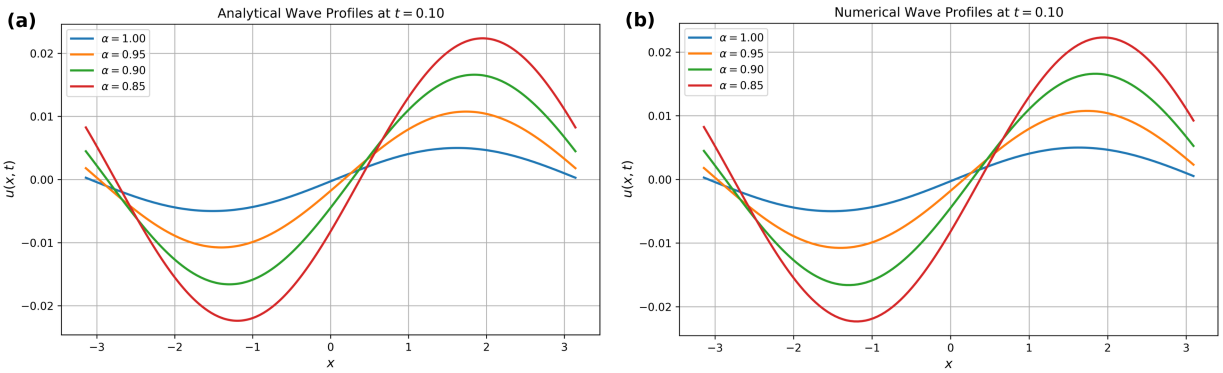


Fig. 13 Side-by-side LADM and numerical wave profiles for $\alpha = 1.00, 0.95, 0.90$, and 0.85 at $t = 0.10$.

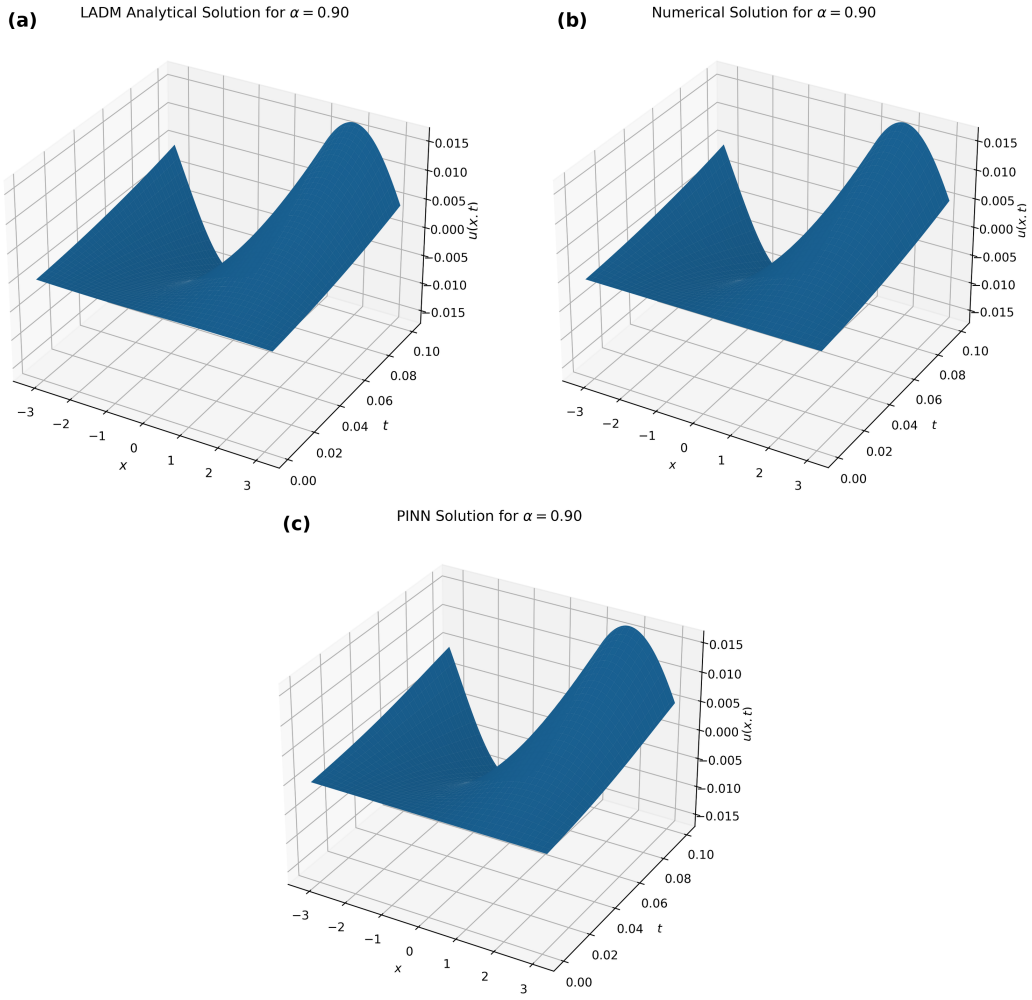


Fig. 14 Three-dimensional comparison for $\alpha = 0.90$. (a) LADM approximation, (b) Fourier pseudospectral solution, and (c) PINN reconstruction.

Table 5 Three-way comparison for the representative case $\alpha = 0.90$.

Method	Main representation	Key validation measure	Observed value	Principal strength	Main limitation
Six-component LADM	Semi-analytical series	Relative difference from the numerical solution at $t = 0.10$	3.21049×10^{-4}	Explicit analytical structure and close agreement between successive short-time truncations	Accuracy depends on the truncation and the time interval
Fourier pseudospectral with ABC history	Grid-based deterministic solution	Relative difference between the 64×400 and 128×800 grids	5.63527×10^{-8}	Small sensitivity to grid refinement in the present study	Requires grid-based time integration and storage and updating of the nonlocal history
PINN	Global neural approximation	Full space–time relative L_2 error against the numerical reference	1.07337×10^{-2}	Continuous approximation with the governing physics embedded in the loss	Training is slower and agreement with the numerical reference is weaker for this benchmark

indistinguishable, consistent with their small relative difference. The PINN reproduces the overall wave shape and the locations of the dominant crest and trough, with small amplitude deviations at later times. Table 5 quantifies the differences between the computed fields.

7.3 Pairwise Profile and Error Comparison

In Figure 15(a,c), the LADM and numerical curves overlap almost perfectly, with pointwise differences of order 10^{-6}. Panels (b) and (d) show that the PINN also reconstructs the wave profile, with a larger discrepancy that reaches approximately 3.72×10^{-4} near the dominant crest. The final-time relative L_2 differences are 3.21×10^{-4} for numerical versus LADM and 1.26×10^{-2} for PINN versus numerical. The spectral solution provides the numerical reference, the six-component LADM gives an accurate short-time analytical approximation, and the PINN provides a global surrogate constrained by the integral equation.

LADM is useful when a compact analytical series and interpretation of the parameters are important. The Fourier pseudospectral solver provides an accurate reference on the periodic domain. The PINN offers a reusable differentiable surrogate for extensions involving incomplete data or inverse problems. In this forward benchmark, the deterministic and analytical approximations agree closely, and the neural approximation is assessed against the refined numerical reference in addition to its training residual.

8 Comparison with Related Published Studies

We compare the present results with representative studies of fractional Kawahara-type models, classical GK computation, and PINN methods for high-order Kawahara equations. The governing equations, domains, initial data, fractional operators, and test cases vary across studies, so the comparison focuses on model scope, memory operator, methodology, and validation strategy.

The closest study involving fractional memory is that of Bhatter et al. [17], who used the ABC operator for a modified Kawahara equation and obtained analytical approximations through the homotopy analysis transform method (HATM). Their work illustrates the use of Mittag–Leffler memory in fifth-order nonlinear dispersive waves. The GK equation studied here retains both uu_x and u^2u_x. Its analytical approximation is compared with an independent pseudospectral history solver and used in a three-way assessment.

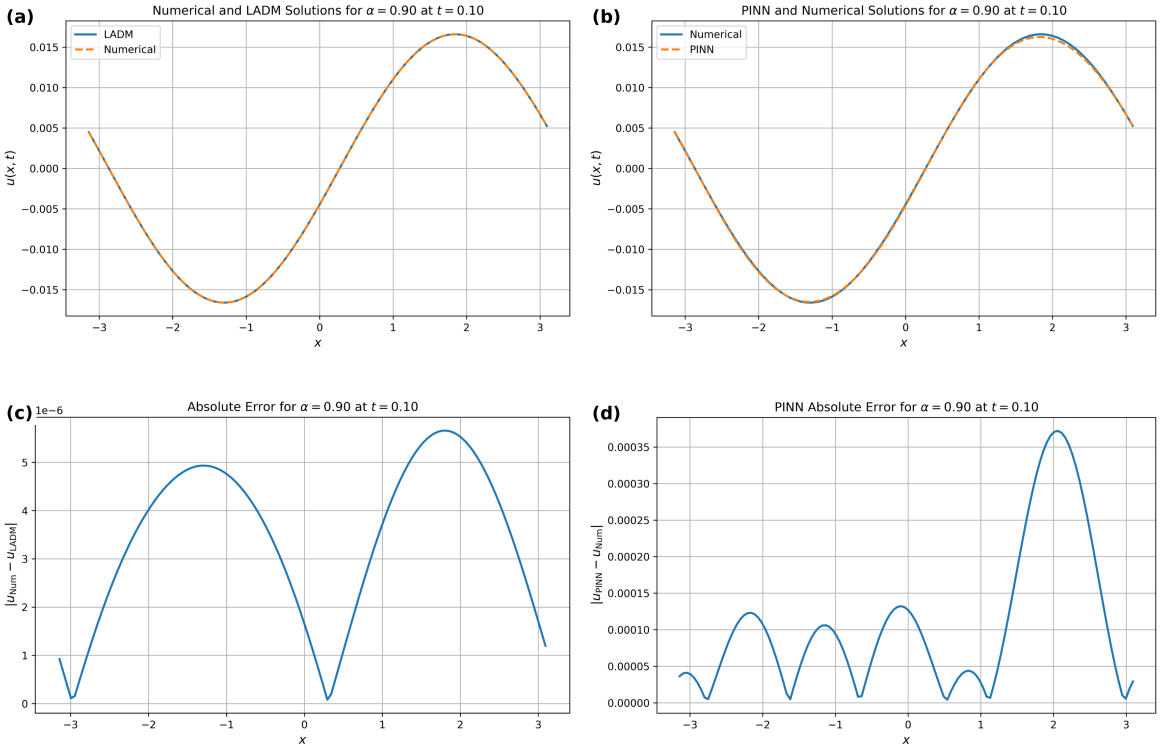


Fig. 15 Pairwise validation for $\alpha = 0.90$ at $t = 0.10$. (a) LADM versus numerical solution, (b) PINN versus numerical solution, (c) $|u_{\text{Num}} - u_{\text{LADM}}|$, and (d) $|u_{\text{PINN}} - u_{\text{Num}}|$.

Table 6 Position of the present study relative to representative literature.

Study	**Model/operator**	**Main method**	**Key distinction relative to the present work**
Bhatter et al. [17]	ABC fractional modified Kawahara equation	Homotopy analysis transform	Uses Mittag–Leffler memory for a modified Kawahara equation. The present study combines quadratic and cubic GK nonlinearities with a three-way comparison.
Ullah et al. [19]	Caputo fractional Kawahara and modified Kawahara equations	Integral transforms and decomposition	Uses the singular power-law Caputo kernel.
Ucar et al. [20]	Classical Gardner–Kawahara equation	Trigonometric quintic B-spline collocation	Treats integer-order GK dynamics.
Ali et al. [21]	Classical Gardner–Kawahara equation	Exact expansions and septic B-spline collocation	Compares exact and numerical results for the classical model.
Towhiduzzaman et al. [26]	$(3+1)$-dimensional Fornberg–Whitham equation	Hirota bilinear method and PINN	Compares analytical and PINN solutions using coordinated multi-panel visualizations.
Kabiri and Sabooni [27]	Classical Gardner–Kawahara inverse problem	PINN	Recovers unknown coefficients from sparse data.
Anand et al. [28]	Modified Kawahara equations	PINN with curriculum learning	Treats forward problems for modified Kawahara equations.

The classical GK studies by Ucar et al. [20] and Ali et al. [21] demonstrate the effectiveness of high-order B-spline collocation for integer-order GK dynamics. On the periodic domain considered here, the Fourier method evaluates spatial derivatives globally in spectral space. The relative grid-refinement differences in Table 3 are of order 10^{-8} to 10^{-7}, indicating low sensitivity to refinement for this test problem.

Towhiduzzaman et al. [26] combined Hirota-based analytical solutions with PINN reconstruction for a $(3+1)$-dimensional Fornberg–Whitham equation and used surface, contour, profile, and error plots to assess the learned wave structures. Kabiri and Sabooni [27] used a PINN to identify unknown coefficients from sparse data in inverse Gardner–Kawahara problems. Anand et al. [28] applied PINNs with curriculum learning to modified Kawahara equations. These studies show that neural networks can handle high-order dispersive operators. The present study incorporates nonlocal ABC temporal memory and adds an independent grid-converged Fourier benchmark. The PINN is thus evaluated against a numerical reference that can also be compared with the analytical approximation.

ABC fractional derivatives, decomposition methods, Fourier methods, GK solvers, and PINNs are all established in prior work. The central contribution of the present study is to bring these methods together in a compatibility-aware ABC Gardner–Kawahara benchmark and to compare the resulting analytical, numerical, and neural approximations.

9 Conclusion

We investigated a forced ABC fractional Gardner–Kawahara equation using Laplace–Adomian decomposition, a Fourier pseudospectral solver with ABC time integration, and a physics-informed neural network. The benchmark uses a zero initial state and a forcing term $t\sin x$ that vanishes at $t=0$. This choice satisfies the initial-time compatibility condition of the AB integral equation and avoids the start-up mismatch that can arise when the prescribed initial profile and the right-hand side are incompatible.

For the selected parameters on $0 \le t \le 0.10$, the six-component LADM approximation has a small last retained component and a small normalized integral residual. Even at $\alpha = 0.85$, the last component accounts for less than 1% of the accumulated solution magnitude, and the normalized residual is approximately 0.31%. As α decreases from 1.00 to 0.85, the forced transient grows in amplitude and changes modestly in shape. The Fourier pseudospectral results reproduce these trends. At $t = 0.10$, the relative numerical–LADM difference ranges from 4.42×10^{-8} at $\alpha = 1$ to 2.92×10^{-3} at $\alpha = 0.85$. The relative grid-refinement differences are of order 10^{-8} to 10^{-7}. For $\alpha = 0.90$, the relative numerical–LADM difference is 3.21×10^{-4}.

The PINN experiment provides a third comparison. A compact $3-40-40-40-1$ network uses periodic spatial features, hard enforcement of the zero initial condition, fifth-order automatic differentiation, and a residual based on the AB integral equation. Its final normalized training loss is approximately 1.42×10^{-5}. Against the refined numerical reference, the PINN yields a relative L_2 error of approximately 1.07% over the full space–time domain and 1.26% at the final time. It reconstructs the main wave features without using the numerical solution as training data.

For this benchmark, changing the ABC fractional order substantially alters the amplitude of the forced transient. The semi-analytical series shows how successive corrections enter the approximation, the spectral solver supplies a reference checked by grid refinement, and the PINN provides a continuous approximation constrained by the nonlocal integral equation.

Future work could extend the benchmark to longer times, nonzero initial states that satisfy the compatibility condition, alternative forcing functions, and physically calibrated parameter sets. Fast-history or sum-of-exponentials approximations could reduce the cost of evaluating the ABC memory term. Adaptive sampling, curriculum time marching, Fourier features, operator learning, and higher-order optimization could improve PINN accuracy or reduce training cost. The same framework could also be used to identify the fractional order and Gardner–Kawahara coefficients from sparse measurements.

References

1. I. Podlubny, *Fractional Differential Equations*, Academic Press, San Diego, 1999.
2. A. A. Kilbas, H. M. Srivastava, and J. J. Trujillo, *Theory and Applications of Fractional Differential Equations*, Elsevier, Amsterdam, 2006.
3. K. Diethelm, *The Analysis of Fractional Differential Equations*, Springer, Berlin, 2010. doi: 10.1007/978-3-642-14574-2.
4. M. Caputo, Linear models of dissipation whose Q is almost frequency independent—II, *Geophysical Journal of the Royal Astronomical Society* **13**(5), 529–539 (1967). doi: 10.1111/j.1365-246X.1967.tb02303.x.
5. A. Atangana and D. Baleanu, New fractional derivatives with nonlocal and non-singular kernel: Theory and application to heat transfer model, *Thermal Science* **20**(2), 763–769 (2016). doi: 10.2298/TSCI160111018A.
6. T. Abdeljawad and D. Baleanu, Integration by parts and its applications of a new nonlocal fractional derivative with Mittag–Leffler nonsingular kernel, *Journal of Nonlinear Sciences and Applications* **10**(3), 1098–1107 (2017). doi: 10.22436/jnsa.010.03.20.
7. S. Yadav, R. K. Pandey, and A. K. Shukla, Numerical approximations of Atangana–Baleanu Caputo derivative and its application, *Chaos, Solitons & Fractals* **118**, 58–64 (2019). doi: 10.1016/j.chaos.2018.11.009.
8. A. Atangana and K. M. Owolabi, New numerical approach for fractional differential equations, *Mathematical Modelling of Natural Phenomena* **13**(1), 3 (2018). doi: 10.1051/mmnp/2018010.
9. S. Aljhani, M. S. M. Noorani, R. Douaifia, and S. Abdelmalek, A high-order predictor–corrector method for initial value problems with fractional derivative involving Mittag–Leffler kernel, *Mathematical Methods in the Applied Sciences* **48**(7), 7378–7397 (2025). doi: 10.1002/mma.9040.
10. K. Diethelm, N. J. Ford, and A. D. Freed, A predictor–corrector approach for the numerical solution of fractional differential equations, *Nonlinear Dynamics* **29**, 3–22 (2002). doi: 10.1023/A:1016592219341.
11. T. Kawahara, Oscillatory solitary waves in dispersive media, *Journal of the Physical Society of Japan* **33**(1), 260–264 (1972). doi: 10.1143/JPSJ.33.260.
12. O. Kurkina, N. Singh, and Y. Stepanyants, Structure of internal solitary waves in two-layer fluid at near-critical situation, *Communications in Nonlinear Science and Numerical Simulation* **22**, 1235–1242 (2015). doi: 10.1016/j.cnsns.2014.09.018.
13. N. Polat, D. Kaya, and H. I. Tutalar, A analytic and numerical solution to a modified Kawahara equation and a convergence analysis of the method, *Applied Mathematics and Computation* **181**(1), 193–199 (2006). doi: 10.1016/j.amc.2005.11.104.
14. D. Kaya and K. Al-Khaled, A numerical comparison of a Kawahara equation, *Physics Letters A* **363**(5–6), 433–439 (2007). doi: 10.1016/j.physleta.2006.11.055.
15. M. Benbachir and A. Saadi, The Kawahara equation with time and space-fractional derivatives solved by the Adomian method, *Journal of Interdisciplinary Mathematics* **17**(3), 243–253 (2014). doi: 10.1080/09720502.2013.801657.
16. A. Atangana, N. Bildik, and S. C. O. Noutchie, New iteration methods for time-fractional modified nonlinear Kawahara equation, *Abstract and Applied Analysis* **2014**, 740248 (2014). doi: 10.1155/2014/740248.
17. S. Bhatter, A. Mathur, D. Kumar, K. S. Nisar, and J. Singh, Fractional modified Kawahara equation with Mittag–Leffler law, *Chaos, Solitons & Fractals* **131**, 109508 (2020). doi: 10.1016/j.chaos.2019.109508.
18. A. Daşcıoğlu and S. Çulha Ünal, New exact solutions for the space-time fractional Kawahara equation, *Applied Mathematical Modelling* **89**, 952–965 (2021). doi: 10.1016/j.apm.2020.07.053.
19. I. Ullah, A. Ali, and S. Saifullah, Analysis of time-fractional non-linear Kawahara equations with power law kernel, *Chaos, Solitons & Fractals: X* **9**, 100084 (2022). doi: 10.1016/j.csfx.2022.100084.
20. Y. Ucar, N. M. Yagmurlu, A. Esen, and B. Karaagac, A new numerical approach to Gardner Kawahara equation in magneto-acoustic waves in plasma physics, *International Journal for Numerical Methods in Fluids* **95**(6),

979–991 (2023). doi: 10.1002/fld.5181.

21. K. K. Ali, D. Yıldırım Sucu, and S. B. G. Karakoc, Two effective methods for solution of the Gardner–Kawahara equation arising in wave propagation, *Mathematics and Computers in Simulation* **220**, 192–203 (2024). doi: 10.1016/j.matcom.2024.01.005.
22. Y. Gong, J. Cai, and Y. Wang, Multi-symplectic Fourier pseudospectral method for the Kawahara equation, *Communications in Computational Physics* **16**(1), 35–55 (2014). doi: 10.4208/cicp.090313.041113a.
23. M. Raissi, P. Perdikaris, and G. E. Karniadakis, Physics-informed neural networks: A deep learning framework for solving forward and inverse problems involving nonlinear partial differential equations, *Journal of Computational Physics* **378**, 686–707 (2019). doi: 10.1016/j.jcp.2018.10.045.
24. G. Pang, L. Lu, and G. E. Karniadakis, fPINNs: Fractional physics-informed neural networks, *SIAM Journal on Scientific Computing* **41**(4), A2603–A2626 (2019). doi: 10.1137/18M1229845.
25. G. E. Karniadakis, I. G. Kevrekidis, L. Lu, P. Perdikaris, S. Wang, and L. Yang, Physics-informed machine learning, *Nature Reviews Physics* **3**, 422–440 (2021). doi: 10.1038/s42254-021-00314-5.
26. M. Towhiduzzaman, M. A. Al Mohit, and A. Z. M. Asaduzzaman, Modeling lump and soliton wave interactions in the $(3+1)$D Fornberg–Whitham equation using a physics-informed neural network framework, *Partial Differential Equations in Applied Mathematics* **17**, 101330 (2026). doi: 10.1016/j.padiff.2025.101330.
27. M. Kabiri and S. Sabooni, Solving inverse Gardner–Kawahara problems with physics-informed neural networks: A data-driven approach, *Physica Scripta* **100**(10), 105204 (2025). doi: 10.1088/1402-4896/ae0769.
28. S. Anand, S. Natesan, and Ş. Toprakseven, Physics informed neural network framework for modified Kawahara equations, *Advances in Computational Science and Engineering* **8**, 50–73 (2026). doi: 10.3934/acse.2026007.